FACULTY OF SCIENCE AND TECHNOLOGY

MASTER'S THESIS

Study programme / specialisation: Engineering Structures and Materials / Mechanical Systems	The *(spring/~~autumn~~)* semester, *(2023)* Open / ~~Confidential~~
Author: Silje Helen Heggholmen	
Supervisor at UiS: Vidar Folke Hansen Co-supervisor: External supervisor(s):	
Thesis title: Microstructure and mechanical tests of a weld on a TIG welded UNS S31803 duplex stainless steel pipe	
Credits (ECTS): 30	
Keywords: UNS S31803 TIG welding Duplex Stainless Steel Mechanical testing Microstructure	Pages: 61 + appendix: 20 Stavanger, *(05.07.23)*

Abstract

University of Stavanger was given a pipe consisting of two parts of the duplex stainless steel grade UNS S31803, which had been welded together using TIG welding. The thesis is about examining the weld that goes around the pipe.

During the thesis both mechanical and microstructural tests were done. The specimens were machined at the university, the tensile test specimen by the workshop employees and the rest by the student. The mechanical tests were Charpy impact tests, tensile tests, and hardness tests, while the microstructure was studied using optical microscope, EBSD and EDS.

The mechanical tests gave good results, where the values were similar to what one would expect of the base material.

The microstructural findings showed some chromium nitrides and at least one carbide particle. There was 40 to 50% austenite in the entirety of the weld when looking over a large enough area. Near the root of the weld the microstructure was isotropic. Closer to the cap the ferrite grains were elongated in the same direction and bands of austenite rich areas crossed them.

Table of Contents

List of figures

List of abbreviations:

DSS – Duplex Stainless Steel

HAZ – Heat Affected Zone

HTHAZ – High Temperature Heat Affected Zone

LTHAZ – Low Temperature Heat Affected Zone

SEM – Scanning Electrode Microscope

EBSD – Electron Backscatter Diffraction

IPF – Inverse pole figure

EDS – Energy Dispersive X-ray spectroscopy

TIG – Tungsten Inert Gas welding

Acknowledgements

This thesis would not have been possible without the kind donation of the pipe with the weld which the thesis is focused on. Special thanks to Inge Omundsen from Subsea7 and Constantinos Tesfay from Rosenberg.

I want to thank Vidar Folke Hansen for being my supervisor and guiding me through the process. I also want to thank Navid Sayyar, a PhD student that works with super duplex, for guidance.

I want to thank Johan Andreas Håland Thorkaas and Mats Ingedal who taught me how to operate the lab equipment in a safe way and guided me in the methodology. Johan also operated the tensile test machine when the tests were done. I also want to express my gratitude to Espen Undheim who operated the SEM and helped generate the EBSD and EDS results.

I want to thank the mechanics at the university workshop and Kjell Høgemark — the CNC operator — for machining the tensile test specimen. I also want to thank the mechanics for guiding me when machining the Charpy impact test specimens and Kjell for making the notch in the specimens.

I also want to express my gratitude to family and friends for emotional support during the master thesis.

1 Introduction

The object of the thesis is a pipe given by Subsea7. It consists of two pieces of the duplex stainless steel grade UNS S31803 that were welded together by Rosenberg. The weld is welded with tungsten inert gas welding. The weld is done with multiple passes, which is similar to some methods of additive manufacturing due to repeatedly welding on small pieces of metal, thus some references in the theory section is from additive manufacturing.

UNS S31803 is a common grade of duplex stainless steel. It is used in several industries, including the oil and gas industry, chemical storage, and paper production. It is known to have good qualities from both its the austenite and the ferrite portions. The low carbon content makes it a weldable stainless steel. Yet, duplex stainless steels are known to form precipitates under poor heat treatment that can weaken the mechanical and corrosive resistant properties.

The purpose of this master thesis is to examine the weld in the pipe and find its properties with mechanical testing and examination of the microstructure. For the mechanical tests Charpy impact tests, tensile tests and hardness tests are performed. For the microstructural examination, optical microscope, EBSD and EDS is done.

Following this short introduction, the next chapter will present the literature on welding and duplex stainless steel. In Experiments known properties specific to the pipe, how the specimens were machined, and how the tests were performed is presented. In Results the data of the examinations are presented and briefly described. In Discussions the data from Results are compared to Theory. At last, the Conclusion presents the main conclusions.

2 Theory

2.1 Duplex Stainless Steel

Duplex Stainless Steel (DSS) is a type of stainless steel that has about equal of ferritic and austenitic phases at room temperature, giving it its name. It is used in several industries: oil and gas, the paper industry and chemical storage. [1]–[4]

The balance of the DSS can be achieved with the right heat treatment and the right chemical composition. [4]

DSS is associated with a good ability to resist corrosion, due to its high chromium levels. DSS also tolerates better resistance to Stress Corrosion Cracking than pure austenitic stainless steels. But the high chromium can make the steel susceptible to chrome nitrides and chrome carbides that may make the steel brittle. It also has fewer alloying elements than some other stainless steels, making it comparably cheaper. [4], [5]

UNS S31308 begins melting at 1400°C and is completely melted above 1450°C. [6]

At 1250°C there are 80 to 85% ferrite in types of DSS with less than 0.2% nitrogen. [7]

2.1.1 Types of Duplex Stainless Steel

Lean duplex stainless steel is a duplex stainless steel with lower levels of nickel and/or molybdenum than other types of duplex stainless steels. To get the correct balance of ferrite and austenite, nitrogen and manganese is added. [8]

Standard duplex stainless steel contains 22 to 25% chromium and 2-3% molybdenum. Among the standard duplex stainless steel, 2205 is the most used. 2205 comes in two variants: UNS S31803 and UNS S32205. [8]

Super duplex stainless steel is duplex stainless steel with Pitting Resistance Equivalent number of 40 or higher. Hyper duplex stainless steels are more highly alloyed than super duplex stainless steel. [8]

2.2 Welding

Fusion welding are a set of welding methods that joins together pieces by melting them and letting the base material fuse together. There are four categories of fusion welding: Arc welding, gas welding, high-energy beam welding and resistance spot welding. [9], [10]

Gas welding is cheaper than arc welding and high-energy beam welding but doesn't have a high power density, so the heat spreads over a larger area. High-energy beam welding is more expensive than gas welding and arc welding, but has a high power density. This makes high-energy beam welding able to melt a deep area and weld it without the heat spreading deep elsewhere in the material. Arc welding is a compromise between low price and power density. [9]

Arc welding have several different methods associated with it: Shielded metal arc welding, tungsten-inert gas welding, plasma arc welding, metal inert gas welding, metal active gas welding, flux-cored arc welding, submerged arc welding, and electroslag welding. [9], [10]

2.2.1 Tungsten-Inert Gas Welding

Tungsten-inert gas (TIG) — also called Gas-Tungsten Arc Welding (GTAW) — is a form of arc welding. In TIG, there is a plasma arc between the tungsten electrode and the weld metal. The tungsten electrode is not consumed in the process. As it is not consumed, external filler material must be added if filler metal it is needed. [9]

As the filler metal is added manually, the welder has more control of the fraction between base metal and filler metal and doesn't have to melt more of the base metal to get the right solution between the two. TIG also has a small heat input, which makes it well suited to weld thin pieces together or to weld sections that needs multiple small passes. [9]

TIG has a heat source efficiency at about 0.7 when having the polarity where the electrode is negative. This is less than metal-inert gas welding — another form for arc welding, which has a heat source efficiency between 0.8 and 0.85. [9]

2.2.2 Heat-Affected Zone

The HAZ (heat-affected zone) may have a higher percentage of ferrite than the base metal. [7]

The HAZ can be divided into two zones: HTHAZ (high temperature HAZ) and LTHAZ (low temperature HAZ). The transitions between HTHAZ and LTHAZ becomes more complex with multipass welding. [7]

HTHAZ is found next to the fusion boundary, where the temperature approaches the melting point. In older DSS grades, the HTHAZ became almost fully ferritic, which reduced the corrosion resistance. In newer DSS grades there is an increased amount of nitrogen which lowers the fraction of ferrite from 50 to 70%, given that appropriate welding practices are used. [7]

The microstructure of the HAZ can be controlled by heat input, material thickness, preheat and interpass temperature. A high peak temperature and exposure time can cause austenite to dissolve into ferrite and cause bigger ferrite grains. [7]

One study found the HTHAZ if welded AISI 2205 to have 75-80% ferrite content. This caused the HTHAZ to be hard and brittle, especially in the colder temperatures. [11]

2.2.3 Unmixed zone

The fusion zone consists of two regions: a composite region and an unmixed zone. The composite region is where filler material and base materials mix together. In the unmixed zone the base material melts and solidifies without mixing with the filler material. If the base

material and filler metal are dissimilar, the composite and unmixed zone becomes different from each other. [12]

The unmixed zone is found along the boundary of the fusion zone, separating the composite region from the not melted material. It can have a different microstructure than the composite region. [12]

2.2.4 Filler material

Filler metal with a higher amount of nickel can be used to get a higher amount of austenite formation, thus a better austenite-ferrite balance, when welding duplex stainless steel. But it can cause a difference in microstructure depending on the depth of the material due to insufficient mixing between filler and base material when welded with electron beam welding. [8], [13]

Heterogeneous welds are welds where the filler metal has a different composition from the base material. [12]

Nickel-based filler causes nitrogen to migrate from HTHAZ to the fusion zone and causes a higher level of ferrite in the HAZ. [7]

2.3 Ferrite in Duplex Stainless steel

Duplex stainless steel becomes fully ferritic over 1250 °C. [14] Austenite begins to precipitate from the ferrite at temperatures lower than this. [7]

The HTHAZ can be fully ferritic in DSS. The weld metal also has a higher amount of ferrite than the base material. [7] One study that looked at super duplex in additive manufacturing found long ferrite grains that grew longer than the depth of the weld pool. [15]

Ferritic stainless steels are less ductile than austenitic stainless steels. [5]

2.4 Austenite in Duplex Stainless Steel

Austenite has a high ductility and fracture toughness, [4] but it also has a few weaknesses. If austenitic steel is in an environment that is too corrosive, it can experience Stress Corrosion Cracking. In addition to this, austenite only has a fatigue endurance limit at about 30% of tensile strength, while for ferritic it is between 50% and 60%. [2], [16]

If the austenite level is above 50%, the remaining ferrite gets enriched in chromium and molybdenum, which enhances the formation of the intermetallic phases. [7]

As austenite precipitate, it precipitates at ferrite grain boundaries as Widmanstätten or intragranular austenite. This process is slowed by large ferrite grains. If austenite forms in the fusion zone, it may cause nitrogen to migrate out of the HTHAZ, which increases the fraction of ferrite in the HTHAZ. [7] One study, which looked at the additive manufacturing

of super duplex stainless steel, found that the HAZ touched the fusion border and that the HAZ had a lower amount of austenite due to cooling down faster. [15]

The rate and amount of ferrite that transforms to austenite is determined on a couple of factors: the cooling rate and the amount of elements that encourages and stabilizes austenite in the area in question. [15] For example, if the steel gets heat treated for some time in high temperatures, the microstructure becomes isotropic, but with intermediate to rapid cooling Widmanstätten austenite may form. [7]

As the ferrite in the metal cools down, it becomes supersaturated in nitrogen. This may cause austenite to precipitate. Secondary austenite contains lower levels of the elements chromium, molybdenum and nitrogen than the other austenitic phases in the metal. [7]

The amount of austenite cannot be higher in the weld than what it would be if equilibrium was reached with annealing. If the filler metal has high levels of nitrogen and nickel, equilibrium levels of austenite can be achieved. Thus it is beneficial for the filler material to have more nickel content compared to the base material, often at 2-4%. [7]

Three types of austenite are found in the coarse ferrite grains in a simulated HTHAZ zone. These were allotriomorphic austenite, Widmanstätten austenite and intragranular austenite. [15], [17] These structures are also found in the fusion zone. [18]

Allotriomorphic austenite formed along ferrite grain boundaries as the steel cools down. It forms elongated shapes. Of the different types of secondary austenite, it is the one that formed the first. [14], [15], [17], [19]

Widmanstätten austenite formed when ferrite cools down, as at high temperatures duplex stainless steels became ferritic. Widmanstätten austenite formed at the boundary between ferrite grains or at the boundary of the allotriomorphic ferrite. It grew into the ferrite grains in parallel plates extending from the boundary. [14], [15], [17], [19]

Widmanstätten austenite can be formed during reheating between the passes in a multipass weld. It can be harder that other austenitic structures in the material as it has a higher amount of chromium and molybdenum. The root of a weld with multiple passes may have higher amounts of Widmanstätten austenite in it. [11]

Intragranular austenite formed within the ferrite grains. It precipitated at relatively low temperatures within the supersaturated ferrite matrix. They form clusters of small square-like grains. [15], [17] Reheating, which happens in multipass welding, may increase the amount of intragranular austenite. [11]

When the material was exposed to 700°C, the intragranular austenite got coarse and Widmanstätten grew. [17]

2.5 Intermetallic Phases

Intermetallic phases can be hard and brittle, and they can deplete the matrix of chromium and/or molybdenum — which again can increase the risk of corrosion. They can also make

the material brittle and reduce its fracture toughness. [2], [4] In addition, nitrides, chrome carbides, σ and χ can all form in the temperature range 550 – 1000°C. [20]

Because of precipitation, DSS shouldn't be subjected to temperatures above 250 to 300°C. [4]

2.5.1 Nitrides

Chrome nitrides (Cr_2N) can form at the grain boundaries and within the grains of austenitic steels exposed to air, while having a temperature over 600°C. [5]

One source says that at the temperatures between 600 and 750 °C, within 10 minutes it can form at ferrite-ferrite grain boundaries. If the temperature is held for longer, Cr_2N forms at ferrite-austenite grain boundaries and within ferrite grains. [20]

Another source says that if the temperature is held at 700°C for 5 minutes causes precipitation of 0.5-1μm long and 50 nm thick rods to form within the ferrite grains in HTHAZ. It also states that a prolonged exposure to elevated temperature — due to inappropriate heat treatment during welding or repeated exposure to the temperature range 600-750°C causes more nitrides to form in HTHAZ. [17]

Cr_2N causes areas depleted of chromium immediately surrounding it. [20]

Nitrides are particles that contains nitrogen that precipitates in the metal. Chromium nitrides (Cr_2N and CrN) tends to form on grain boundaries. [5], [7]

In high temperatures (above and around 1040 °C) ferrite allows nitrogen to be solved into it. If the material is then cooled down, the ferrite doesn't allow as much nitrogen to be solved in it, and Cr_2N precipitates within the grain. [7]

2.5.2 Chrome Carbides

Carbides are combinations of metals and carbon. $M_{23}C_6$ and M_7C_3 are two forms that can occur in duplex stainless steels. $M_{23}C_6$ forms at austenite-ferrite grain boundaries if the temperature stays between 950-1050 °C for over 10 minutes and the carbon concentration is over 0.02% C. M_7C_3 forms quickly between 650 and 950 °C at the grain boundaries if the carbon concentration is above 0.03% C. [7]

Chromium and Molybdenum are both elements that can form carbides and both are found in 2205. [5], [7].

A low cooling rate from 1000°C to room temperature to room temperature may promote the precipitation of chromium carbides. [21]

2.5.3 Sigma Phase

Sigma phase (σ) is a particle consisting of iron, chromium, and molybdenum. It has a tetragonal crystal structure and forms at between 600 and 1000 °C. [2], [7]

σ can form in Cr-Ni steels where there is more than 17% Cr, although increasing nickel hinders its formation. σ also prefers ferrite phase. Mo also accelerate σ phase. [5]

σ needs some time to form. In superduplex, at 900 °C, it may take only two minutes to form. In some austenitic stainless steels it may take up to 1500 hours for σ to form. [5], [7]

Just 1% σ in the steel can be enough to decrease corrosion resistance and impact toughness. The effect of σ is more severe than Cr_2N and χ. [20]

2.6 Alloying Elements

2.6.1 Carbon

Carbon in stainless steels can lead to carbide precipitation. Chromium rich carbides can act as the starting point for pitting corrosion and intergranular corrosion, as chromium carbides can precipitate at grain boundaries. Hence it is limited to 0,02% or 0,03% in duplex. [4], [7], [22], [23] Carbides can also cause embrittlement. [11]

Carbon is also a nickel equivalent, thus an austenite stabilizing element. [2]

2.6.2 Manganese

Manganese can make it easier for the material to absorb nitrogen and makes it harder for the nitrogen to leave the material. It also makes the metal more resistant to wear and increases the tensile strength without lowering the ductility. [7]

Manganese is a Sigma-phase enhancer. [7]

2.6.3 Silicon

Silicon is an element that increases the ferrite level. At high temperatures it increases the steel's resistance to oxidation and if the concentration is above 3.5 to 5.5% the material becomes less vulnerable to pitting corrosion. [2], [7]

Silicon can form some intermetallic phases and enhance others, such as the Sigma phase. These can be hard and brittle. [2], [7]

2.6.4 Phosphorus

Phosphorus is an impurity in stainless steel that can hinder the corrosion resistance. Ferrite dissolves it better than austenite does. [2], [7]

2.6.5 Sulfur

Sulfur hinders the corrosion resistance and thus needs to be kept low. Yet some needs to remain because it is useful for the weld bead penetration. Ferrite dissolves it better than austenite does. [7]

2.6.6 Nickel

Nickel is an austenite stabilizing element and thus increases the level of austenite. This can cause the ferrite level to decrease if the metal is heat treated after the welding. This can cause a higher concentration of elements that forms Sigma-phase in the ferrite, which can increase the chance that a Sigma-phase will form. [7]

The ferrite in DSS has at least 3% nickel, in contrast to fully ferritic stainless steels, which has low levels of nickel. [7]

2.6.7 Chromium

Chromium covers the steel with a passive film, which makes the steel more resistant to corrosion. Higher levels of chromium increase how much intermetallic phases precipitates in the metal by accelerating their formation and expanding the temperature range where they can form. Chromium also stabilizes ferrite. [4], [7], [23]

Chromium is a Sigma-phase enhancer. [7]

2.6.8 Molybdenum

Molybdenum gives resistance to pitting and crevice corrosion in an environment. [7]

However, between 300 and 1000°C, it increases the precipitation of α', σ and chromium nitrides by widening the range of temperatures where they can form and accelerate their formation. This can lower the fracture toughness and make the material brittle. [4]

2.6.9 Nitrogen

Adding nitrogen improves stabilization of austenite at higher temperatures and it enhances re-precipitation. [17]

Fracture toughness and corrosion resistance is increased with nitrogen. [4]

Nitrogen increases petting resistance, austenite content and strength. Increasing the nitrogen content reduces the risk of nitride formation by increasing austenite content as there is less distance between the areas of austenite. [7]

2.6.10 Copper

Copper is an element that can be added to stainless steels to make the material more resistant to sulfuric acid. [2]

2.7 Mechanical Tests

2.7.1 Vickers Hardness

Vickers hardness is measured using the formula:

$$HV = 1.854\frac{F}{D^2}$$

Where F is the force in kgf (kilogram force) and D^2 is the area of indentation in mm squared. [24]

If S31803 is heated to 1300°C and rapidly cooled they get a higher hardness and lower toughness compared to if it was cooled at a slower rate. Cr_2N, which is formed during fast cooling, also causes higher hardness and lower toughness. Oil cooling causes a hardness of 288 ± 3.1 HV. [21], [25]

Microhardness in Vickers hardness is hardness where a light load (10g to 1kg) is applied to the material. [26]

Low cooling rate can increase the microhardness in ferrite. [21]

An increased amount of sigma phase causes an increased amount of hardness. [27]

Annealed UNS S31803 has a Brinell Hardness at 260 HB, which for steel is equivalent to 260 HV in Vickers hardness. [6], [27], [28]

The base material certificate in 8.1.2 reports a hardness between 218 and 228 HV.

2.7.2 Impact Energy

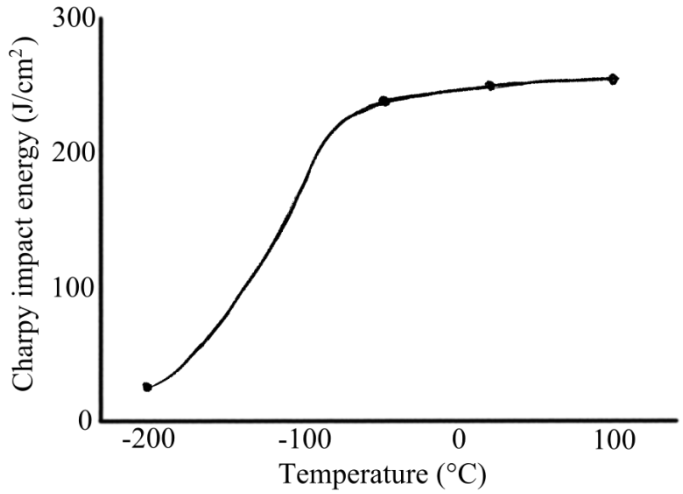

Figure 1 Charpy impact energy at different temperatures for normalised stainless steels. Illustration based on graph at page 64 in [7]

Figure 1 shows S31803 at 12 mm thickness and S31803. Figure 1 is based on figure 5.9 at page 64 in [7]. The material referenced in the graph is unwelded and solution annealed [7].

There is a decreased impact toughness with an increased fraction of ferrite in the HAZ. If a nitrogen-containing 2205 DSS has experienced a high peak temperature and then a fast cooling rate, the material in the weld gains a higher ferrite fraction. [17]

UNS 31308 that has been heated to 1300°C and then rapidly cooled has a higher hardness and lower impact toughness than if it was more slowly cooled. If it was quenched in water, it got an austenite fraction of only 17.1%. If it was quenched in oil, it got an austenite fraction of 27.6%. The fracture surface contained a patchwork of brittle and ductile portions. [21], [25]

One study aged samples for 10 minutes at different temperatures and then tested them with Charpy V-notch test. The Charpy test was tested at -40°C and at $10 \times 10 \times 55\ mm$. When aged at the temperature range 450-500°C, the impact toughness was at 270 J (interpreted from a graph). This was almost the same as for the specimen that had undergone solution-annealing at 1050°C. When the samples had been aged in the temperature range 600-950°C, they had a lower impact toughness than the solution-annealed samples. They had an increased amount of embrittlement and precipitation of the secondary phases Cr_2N, σ and χ. The toughness impact was the lowest for the sample that had been aged at 850°C, where the results dipped below 50 J. This sample had 1.2% σ-phase.[20]

Another study that looked at welded AISI 2205 showed a 40% reduction (153 J) in the results for the Charpy impact test compared to the base material. Their base material had the following chemical composition: 0.027% C, 1.463% Mn, 0.42% Si, 0.01% S, 0.02% P, 22.8% Cr, 5.5% Ni, 3.3% Mo, 0.1% Cu, 0.18% N, and 0.134% other alloying elements. It uses the dimensions $7.5 * 10 * 55\ mm$ for the samples. [11]

2.7.3 Tensile Strength

Ultimate tensile strength is calculated by $\frac{Maximum\ load}{Original\ cross\ section} = \frac{P_{maximum}}{W \times T}$ in rectangular specimen. $P_{maximum}$ denotes the maximum tensile load on the sample. W and T denotes the width and thickness of the original cross section. [29]

According to standard AWS B4.0 — in samples where the weld is normal to the tensile stress — yield strength, elongation, or reduction in area is not reported. Only ultimate tensile strength is reported. This is because the strain during testing along the specimen is not uniform during yielding. [29]

One source expects ultimate tensile strength of the base material to be 710 MPa. [6] The base material certificate at 8.1.2 gave the results 702-777 MPa.

If the weld has been welded with duplex filler, it does not struggle with meeting the tensile strength values that are required for the parent material. If a nickel-based filler is used, it may cause the weld to become fully austenitic, which reduces the tensile strength. [7]

Ferrite gives a higher tensile strength than austenite. Without filler wire, desired tensile strength was typically unproblematic to reach, due to a high ratio of ferrite. [13]

If the material is fully austenitic, it gets a lower tensile strength. If there are intermetallic phases the ductility can be lowered. The elongation can also be less than that of the base material. [7]

3 Experiments

3.1 Material

The object that contains the weld and the material is a pipe. The pipe was welded together using TIG welding, as specified in the WPS located in appendix at 8.1.1. Figure 2 shows the pipe before the work on making the specimen began.

Figure 2 Picture of the pipe the way it looked before machining.

3.1.1 Specifications of the Pipe

Length of pipe: about 450 mm

Outer diameter of pipe: 170 mm

Wall thickness: 11.1 mm measured, while the material certificate at 8.1.2 says 10.97 mm.

3.1.2 Composition

Table 1 shows the composition of the base material and the filler metal, as described in the material certificate for the base material found in 8.1.2 and the material certificate for the filler material found in 8.1.3. The base material is the duplex stainless steel grade UNS S31803.

The filler material has more nickel, manganese, silicon, carbon and chromium and less nitrogen than the base material. The difference is the greatest in nickel, where the difference is 3.05%.

Table 1 The composition for the base metal and the filler metal in w%

Element	C	Mn	Si	P	S	Ni	Cr	Mo	N	Cu
Base metal	0.018	1.02	0.270	0.027	0.0005	5.55	22.45	3.17	0.1669	
Filler metal	0.02	1.4	0.4	0.020	0.002	8.6	23.2	3.2	0.15	<0.1

3.1.3 Weld

As specified in the WPS at 8.1.1, the buttweld was welded with welding process 141 (called TIG or GTAW). Argon was used as a shielding gas during welding.

The weld goes around the entire pipe as it welds the two pipe pieces together.

It is welded in multiple passes and cooled down to 150°C between the passes.

3.2 Optical Microscopy

3.2.1 Hot Mounting

The samples used for microscopy were first cut to 45 mm as to fit in a 50 mm diameter form. The form was formed by encapsulating the sample with powder, which was then compressed at 250 bar at 180°C. Two layers of dust were used: multifast around the sides of the sample and condufast under the sample. Condufast was used because of the electropolising etching with NaOH. [30]

3.2.2 Polishing

For polishing Struers method D was used, except the last step. The steps used are detailed in Table 2.

The polishing was done using Struers TegraForce-5.

Table 2 The steps used for grinding and polishing the samples.

Plate	Lubricant	Particle size
Piano	Water	1200 grit
Allegro	DiaPro Allegro/Largo	9 μm
Dac	DiaPro Dac	3 μm

3.2.3 Electropolishing

Electropolishing:

- 10% oxalic acid in 10 seconds at 5.5 V
- Cleansing of apparatus and sample with first water then ethanol then drying
- 20% NaOH in 8 seconds at 3.0 V
- Cleansing again

All three samples were electropolished with the oxalic acid step before the NaOH electropolishing was done. Table 3 and Table 4 shows the values recorded while electropolishing. The apparatus used for electropolishing was a Struers LectroPol-5.

Table 3 Values recorded for electropolishing with oxalic acid.

Sample	Etchant	Current	Temperature
Side-view sample	Oxalic acid	0.46 A	22°C
Bottom-view sample	Oxalic acid	0.44 A	22°C
Base material	Oxalic acid	0.41 A	22°C

Table 4 Values recorded for electropolishing with NaOH.

Sample	Etchant	Current	Temperature
Side-view sample	NaOH	0.21 A	21°C
Bottom-view sample	NaOH	0.13 A	22°C
Base material	NaOH	0.16 A	22°C

3.3 Vickers Hardness

A force of 1 kgf was used for all three samples. This light force was chosen as to hopefully get at least one imprint in the HAZ each time the machine crossed a weld. The distance between the test was determined by the size of some test imprints done on the base material sample.

The distance between the imprints should according to ASTM E384 [31] be at least 2.5 times the diagonal of the imprint mark. Three different forces were tested on the base material sample, before the pattern testing in 4.2:

- 10 kgf, where the distance between imprints could be 0.75 mm
- 5 kgf, where the distance between imprints could be 0.5 mm
- 1 kgf, where the distance between imprints could be 0.25 mm

The hardness tests were done automatically by the hardness test machine.

The samples are the same as the ones used for optical microscopy. The preparation is described in 3.2.1 and 3.2.3.

3.4 Charpy Impact Test

3.4.1 Machining

The process with making a Charpy test specimen begun with cutting a section of the wall using a band saw, where the inner width is at least 10.5 mm. This is done to be able to follow the AWS B4 standard, where the dimensions are $10 * 10 * 55\ mm$.

The sections cut out had to be wider than 10mm at the bottom, but not so wide as to cause the length from the top to the bottom to fall under 10mm as they were milled to get a square cross section.

The specimens were then cut with a smaller band saw to get the length of 55-60mm, with the weld in the middle of the specimen.

Then the specimens were milled. At first, they were milled to get the cross section to be rectangular. Then they were milled to get the cross section to a square shape with the dimensions between 10.2 and 10.5 mm.

As a last step, the notch was carved out by CNC. Figure 3 shows how the weld is oriented in the sample compared to the notch.

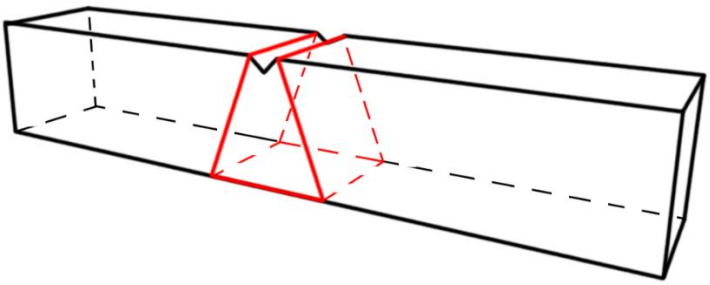

Figure 3 Illustration of orientation of weld in Charpy impact test.

3.4.2 Testing

Three of the Charpy specimen was cooled down to -46°C, using a coolant consisting of ethanol and glycol. The cooled down samples were named C1, C2 and C3. The samples had to be rapidly moved from the cold bath to the machine (around 5 seconds) with a tong to have the temperature be as close to -46°C as possible.

The other three was tested at room temperature. The samples were named R1, R2 and R3.

The Charpy tests were tested with the machine showed in Figure 4. The machine is a Zwick/Roell RKP 450. The samples were put into the machine with a tong.

Figure 4 The Charpy test machine.

3.5 Tensile Test

3.5.1 Machining

The machining was done following the work drawing in Figure 5.

When the material to become the specimen were sawed out of the pipe, it had to have the thickness of 9.0 mm, with 0.5 mm tolerance. This limited how wide the specimen could be as the thickness of the pipe is about 11 mm thick. The specimen also had to be milled so that they had a rectangular cross section. The width outside of the reduced section had to be wider than that within the reduced section. The outer width was sawed to be about 30 mm. Figure 6 shows how the tensile specimens were located within the pipe walls and the curvature of the pipe walls around them.

The work drawing in Figure 5 was made for the latest step in the machining, as the samples were machined into the correct shape with CNC.

The measures are based on the AWS standard B4.0 from 2016.

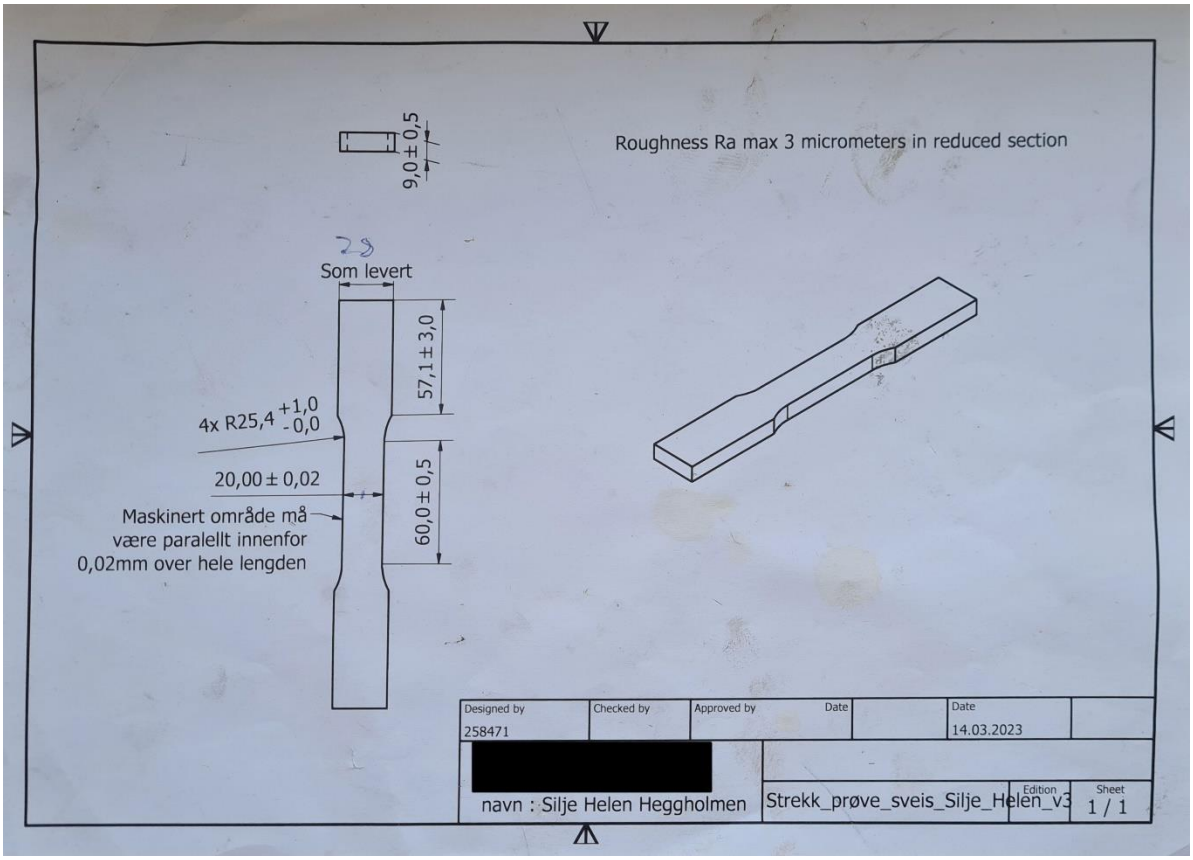

Figure 5 Work drawing for the tensile tests.

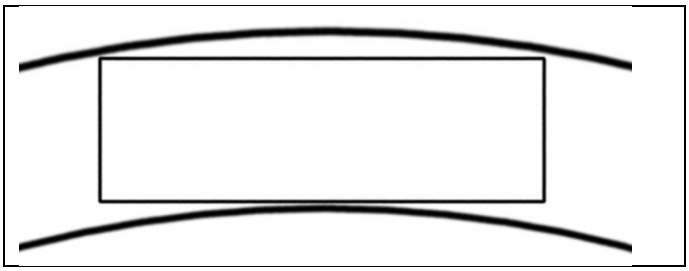

Figure 6 Tensile specimen within the wall of the pipe.

3.5.2 Testing

The testing was done with an Instron tensile test machine. Due to there being a weld transverse to the tensile load, the yield strength and Young's modulus were not measured as the material wouldn't be homogeneous. Ultimate tensile strength and the stress against strain was measured.

Figure 7 The clamps of the tension test device.

There was first a dummy test that was stretched by the machine to calibrate it. Then three tests of the material within the tolerances of the drawing above. The tests were held in place as seen in Figure 7. The tensile test device is made by the company Instron.

The weld was in the middle of the reduced section.

3.6 SEM

3.6.1 Preparation

The sample was first cut below the length of 40 mm because 40 mm was the biggest size that would fit into the SEM. A bit of base material was left on both sides.

The sample was hot mounted in a 40 mm diameter cast with polyfast. It was hot mounted by CitoPress-30. Figure 8 shows the sample in the cast after polishing. The hot mounting was done at 180°C and at 250 bar.

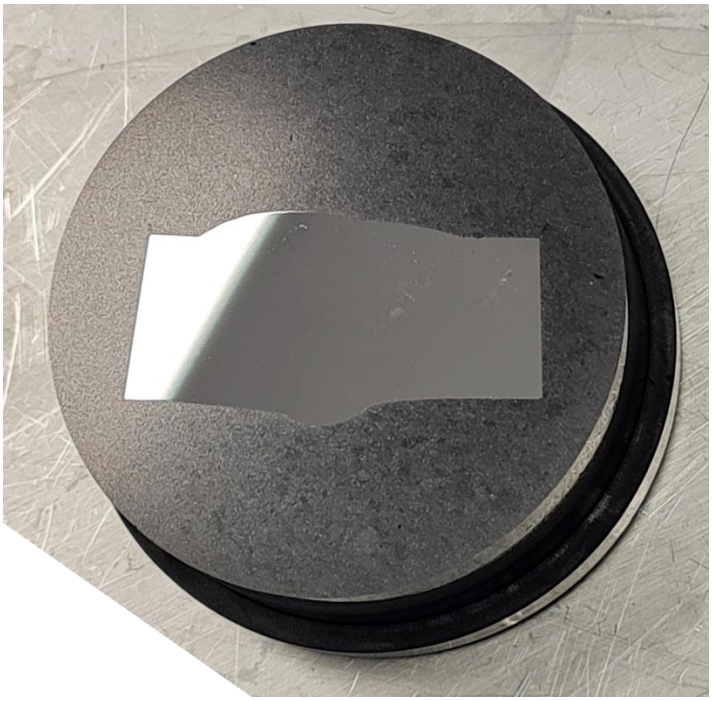

Figure 8 Sample after polishing.

The polishing was done in five steps. If something went wrong or the result for the step wasn't good enough, the step was repeated. The polishing method is shown by Table 5, which was done by Struers TegraForce-5.

Table 5 Overview of the polishing method.

Plate	Lubricant	Particle size	Duration [minutes]
Piano	Water	1200 grit	3
Allegro	DiaPro Allegro/Largo	9 μm	3
Dac	DiaPro Dac	3 μm	6
Dur	DiaPro Nap-B	1 μm	8
Chem	OP-S		10

Between the steps, the samples were cleaned with an apparatus called Struers Lavamin that used ultrasound to clean them.

3.6.2 EBSD

The model used for the SEM testing was a Supra 35 VP made by the company Zeiss. The detector used was a NORDIF EBSD detector and the software used to analyze it was EDAX OIM Analysis.

EBSD was done to get a clearer view of the distribution of austenite and ferrite in the microstructure. Both IPF, phase map and data on grain size distribution was generated.

There were taken 6 images: One in the root, one in each HAZ, one in the center of the weld and two in the top.

The root weld image was taken at a distance at maximum 0.5 mm from the edge of the sample. Similarly, the image closest to the top was taken at a distance at maximum 0.5 mm from the top of the sample. The image at the center was attempted taken in the center of the weld, but it was few ways to know how close to the center it was.

The HAZ images were taken somewhere in the transition between weld metal and base material, but it is unsure exactly where. It is also uncertain where one of the images closer to the top/cap was taken. It has been called Weld cap – lower.

EBSD images was made at the cap of the weld, the transition area from weld to base material, the middle of the weld and near the root of the weld.

3.6.3 EDS

The same sample was used for EDS as was used for EBSD. Supra 35 VP by Zeiss was used for EDS as well. The detector used was EDAX Octane Elite and the software was EDAX Team.

The EDS was done to find the chemical composition of particles in order to find intermetallic phases like carbides.

3.7 Safety

Safety goggles were necessary for milling, sawing, tension testing, Charpy impact testing, hot mounting, polishing and electropolishing. It was mandatory to keep the safety goggles on all the time in the sample preparation lab.

Hearing protection was used whenever the noise was loud. Hearing protection was mandatory for the tensile testing.

Operations where extra safety equipment was needed:

- Milling: shield mounted on the machine, overalls
- Electropolishing: nitrile gloves

Necessary HSE courses were taken.

4 Results

4.1 Optical Microscope Results

4.1.1 Base Material Sample

Figure 9 shows the microstructure in a sample without a weld. The austenitic and ferritic phase forms stripes. Scale bar shows $20\ \mu m$. The lighter structures are here the austenite.

Figure 9 Image of the microstructure in the base material.

4.1.2 Side-View Sample

Figure 10 shows an overview of the weld in the Side-view sample. The image consists of a patchwork of smaller images. The root pass goes darker as it gets closer to the edge of the sample. Several passes can be seen. Visually it may look like there are 6 or 7 passes. Some beads look like they have some darker lines on them. The edges of the samples look darker. Figure 11 is a zoomed in sand cropped image taken from Figure 10.

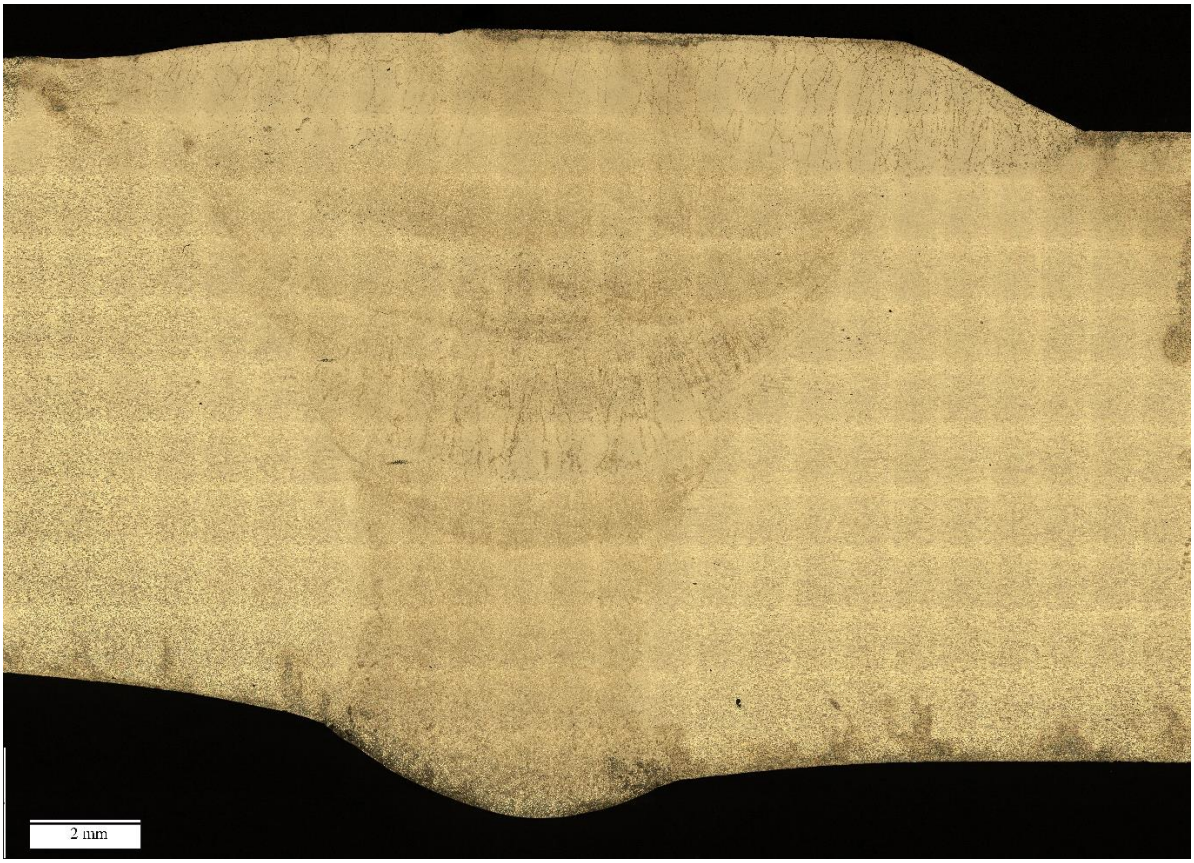

Figure 10 Overview of the weld in the Side-view sample. The blue edges of the rectangle shows where Figure 11 is taken from.

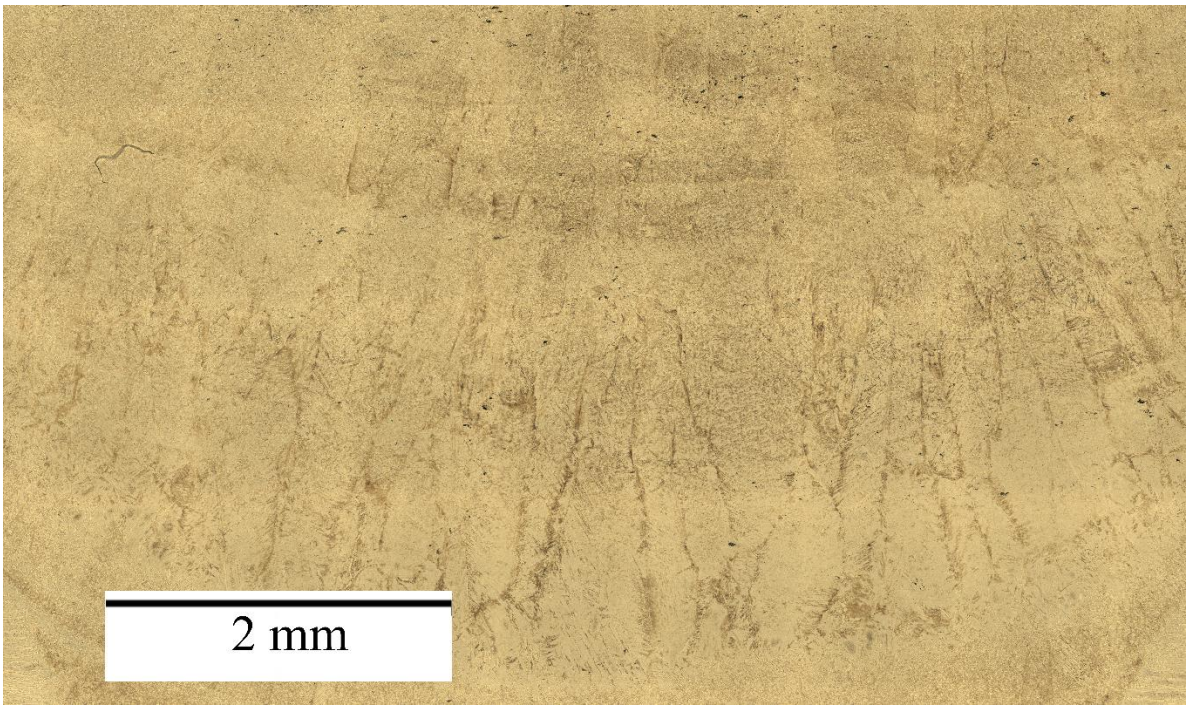

Figure 11 Zoom in on the middle of the weld.

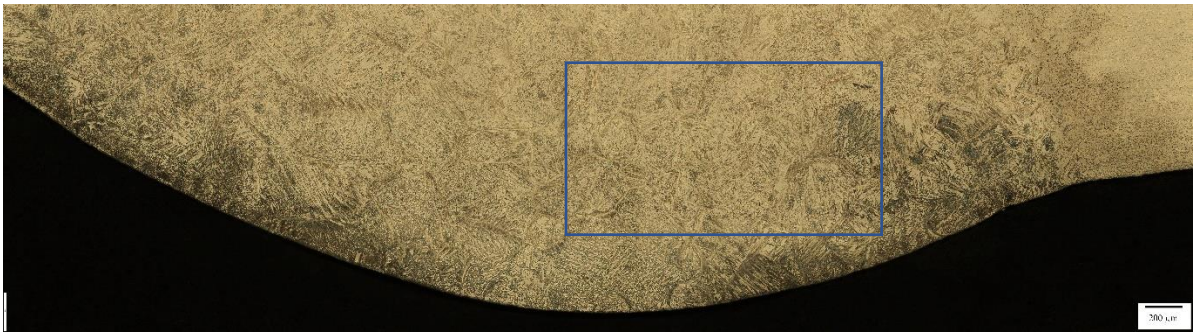

Figure 12 Overview of the root of the weld in the Side-view sample.

Figure 12 shows a patchwork overview of the root of the weld in the Side-view sample. It appears to be darker on the edges on the sides of the root pass. The scale bar is a bit too small to let the numbers be seen clearly, but it says $200\ \mu m$.

Figure 13 Closer look at the microstructure in the root pass.

Figure 13 is a screenshot of a zoomed in and cropped version of Figure 12, where the scale bar is the same size compared to sample and only moved as to not be cropped out. Figure 13 shows Widmanstätten structures and allotriomorphic structures. Figure 13 also shows some darker areas. The blue rectangle in Figure 12 shows where Figure 13 is taken from.

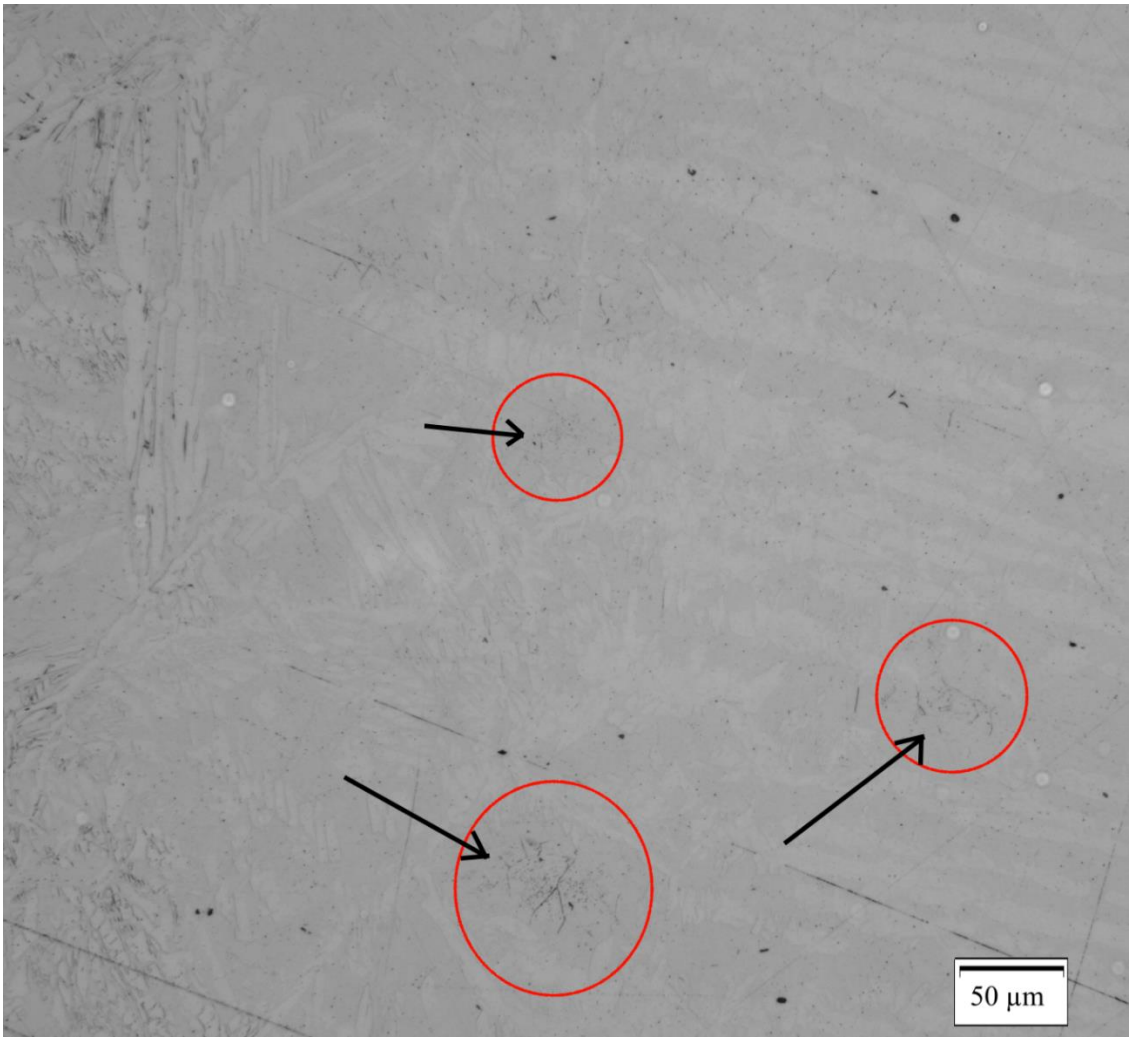

Figure 14 Image of the transition between weld and base material. Arrows points to nitrides.

Figure 14 shows a bit of the weld pool, a bit of the base material and the area between the two. In this area, in the areas of slightly darker grey, there are some nitrides which are marked with arrows. The recorded image is grey scale. Ferrite is here slightly darker, and austenite is here slightly brighter.

To the further left of the image there are some darker areas on the grain boundaries. These darker areas are not found in the area in the middle and the area to the right. The area to the right looks to the base material. There are multiple places in the middle region with nitrides, but only three are marked with red rings and black arrows.

4.1.3 Bottom-View Sample

Bottom-view sample shows a section into the root pass. Figure 15 shows an illustration of the placement and orientation of the weld in Bottom-view sample. The light red shaded area is the weld, and the grey shaded area is the base material. The root was focused on because the notch at the Charpy tests was placed at the root-side of the sample.

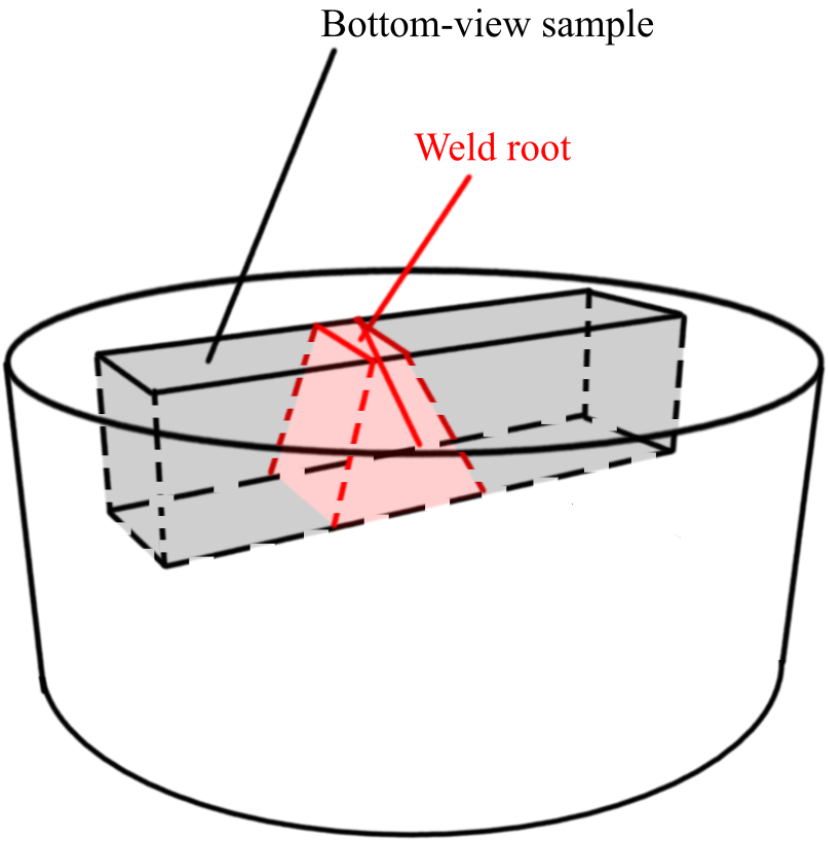

Figure 15 Illustration of the Bottom-view sample's orientation and placement in mold.

Figure 16 is a picture from when the Bottom-view sample was only etched with oxalic acid. Figure 17 is a zoomed in and cropped image of Figure 16, focusing on the edge of the weld. Both show a gradient from lighter color in the middle to darker color at the edge of the weld/sample. Figure 17 shows what appears to be brighter area on the grain boundaries — allotriomorphic austenite. Possibly some Widmanstätten austenite can be seen as well.

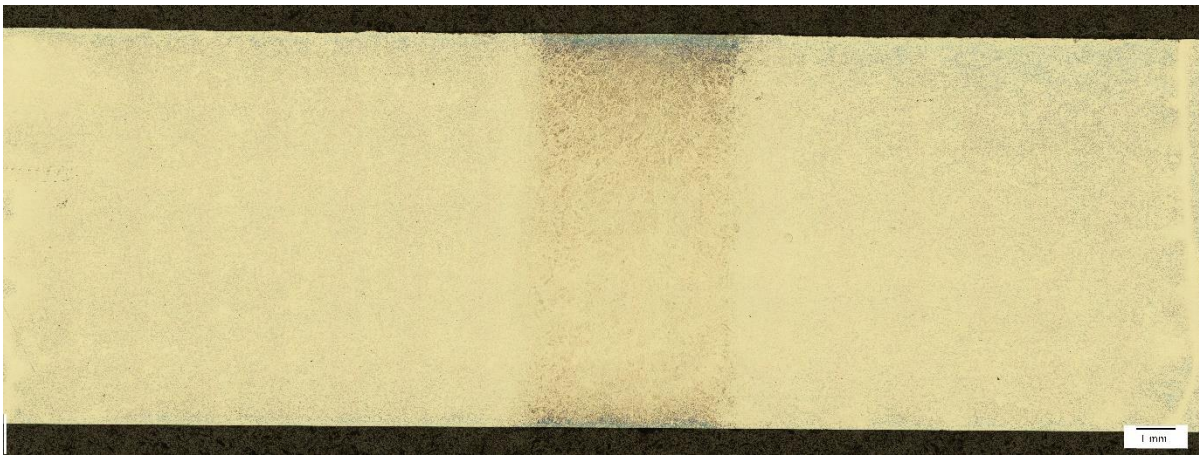

Figure 16 Overview of the Bottom-view sample. The edges of the sample at the weld is darker.

Figure 17 Zoomed in version Figure 16 showing the edge of the sample. It shows some allotriomorphic austenite.

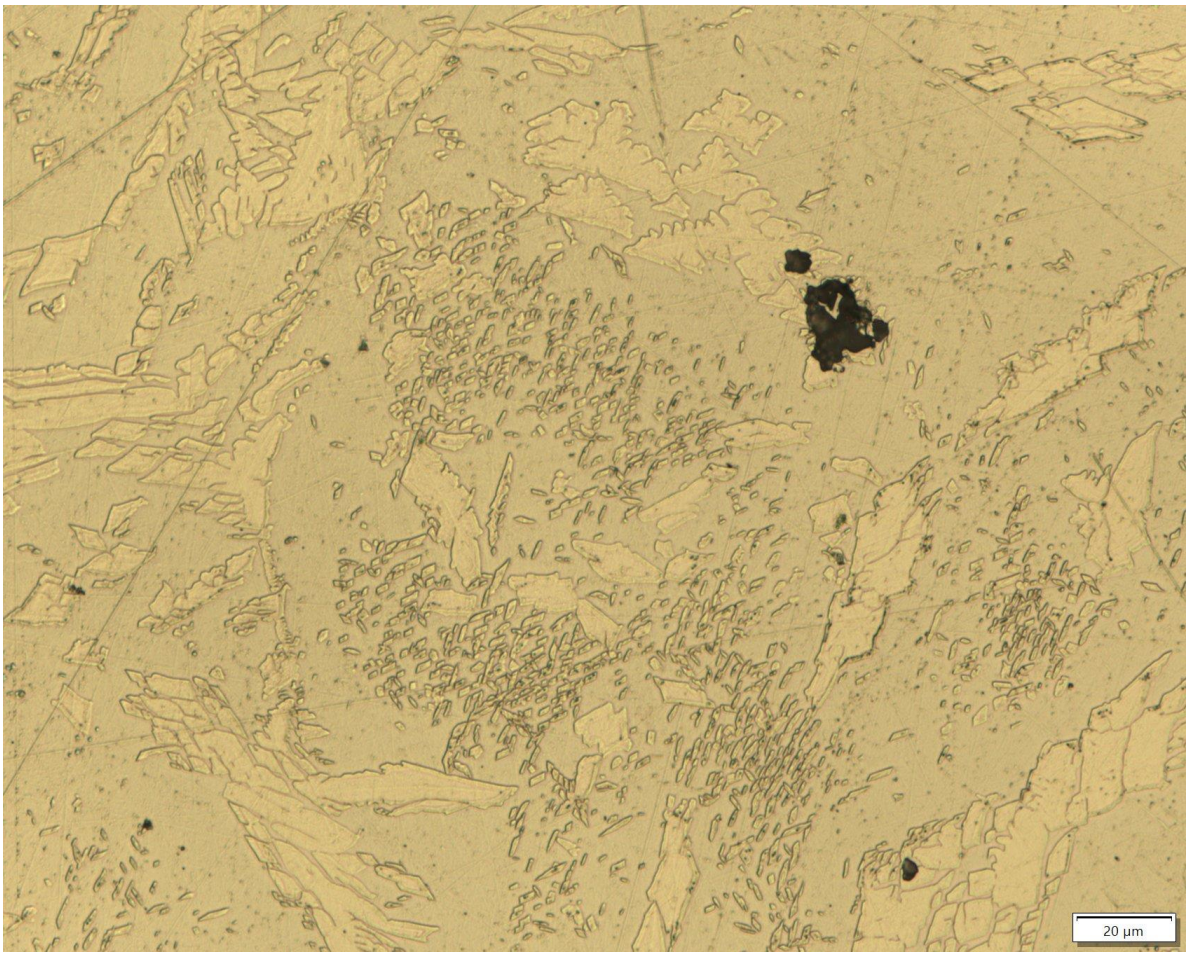

Figure 18 Image of the Bottom-view sample showing intragranular austenite.

Figure 18 and Figure 19 are pictures from the Bottom-view sample after it was polished again and etched with oxalic acid and NaOH.

Figure 18 shows clusters of small intragranular austenite between bigger austenite structures. These structures may also be intragranular austenite. There appears to be dark lines separating the ferrite and the austenite.

Figure 19 shows nitrides within the metal, located in the HAZ. There is mostly ferrite within the image.

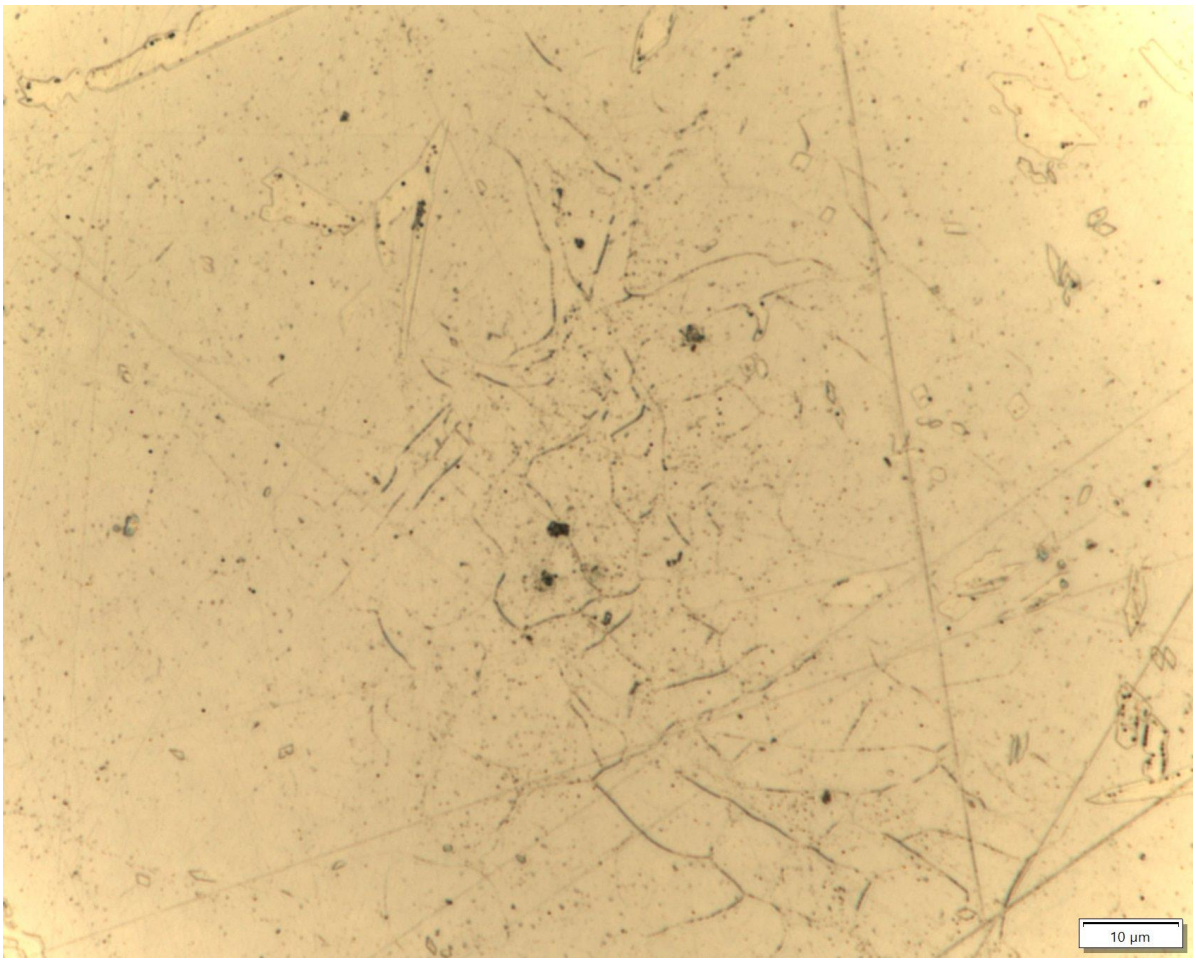

Figure 19 Image of chromium nitrides in the ferrite in the Bottom-view sample.

4.2 Hardness

4.2.1 Results from Base Material Sample

Results for base material sample Table 6 shows the mean, minimum, and maximum results for the Vickers hardness test of the base material. All of the values are beneath 300 HV and above 230HV.

Table 6 Mean, min and max values for base material hardness test.

Mean	Min	Max
253	234	292

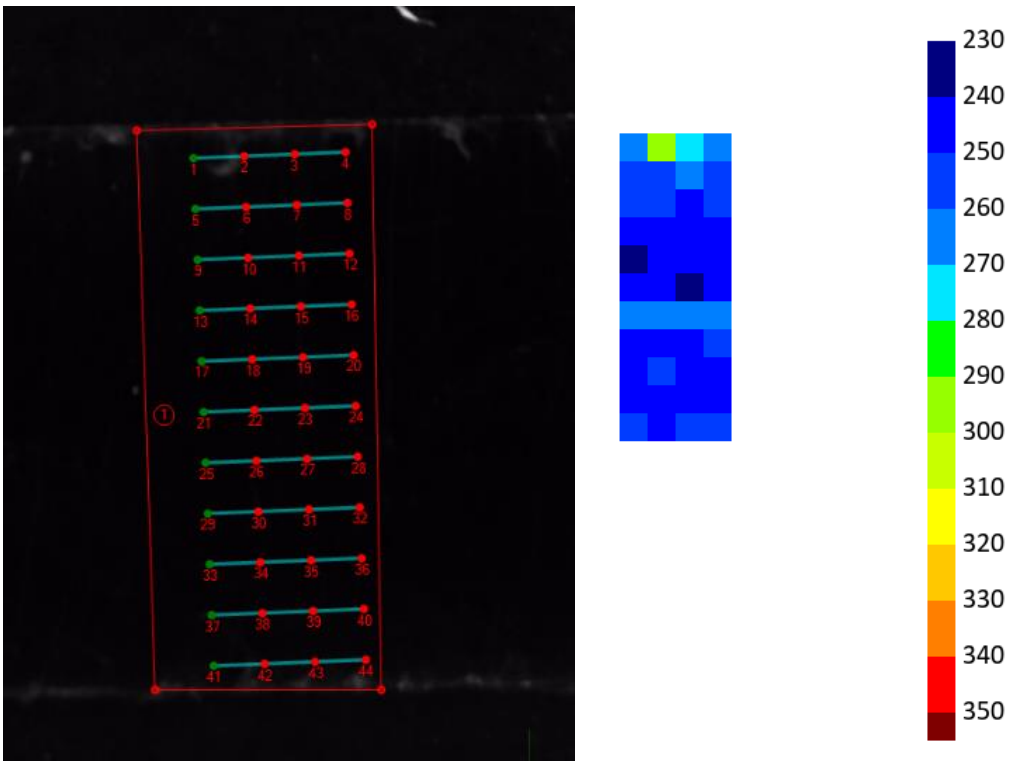

Figure 20 a) Pattern the hardness test was done in. b) A map of the hardness test results

Figure 20a shows the pattern the hardness test machine used over the sample, doing 4 tests for each of the 11 lines.

Figure 20b shows a map of the values, one number per point on the planned map. The values are mostly between 240 and 250, with some exceptions with higher values. Test spot 2 got a value between 290 and 300. Line 7 from the top got all values between 260 and 270.

4.2.2 Result from Side-View Sample

Figure 21 shows a map of the values from the Vickers hardness test. During the testing, the computer powering the hardness tester crashed, thus some tests were not done. The missing data is market in magenta/dark pink. Table 7 shows that the lowest value is 198, which is below any other number in the set and is thus not illustrated in Figure 21, but replaced with a dark blue color.

Table 7 The mean, min and max value for weld Side-view sample hardness.

Mean	Min	Max
271	198	307

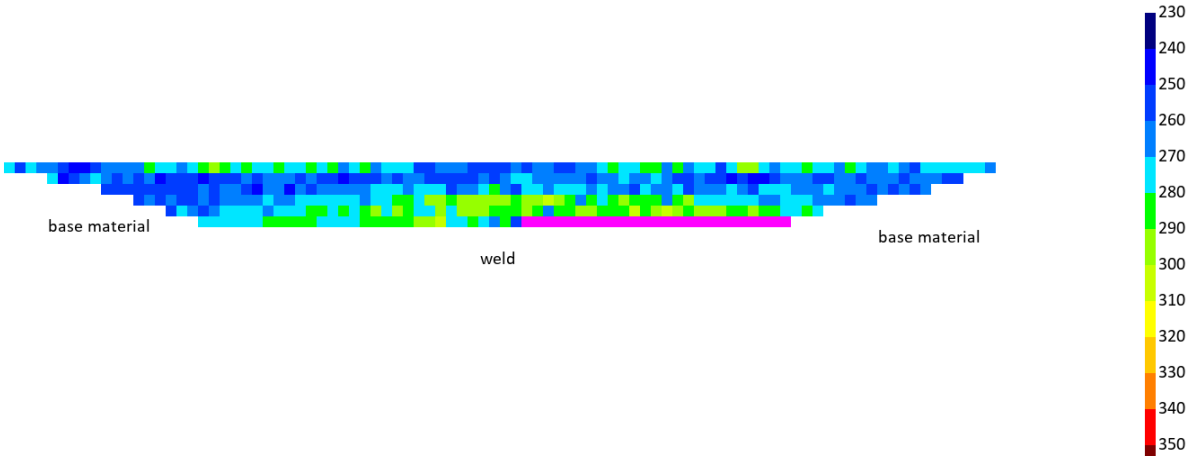

Figure 21 Area map for hardness results for the Side-view sample.

Figure 22 and Figure 23 shows the planned pattern for the tests over the material. Figure 22 shows the actual picture of the weld, while Figure 23 is a sketch to make it clearer where the weld is compared to the tests.

Figure 21 can be seen as having different sections. The middle of the three lowermost lines, the spots that are green and yellow-green aligns with placements on the lines that are a bit wider than weld — based on Figure 22 and Figure 23. They have the highest values near the middle — around 300 HV. The two lines have lower values near the ends of the specimen, where the color corresponds to around 260 HV, which is almost as low as measured at the base material.

The second and third line from the top doesn't change very much in value depending on where they are. The top line has a lower value in the middle, but higher values both to the right and the left at the toes of the weld.

The two lowest lines go over the root pass and the second pass. The three upper lines go over the fill passes and the weld cap.

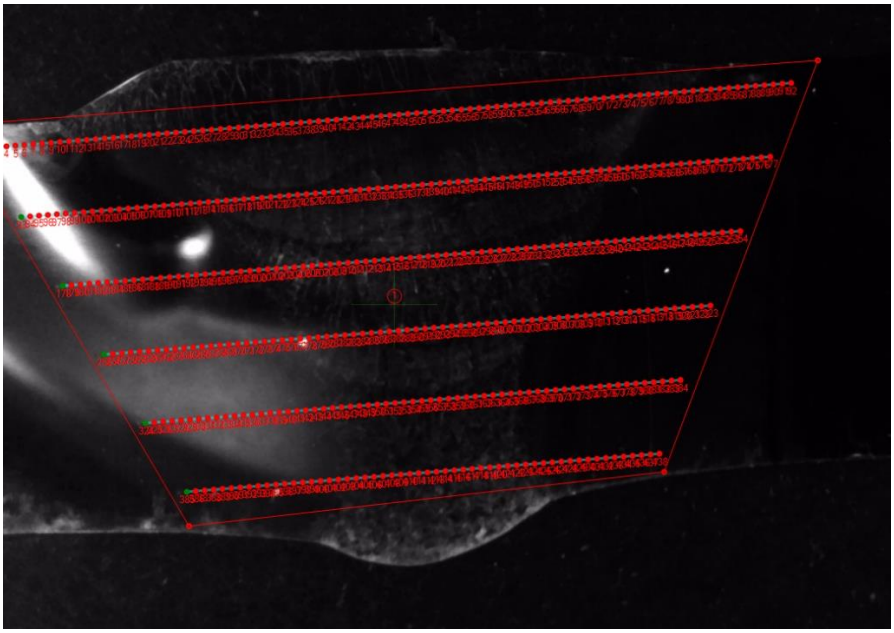

Figure 22 The pattern of which the hardness test was done.

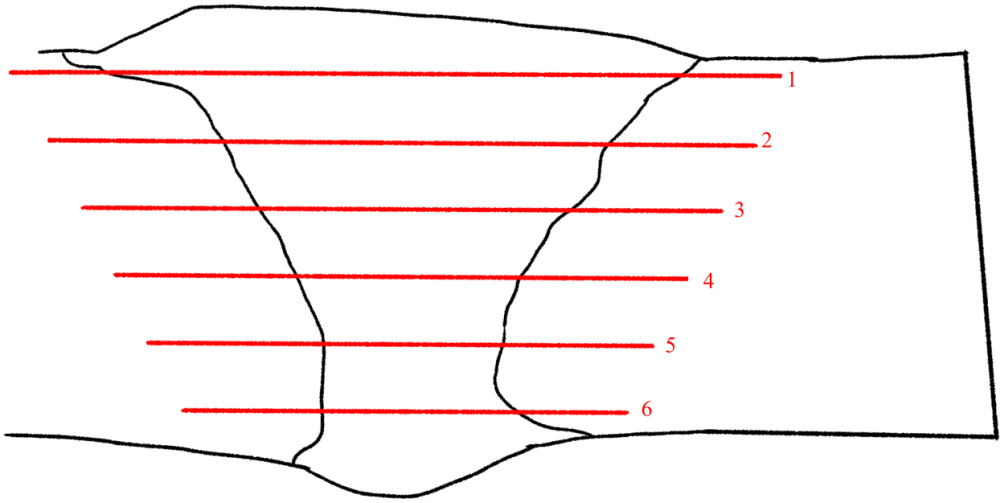

Figure 23 Sketch of the hardness test pattern over the weld.

4.2.3 Result from Bottom-View Sample

Table 8 shows the mean, minimum, and maximum values for the hardness test for the Bottom-view sample. The lowest value is higher than the mean value for the base material specimen.

Table 8 Table showing mean, min and max values for hardness values for the Bottom-view sample.

Mean	Min	Maks
296	262	338

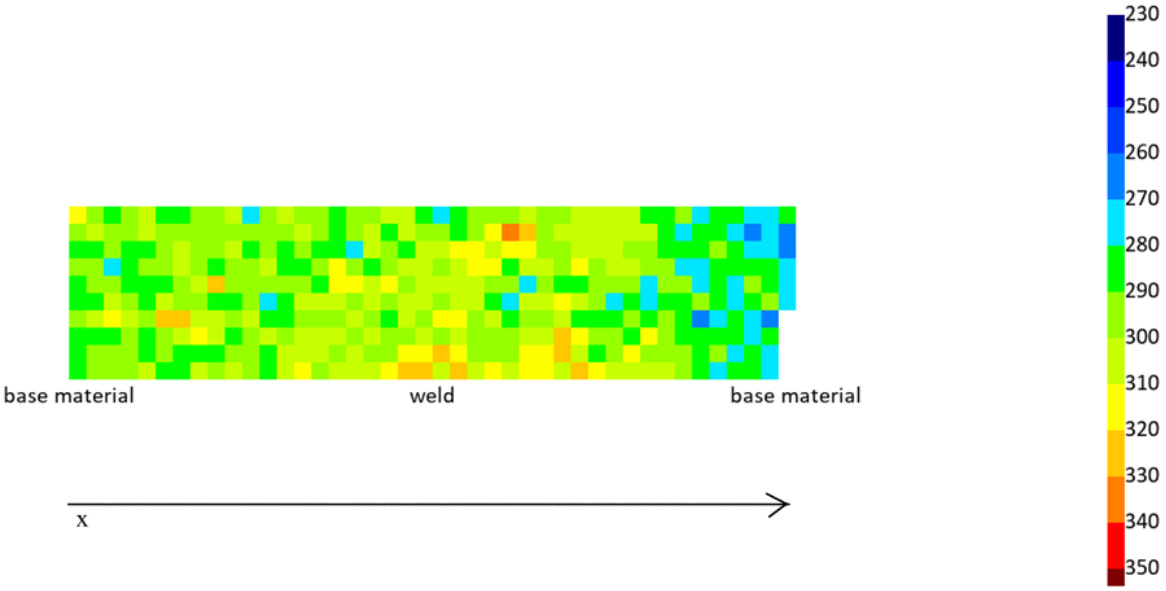

Figure 24 Area map of the hardness results for the Bottom-view sample.

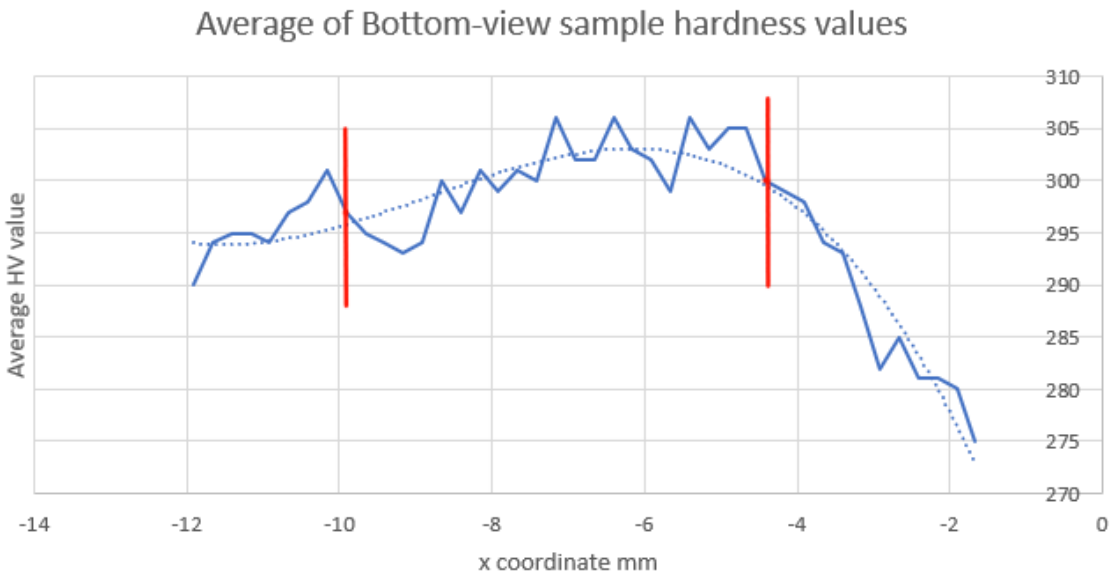

Figure 25 Average hardness value per location in x direction for the Bottom-view sample.

Figure 24 shows the area map of the hardness values. The values on the right side of the weld are lower than the values on the left side of the weld for this sample.

Figure 25 shows the average of the different values per x location (left to right on Figure 24). The red lines show where the weld transitions to base metal, where the weld is between the

two red lines. The graph shows a decline in hardness values as the position moves away from the weld. This decline is sharper on the right side on the graph than the left side on the graph.

Figure 26 is a picture of the Bottom-view sample showing the pattern that the hardness tester used. The red lines show the ends of the lines the hardness tester made and the cyan/turquoise lines show where the weld is in the Bottom-view sample. For some reason the picture of the pattern of the hardness test was missing from the files, thus this picture was taken as a replacement.

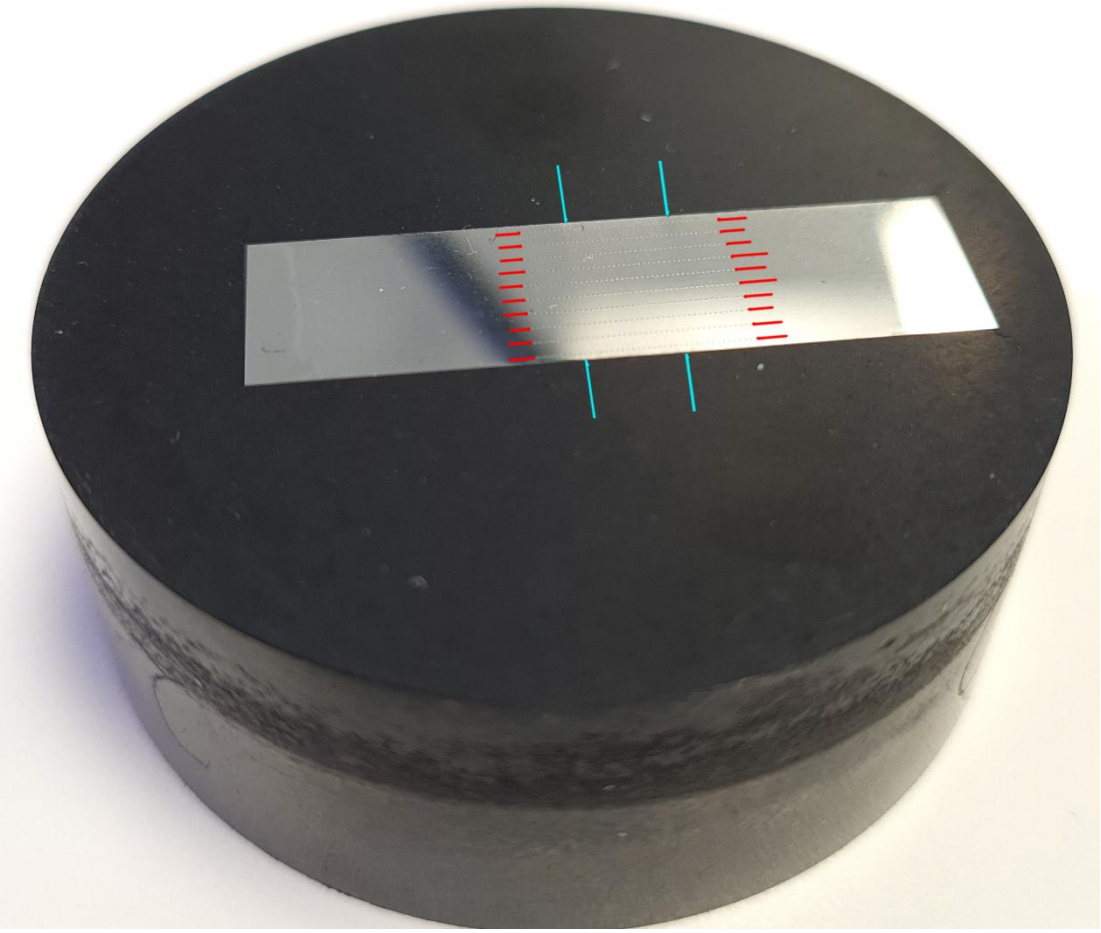

Figure 26 View of Bottom-view sample after hardness testing.

4.3 Charpy Impact Test

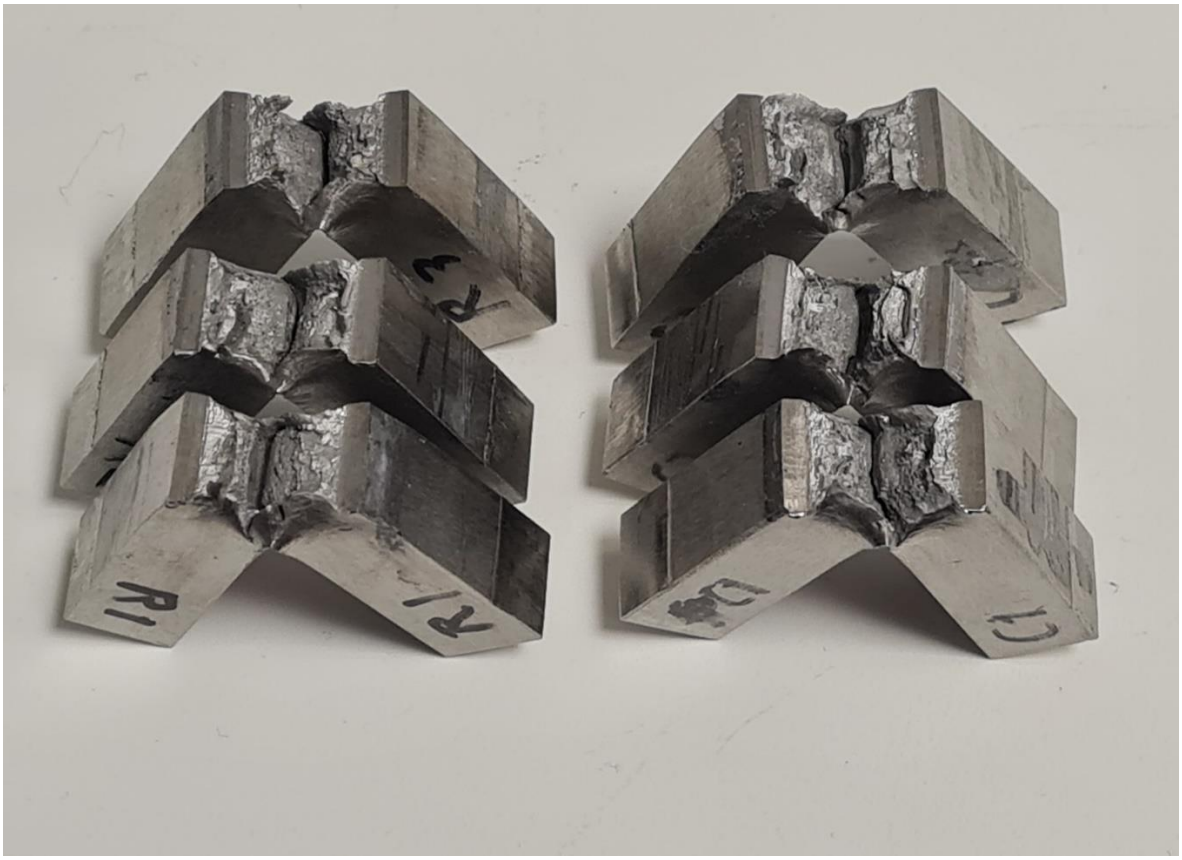

Figure 27 Picture of the Charpy tests after testing.

Figure 27 shows a picture of the Charpy test samples after testing. The ones to the left are the ones that were tested at room temperature and the ones to the right are the ones cooled down to $-46°C$. The samples are placed so that 1 is in the front and 3 is at the back.

All the fractures seem to have been ductile and the sample held together in a hinged form instead of splitting into two. It was not possible to further break the samples with one's bare hands. In addition, there isn't much difference between the ones to the right and the ones to the left.

Table 9 and Table 10 show the numeric results for the Charpy impact test. Measured in J. As the cross section for the samples outside of the notch is $10 \times 10\ mm$, which is equal to $1\ cm^2$. Thus, the values remain the same when converted to J/cm^2. Figure 28 shows the graphical representation of the average of the results with the error bars showing the highest and lowest value.

Table 9 Values recorded when doing the Charpy tests at room temperature.

Name of sample	Mechanical gauge in J	Digital reading in J
R1	313	310.3
R2	227	225.2
R3	302	298.7

Table 10 Results for Charpy test at -46 degrees Celsius

Name of sample	Mechanical gauge in J	Digital reading in J
C1	279	275.9
C2	309	305.9
C3	226	224

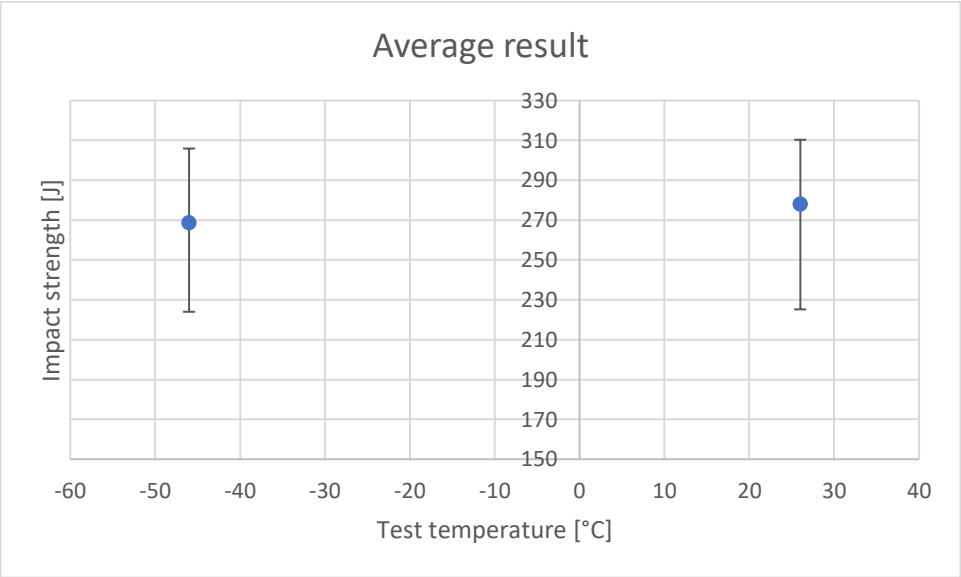

Figure 28 Graphic result of Charpy impact test

Figure 28 shows the results for the Charpy impact tests. The vertical axis shows the impact strength, while the horizontal axis shows the temperature in Celsius. The error bars point to the highest and the lowest impact strength values recorded. The average of each of the two sets of results are within the spread of values for the other set.

4.4 Tensile Test

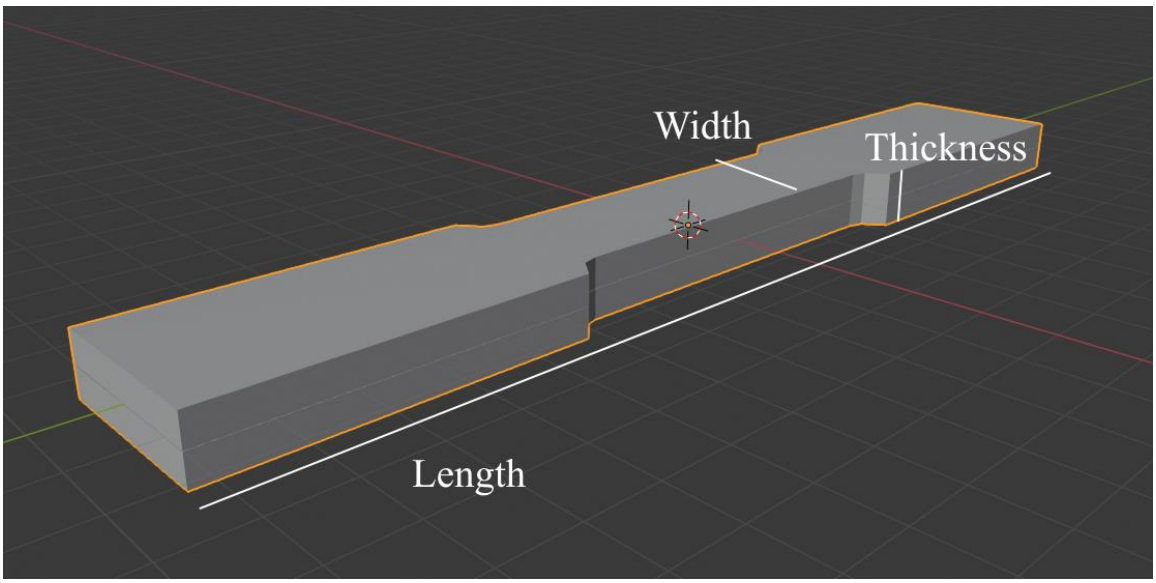

Figure 29 Illustration of where the dimensions are.

Table 11 Results for the tensile test

Specimen label	Tensile stress at Tensile strength [MPa]	Tensile stress at Break [MPa]	Thickness [mm]	Width [mm]	Specimen note
1	750.06	423.65	8.54	20.02	Necking and break at extensometer arm contact point occurred in all the specimens
2	751.40	428.58	9.14	20.02	
3	749.27	422.50	9.04	20.02	

Table 11 shows the tensile stress at ultimate tensile strength and at break in addition to the thickness and width of the cross section of the narrowed area. Figure 29 illustrates the areas of dimensional measurements.

Figure 30 shows the specimen after the tension test was done. The fusion zone looks like it has “expanded” in the area because the surrounding material have gotten a reduced thickness. The fracture appears to be ductile and happened some distance from the weld. The fusion zone also has some kind of pattern within its surface that emerged during the tensile test.

Figure 30 The tension specimens after the tests were done.

4.5 EBSD

The results from the EBSD appears to be upside down. The pictures were rotated 180° before being placed in this document. There are also some horizontal artifacts on the images.

IPF images for the areas are in the appendix in 8.4.

4.5.1 Weld Cap – Higher

The ferrite grains in Figure 31 stretches longer than the area chosen for this EBSD image. The area can be divided into three patterns: the upper pattern, the lower pattern and the pattern between them. In the upper and middle pattern there is mostly ferrite with a little bit of austenite, coloring these areas quite green. The lower pattern is redder and thus have more austenite.

In the upper pattern there can be found allotriomorphic austenite, intragranular austenite and some Widmanstätten austenite that seems to shoot out from the allotriomorphic austenite.

In the middle section there are some small needle structures of austenite and allotriomorphic austenite.

In the lower section there is allotriomorphic austenite, Widmanstätten austenite and a lot of intragranular austenite.

The fraction of austenite for the entire area is 0.265, while the fraction for ferrite is 0.735. However, it is clear that the upper section has less austenite than the lower section, so the fractions apply to the whole image all together and not the individual sections.

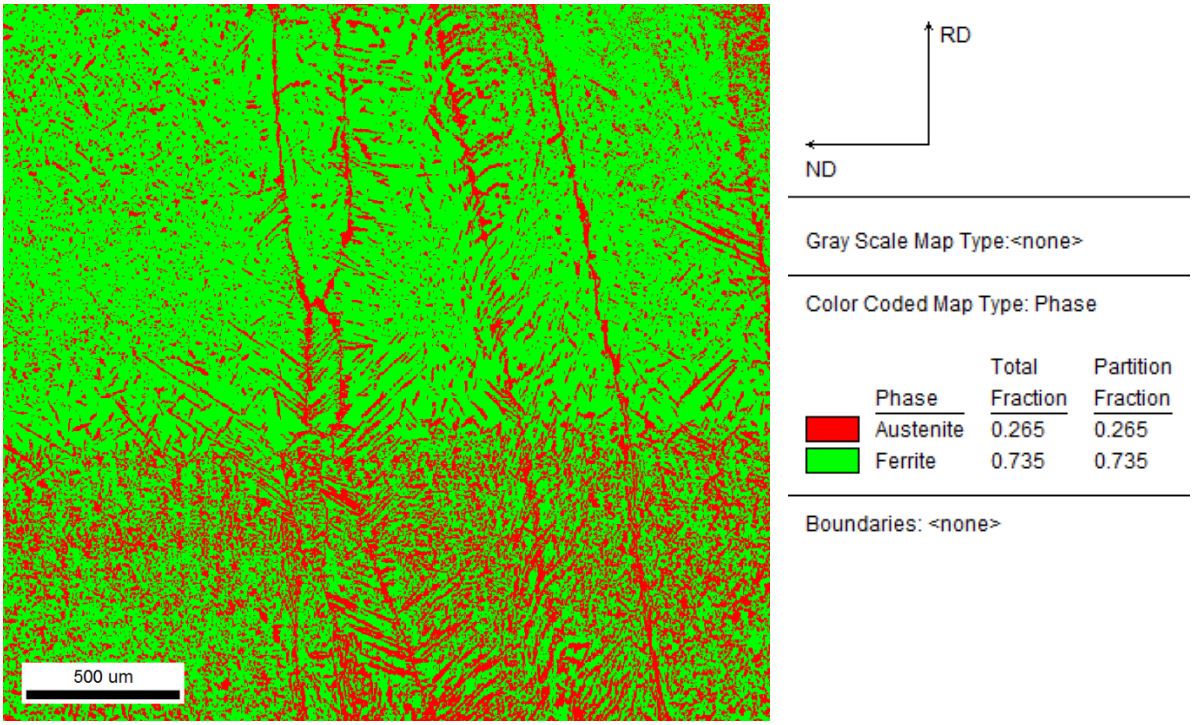

Figure 31 Phase map from the top of the weld.

Figure 32 shows the IPF map for the ferrite in the same area of Figure 31. On the left side there are some different ferrite grains with similar orientation without allotriomorphic austenite between them.

Figure 33 shows the grain size for the austenitic grains. The ferritic grains are all visually so large that the graph would not show an accurate result for them.

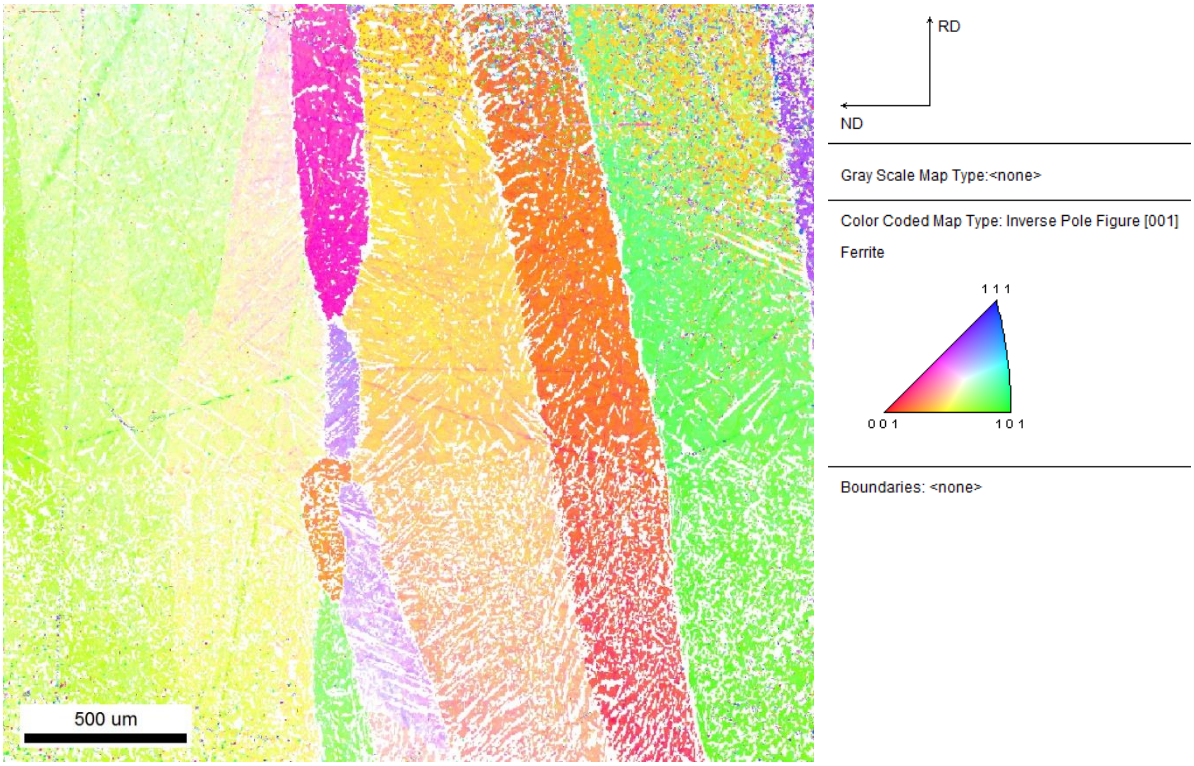

Figure 32 IPF map of the ferrite in the top of the weld.

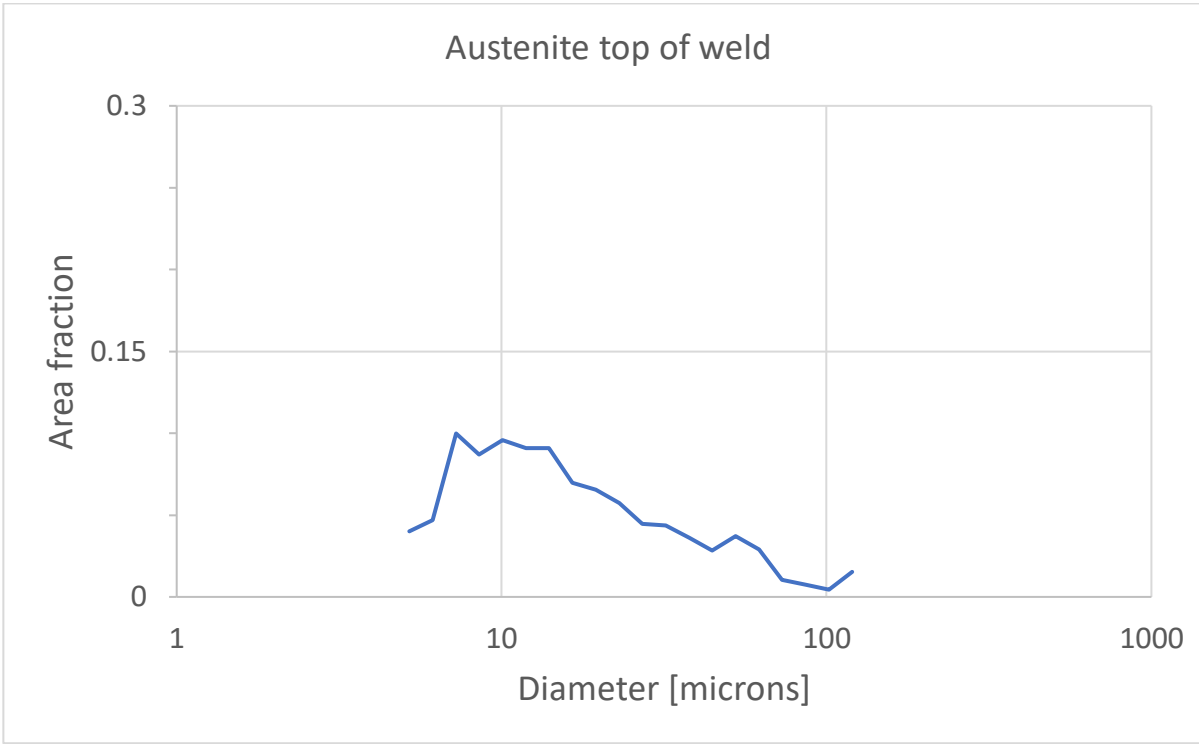

Figure 33 Graph showing the grain size distribution of austenite in the top of the weld.

4.5.2 Weld Cap - Lower

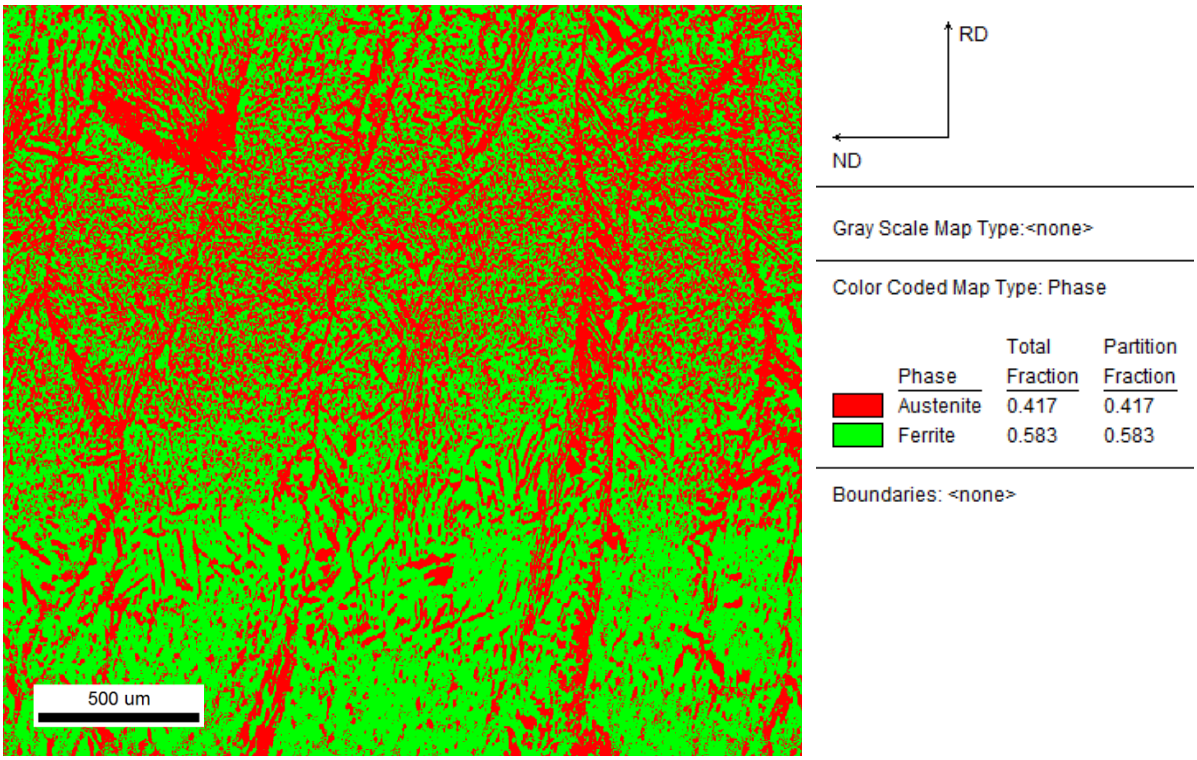

Figure 34 Phase map for weld cap.

Figure 34 shows the phase map for an area close to the weld cap, but lower than Figure 31. The ferrite grains are long and big. There is some allotriomorphic and Widmanstätten austenite formed on some of the ferrite grains.

In the upper part of the images there is a horizontal band where there is a lot of intragranular austenite, coloring the phase map red in this area. The cap of the weld has 41.7% austenite and 58.3% ferrite. This composition is not the same in the different part of the picture as some areas are redder than others.

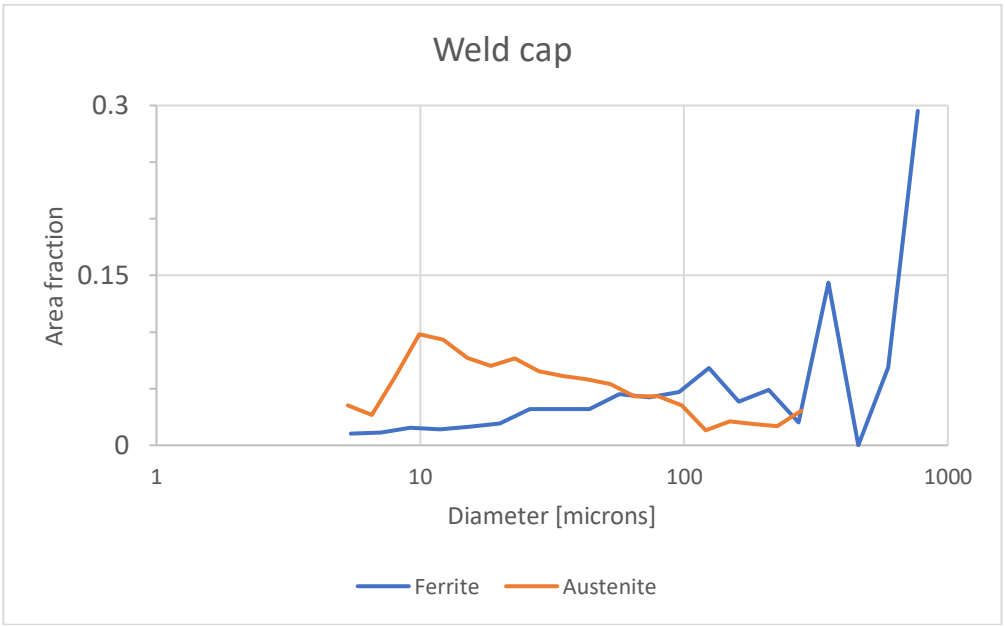

Figure 35 Grain size ferrite in weld cap.

Figure 35 shows the grain size for austenite and ferrite in area fraction per the diameter in micrometer. There are most austenite grains at about 10 microns and ferrite grains at 1000 microns or above. Figure 55 shows the length for at least one of the ferrite grains to have a length of above 2500 microns.

4.5.3 Center of Weld

Figure 36 shows the phase map in the center of the weld. The ferrite structure seems to be elongated, although based on the phase map, in the upper part of the image it is hard to see where the ferrite grain boundaries are.

The upper part of the image appears to be more red than the lower part of the image, thus it has more austenite. There are Widmanstätten austenite, intragranular austenite and austenite shapes harder to identify in the upper part of the image.

In the lower part of the image, the structure of austenite varies from grain to grain. Some grains have a lot of intragranular austenite, while others have more Widmanstätten austenite and others again have thick areas of austenite. The ferrite grains is separated by allotriomorphic austenite.

The area has 50.3% ferrite and 49.7% austenite, but as the upper area is redder and the lower area is greener, the composition varies for different part of the picture.

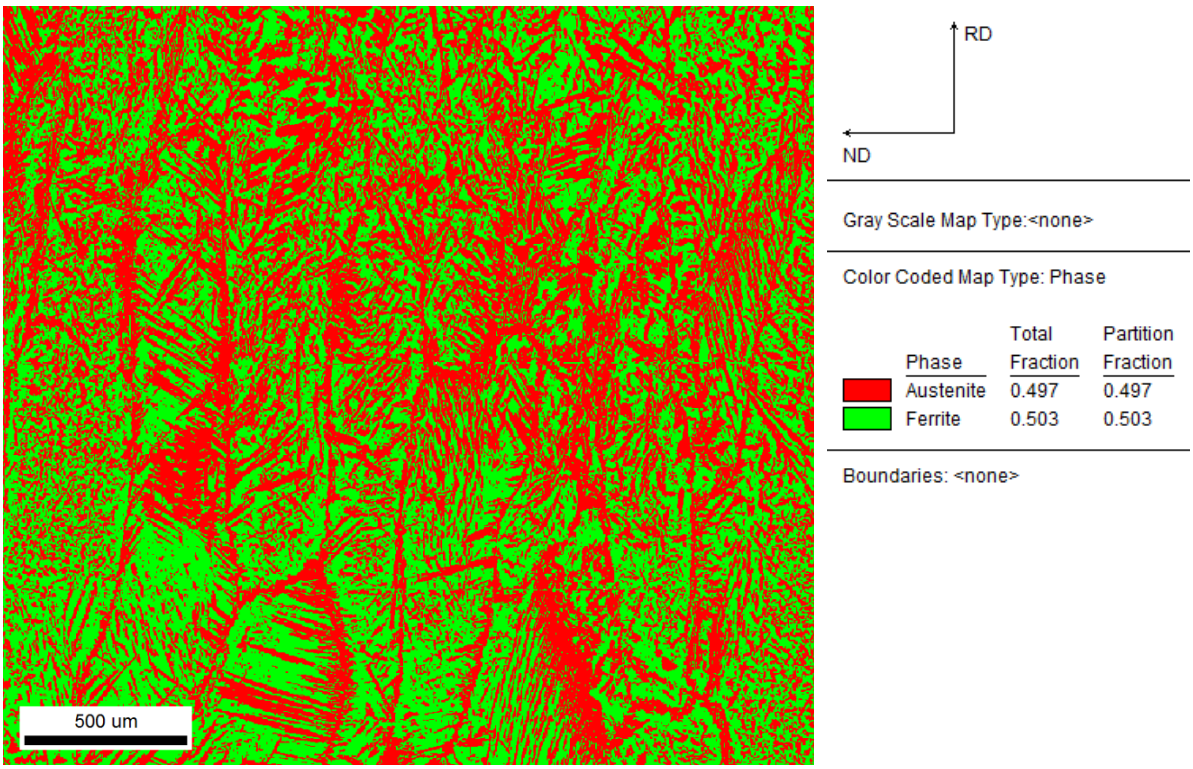

Figure 36 Phase map for an area in the center of the weld.

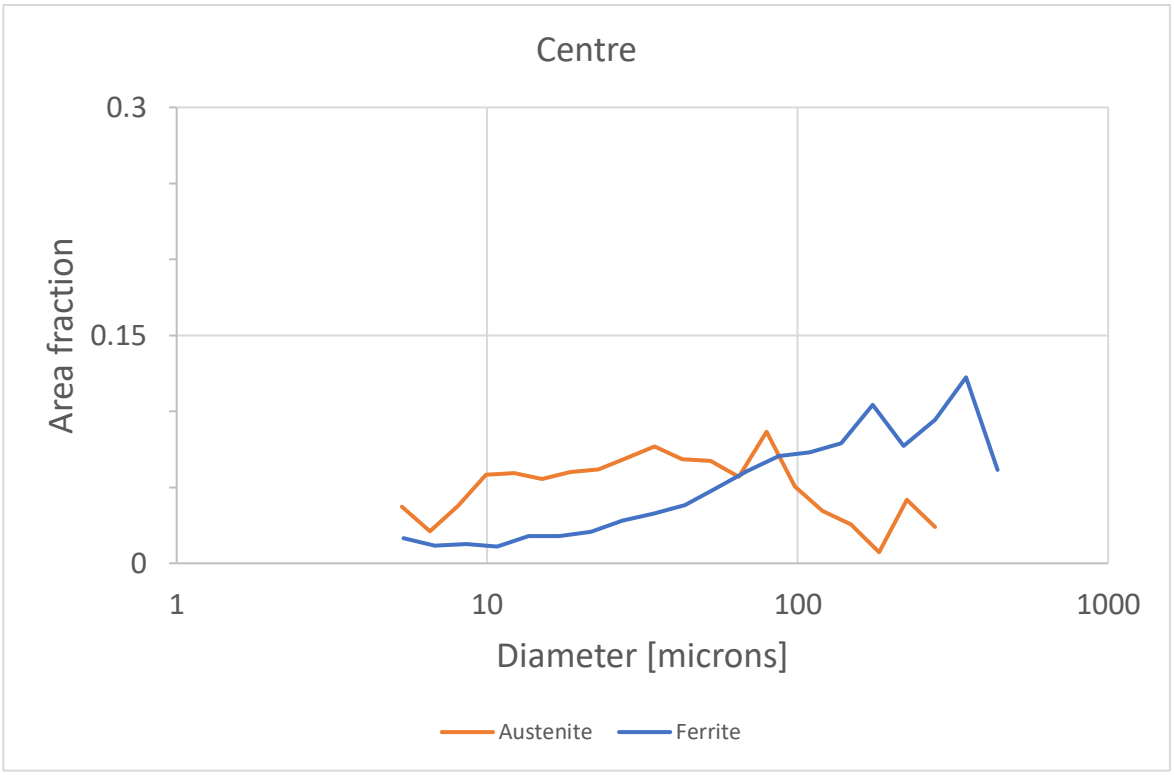

Figure 37 Graph over grain size for ferrite and austenite in the center of the weld.

4.5.4 HAZ and Surrounding Areas

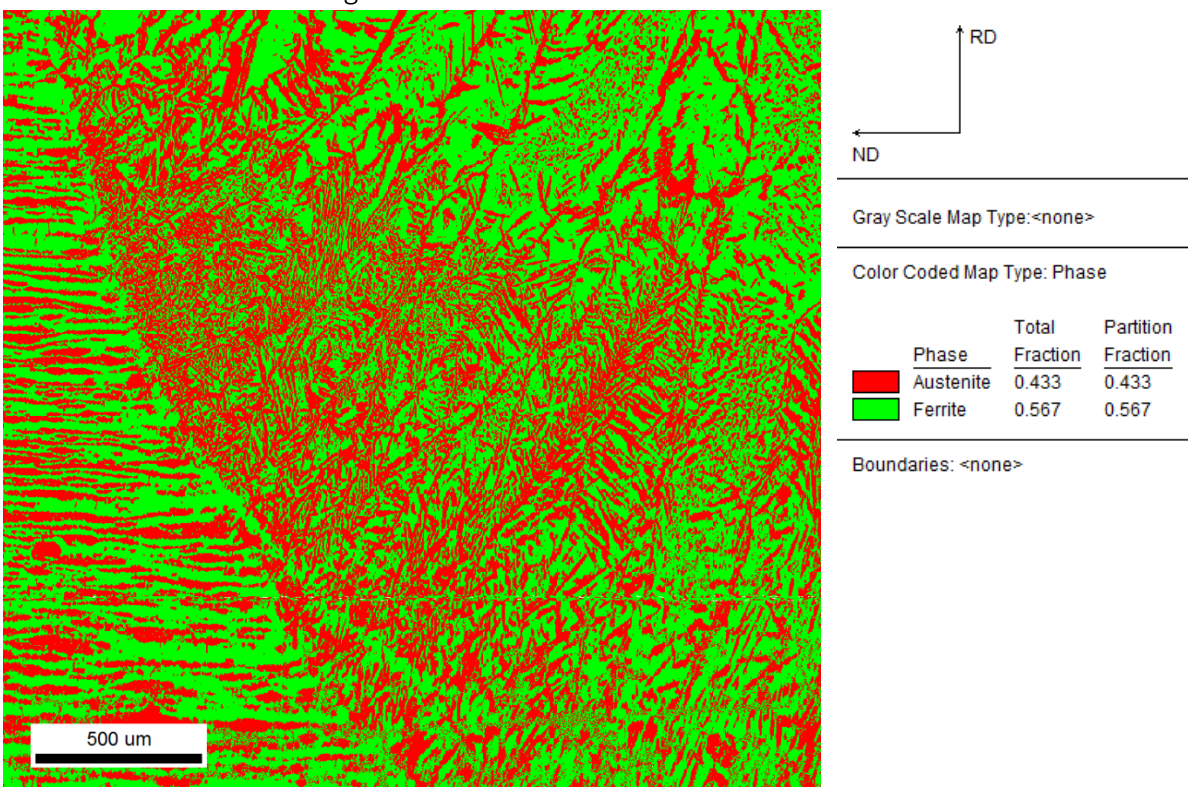

Figure 38 Phase map for the left HAZ.

Figure 38 shows that the depicted area of the boundary between the weld pool and the base material has a composition of 43.3% austenite and 56.3% ferrite, although the amount of

austenite and ferrite varies based on where one is in the image. This area covers a bit of the base material, the HAZ and the fusion zone, thus the data for the fractions isn't limited to just the HAZ.

The image can be seen as having multiple different sections. The lower left corner shows a structure that looks like base material. Getting closer to the weld, the structure looks mostly the same, but is more depleted of austenite. Then is a thin green line of ferrite left of the thicker and redder structure.

The section in the middle of the image is redder than the other sections of the image, thus has more austenite. There is allotriomorphic austenite and Widmanstätten austenite. But close to the fusion border, it is hard to identify the austenite structures.

The section in the upper right corner of the image is quite green, thus it has little austenite. The austenite here is mostly allotriomorphic austenite and intragranular austenite.

There is an area of higher austenite amount near the HAZ or at the HAZ than further into the weld pool.

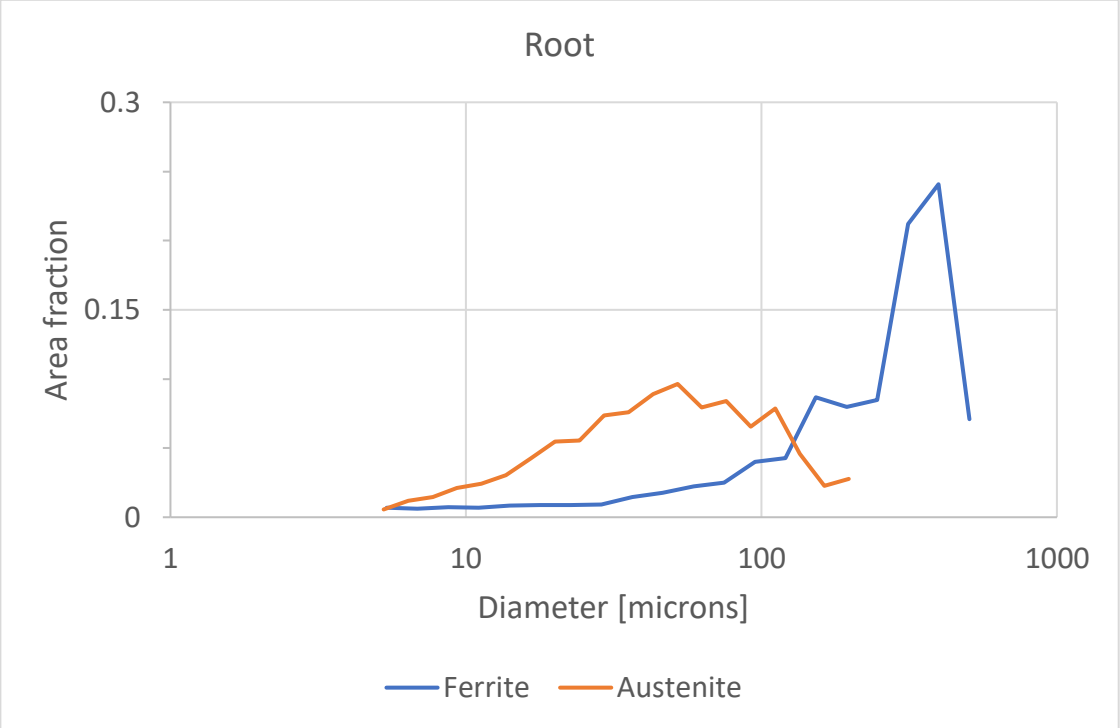

Figure 39 Grain size for ferrite for left HAZ.

Figure 39 shows the grain size for austenite and ferrite in area fraction per the diameter in micrometer. This area covers a bit of the base material, the HAZ and the fusion zone, thus the data isn't limited to just the HAZ. There are most austenite grains at about 40 microns and ferrite grains at about 300 microns.

4.5.5 Root Bead

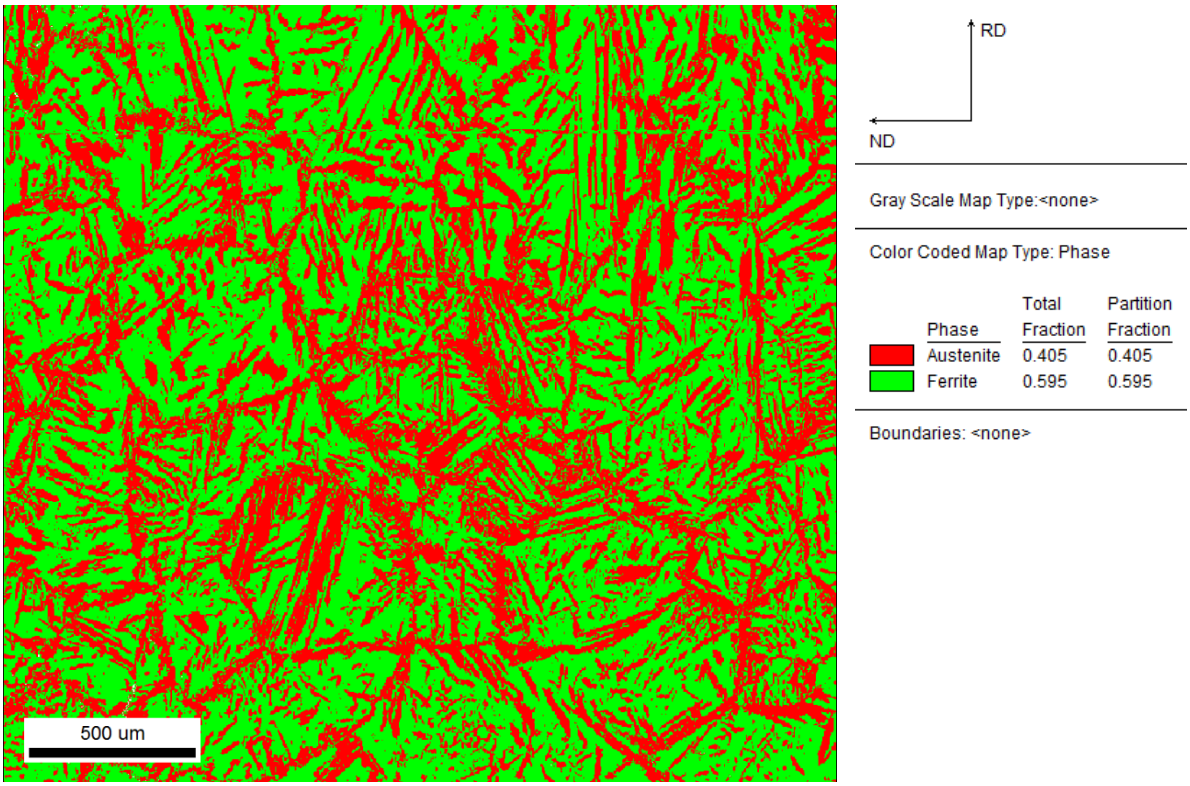

Figure 40 Phase map for the root bead.

The root of the weld has 40.5% austenite and 59.5% ferrite.

Figure 40 shows the phase map for an area in the root pass. Widmanstätten austenite, allotriomorphic austenite and intragranular austenite can be seen. The ferrite is rounder and together with the allotriomorphic austenite on the ferrite grain boundaries, the two structures can almost look a bit like the pattern on a turtle's shell.

There doesn't seem to be a red belt in this area as could be seen in Figure 31 and Figure 34.

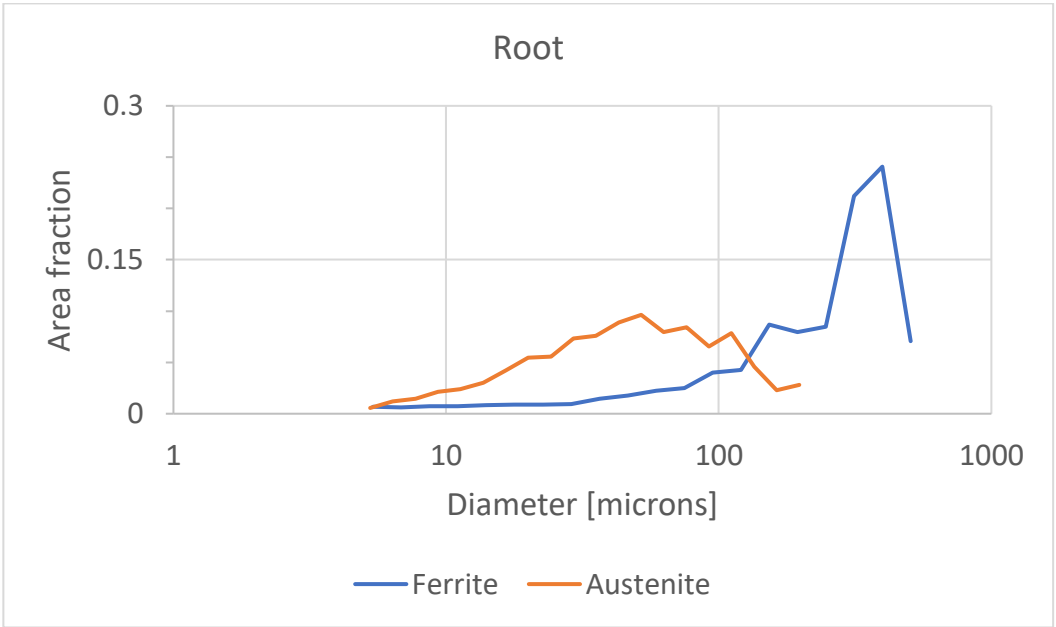

Figure 41 Grain size graph for austenite (orange) and ferrite (blue) in the root of the weld.

Figure 41 shows the grain size for austenite and ferrite in area fraction per the diameter in micrometer. There are most austenite grains at about 40 microns and ferrite grains at about 300 microns.

4.6 EDS

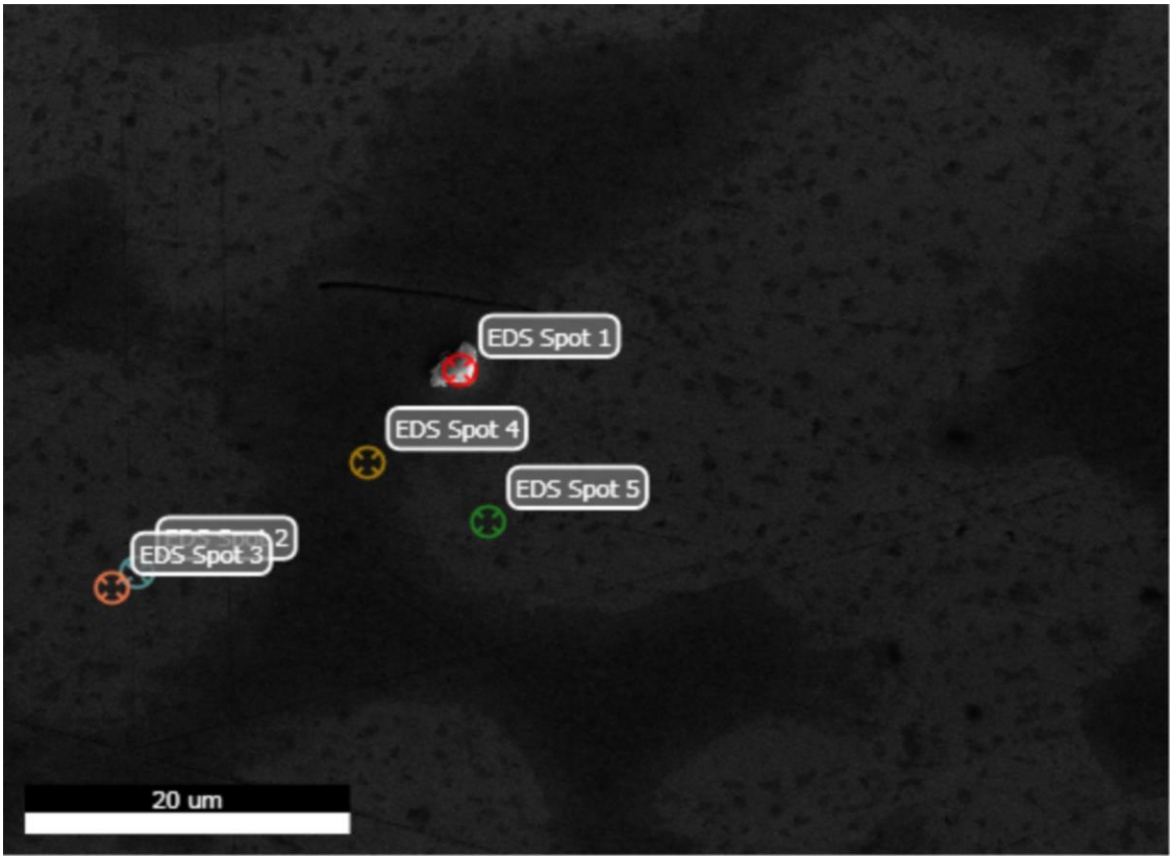

Figure 42 Areas where EDS was done.

Figure 42 shows the five spots where EDS was measured. The area is divided into grey and darker grey (almost black) areas. The grey areas have darker spots. Near the middle of the image there is a small particle that is only a couple of microns across that appears brighter than the rest of the area. The exact location of this image in the sample is unknown; it was chosen because of the particle in spot 1.

Spot 1 is located at the brighter particle and the elements that were found is shown in Table 12, which is based on the data in Figure 66 in 8.5 in appendix.

The rest of the spots got similar results to each other. The results can be seen in Table 13, which is a table based on the rest of the figures in 8.5.

Spot 1 has more carbon than the other spots, where in spot 1 it is one of the most prominent elements. In the other spots, there were only traces of carbon. In the other spots there were also traces of oxygen and silicon, which could not be seen in spot 1.

Table 12 Elements in spot 1:

Prominent	**Can be seen**
Carbon	Nickel
Iron	Molybdenum
Chromium	

Table 13 Elements in the rest of the spots:

Prominent	**Can be seen**
Iron	Molybdenum
Chromium	Nickel
	Carbon
	Oxygen
	Silicon

5 Discussion

5.1 Carbides

$M_{23}C_6$ forms above 0.02%C if the metal is within the right temperature for a long enough duration. The base material has 0.018% carbon content, which is beneath but close to 0.02% carbon. The filler material is at 0.02% carbon. This together should make it unlikely to find a carbide, but one was found during the EDS. The EDS doesn't say much about how many carbides there are in the material, but it shows that at least one particle can be found.

As carbides can make the material get a lower fracture toughness and the Charpy impact tests gave a good result, the number of them was likely not that great. This also makes sense per the chemical composition. It could be that there is just enough carbon in the material to form a small number of carbides or there can have been some contamination from the environment.

5.2 Tensile Test Behavior

During the tensile test, the fracture was in the base material. This means than the base material has a lower ultimate tensile strength than the HAZ and weld metal, as it didn't snap there. This also indicates that the ultimate tensile strength in the weld metal and HAZ was not found.

The weld metal appeared to grow as the test was performed and grew visible in the sample as the tension test was performed. The "growth" was an effect that the base material was elongated, and its cross section shrank. This indicates that the welded section experienced less strain than the rest of the sample, which could be due to the nitrides that were found. Standard AWS B4.0 did recommend to not measure other things than ultimate tensile test as the material wouldn't be uniform during yielding. The result from the tensile test does indeed show that in some way the material properties are different in the weld compared to in the base material.

As the base material experienced necking and general loss of cross section, the base material experienced higher true stress than the weld metal as it had a smaller cross section.

As tensile strength and hardness for metals are related, this behavior could mean that the hardness in this region is higher than in the base material. And indeed, the hardness test found higher values in the weld metal.

5.3 Charpy Impact Test

The Charpy impact test results were similar for room temperature and -46°C. This is similar to Figure 1, where the impact energy hardly changes between those two temperatures. The same graph, although the reading may be unprecise, shows that expected values are around 250 J. The results for the Charpy impact tests had a value at around 270-280 J. Figure 1 is for UNS S31803 that has been solution annealed. Assuming that this material can be seen as

having the same properties as the base material, the weld seems to have a better impact toughness than the base material.

The study that reported a result of 153 J for their welded section in welded AISI 2205 used different measurements for their Charpy impact tests. Their cross-sectional measurements (10 mm times 7.5 mm) gives a cross sectional area of 0.75 cm^2. This gives 204 J/cm^2, which is around 25 J/cm^2 less than the lowest results in 4.3. The chemical composition of their base material also has a carbon content of 0.027%. This could be enough to form some kinds of carbides that could make their samples more brittle.

It must be noted that there was a variability between the Charpy impact test results and the Charpy impact tests were hit at the root of the weld instead of the cap of the weld. The thickness of the samples in this thesis and the samples for Figure 1 are also slightly different: the samples in this thesis were 10 mm thick, where the samples that Figure 1 described were 12 mm thick.

It has to be noted that there was a large spread between the lower and higher values, as seen in Figure 28. This makes it hard to know the precise values of the material and thus makes it hard to draw conclusions. To get a more precise result, more Charpy impact tests should be done.

5.4 Hardness

The mean hardness for both the Side-view sample and the Bottom-view sample were higher than for the sample with only base material. The highest values, both for the Side-view sample and the Bottom-view sample were in the fusion zone. So, it does seem that the weld has made the material harder. All the mean results are higher than the one in the base material certificate 8.1.2.

That said, the higher values for the Side-view sample were in the lower half of the fusion zone. Much of the upper half of the fusion zone had values only slightly greater than the ones found in the base material (values in the range of 250 to 280 in the Side-view sample compared to 240 to 250 in the base material sample). The lower part of the weld in the Side-view sample had values between 270 and 320. The Bottom-view sample had values between 280 and 340 in the fusion zone.

What is interesting is that the microstructure in the root, center and top of the weld are different from each other. The root of the weld has a more isotropic structure with smaller ferrite grains than in the cap of the weld. In the cap of the weld the ferrite grains are elongated and there are some bands of austenite crossing of them.

As the upper parts of the weld has less Widmanstätten austenite, and Widmanstätten austenite is harder, this might explain why the material is harder near the bottom of the weld.

5.5 Precipitates

There were found chromium nitrides in the outskirts of the weld or in the transition from weld metal to base metal. This should then lower the material's resistance to corrosion by depleting the material around the nitrides of chromium. This thesis did not do tests on corrosion.

Chromium nitrides can also lower the impact toughness, which is interesting considering how well the Charpy tests did. That said, the nitrides were found in the outskirts of the weld or in the HAZ and the Charpy tests were attempted to be done as in middle of the weld as possible. It could be that the area that was tested by the Charpy test was relatively unaffected by nitrides.

One particle that was likely a carbide was also found. Carbides can be the starting point for different types of corrosion and is thus unwanted. It is unclear how many carbides were found in the material.

5.6 Phase Distribution

The amount of austenite varied from place to place. Although the EBSD phase map indicated that there was around 40 to 50% austenite in several areas, there were in some of these areas different regions where it was clear that some areas had more austenite than others. But averaging out the results does give a value between 40 and 50%.

The different places in the weld also had different patterns of austenite and ferrite. In the root the ferrite grains were smaller and rounder, while in the weld cap, the ferrite grains were larger and had a more elongated shape. The areas in the cap, between the bands of austenite, could be areas where there weren't enough ferrite-ferrite grain boundaries to let austenite nucleate as the material cooled down.

There were found some austenite depleted zones with bands of austenite rich zones between. One thought is that the bands of austenite are HAZ zones between the passes as the material here has a longer time in the right temperatures to form the austenitic structures. Another thought could be that the austenite depleted zone between the bands of austenite could be the HAZ as nickel-based alloys can draw nitrogen from the HAZ to the fusion zone. But the filler isn't very different from the base material, and of nickel content it was 8.6% nickel instead of 5.55% nickel. That doesn't seem to be a nickel-based alloy. It can also be noted that this pattern of bands of austenite between areas of depleted austenite is seen in the upper part of the weld, nearing the weld cap.

As austenite has a high fracture toughness, it makes sense that the Charpy impact test had good results, as the amount austenite in unwelded S31803 should be about 50%. What is interesting is that austenite is also ductile. The Charpy tests did show ductile breaks, but for the tensile tests, the base material showed more ductility than the weld in that the weld appeared to "grow". But it can be that the base material was only slightly more ductile and that this slight difference made the base material give way for the weld material.

Ferrite also gives a higher tensile strength than austenite. If the level of austenite in the weld is lower than the level of austenite in the base material, it does explain why the weld material had a higher tensile strength.

6 Conclusion

This thesis examined the microstructure and the mechanical properties of a weld in a pipe made from S31803 Duplex Stainless Steel.

The mechanical tests that were done were Vickers hardness, tensile test and Charpy impact test. The hardness test showed root of the weld was harder than the rest of the weld, which again was harder than the base material. The weld material had a higher tensile strength than the base material. The Charpy impact test gave results consistent with the base material. All the mechanical tests showed good results.

The microstructural observations were done by optical microscope, EBSD and EDS.

There were found some chromium nitrides and carbides in the material. Although corrosion testing wasn't done, the theory states that this can give a worsened resistance against corrosion.

There were different structures in the root of the weld than in the cap of the weld. In the root the structures varied less based on direction and location. Nearer the cap there were bands of austenite transverse to long ferrite grains, where the metal outside of the bands has a lower amount of austenite.

6.1 Further Work

For future studies of the material different things can be examined.

Fatigue and fractures can cause accidents after the material has been in operation for some time. Fatigue testing of the weld could be done to see how it behaves over time.

Precipitation can affect how well stainless steel can resist corrosion. It could thus be useful to do corrosion tests on the weld and HAZ and see how they behave compared to the base material.

The Charpy impact tests were done only at the root of the weld. It could be useful to also having done it in the base material to see how the values compared. It could also be interesting to see if the Charpy impact tests gives the same values if it hits the cap of the weld.

The Charpy impact test results spread quite a bit from lowest to highest. To get a more precise result, more test could be done to see what values were outliers that skewed the results.

It could also be interesting to study the fracture surface for the Charpy impact test specimens to examine how the microstructure looks after the test.

There weren't done any hardness tests in the top of the weld cap or in the bottom-most part of the weld root. To get a fuller picture of the relationship between microstructure and hardness, hardness tests could be done in these areas.

7 References

[1] "What is Duplex Steel?," *Metal Supermarkets*, Apr. 13, 2022. https://www.metalsupermarkets.com/what-is-duplex-steel/ (accessed Mar. 09, 2023).

[2] M. F. McGuire, *Stainless Steels for Design Engineers*. ASM International, 2008. doi: 10.31399/asm.tb.ssde.9781627082860.

[3] International Molybdenum Association, *Practical Guidelines for the Fabrication of Duplex Stainless Steels*, Third. London, UK: International Molybdenum Association (IMOA), 2014.

[4] J. C. de Lacerda, L. C. Cândido, and L. B. Godefroid, "Effect of volume fraction of phases and precipitates on the mechanical behavior of UNS S31803 duplex stainless steel," *International Journal of Fatigue*, vol. 74, pp. 81–87, May 2015, doi: 10.1016/j.ijfatigue.2014.12.015.

[5] R. Honeycombe and H. Bhadeshia, *STEELS Microstructure and Properties*, Fourth edition. BH Elsevier, 2017.

[6] "UNS S31803 Stainless Steel :: MakeItFrom.com." https://www.makeitfrom.com/material-properties/UNS-S31803-Stainless-Steel (accessed Jun. 10, 2023).

[7] R. N. Gunn, Duplex Stainless Steels '91, and Duplex Stainless Steels '94, *Duplex stainless steels: microstructure, properties and applications*. Cambridge: Abington, 1997.

[8] Dr. J. Fritz, *Practical guide to using duplex stainless steels*, Second. Nickel Institute, 2020.

[9] S. Kou, *Welding Metallurgy*, Third Edition. Wiley, 2021.

[10] "What is Fusion Welding?" https://www.twi-global.com/technical-knowledge/faqs/what-is-fusion-welding.aspx (accessed Jul. 01, 2023).

[11] A. Vinoth Jebaraj and L. Ajaykumar, "Influence of Microstructural Changes on Impact Toughness of Weldment and Base Metal of Duplex Stainless Steel AISI 2205 for Low Temperature Applications," *Procedia Engineering*, vol. 64, pp. 456–466, Jan. 2013, doi: 10.1016/j.proeng.2013.09.119.

[12] J. C. Lippold, *Welding metallurgy and weldability*. 2014.

[13] T. Tóth, S. Krasnorutskyi, J. Hensel, and K. Dilger, "Electron beam welding of 2205 duplex stainless steel using pre-placed nickel-based filler material," *International Journal of Pressure Vessels and Piping*, vol. 191, p. 104354, Jun. 2021, doi: 10.1016/j.ijpvp.2021.104354.

[14] A. J. W. Menezes, H. Abreu, S. Kundu, H. K. D. H. Bhadeshia, and P. M. Kelly, "Crystallography of Widmanstätten austenite in duplex stainless steel weld metal," *Science and Technology of Welding and Joining*, vol. 14, no. 1, pp. 4–10, Jan. 2009, doi: 10.1179/136217108X341166.

[15] N. Sayyar, V. Hansen, W. M. Tucho, and M. W. Minde, "Directed laser deposition of super duplex stainless steel: Microstructure, texture evolution, and mechanical properties," *Heliyon*, vol. 9, no. 4, Apr. 2023, doi: 10.1016/j.heliyon.2023.e15144.

[16] W. D. Callister and D. G. Rethwisch, *Material Science and Engineering*, 9th edition. Asia: Wiley, 2015.

[17] T. H. Chen and J. R. Yang, "Microstructural characterization of simulated heat affected zone in a nitrogen-containing 2205 duplex stainless steel," *Materials Science and Engineering: A*, vol. 338, no. 1, pp. 166–181, Dec. 2002, doi: 10.1016/S0921-5093(02)00065-5.

[18] A. Vinoth Jebaraj, L. Ajaykumar, C. R. Deepak, and K. V. V. Aditya, "Weldability, machinability and surfacing of commercial duplex stainless steel AISI2205 for marine applications – A recent review," *Journal of Advanced Research*, vol. 8, no. 3, pp. 183–199, May 2017, doi: 10.1016/j.jare.2017.01.002.

[19] E. Westin, "Microstructure and properties of welds in the lean duplex stainless steel LDX 2101," Jan. 2010.

[20] B. Deng, Z. Wang, Y. Jiang, T. Sun, J. Xu, and J. Li, "Effect of thermal cycles on the corrosion and mechanical properties of UNS S31803 duplex stainless steel," *Corrosion Science*, vol. 51, no. 12, pp. 2969–2975, Dec. 2009, doi: 10.1016/j.corsci.2009.08.015.

[21] S. S. M. Tavares, V. F. Terra, J. M. Pardal, and M. P. C. Fonseca, "Influence of the microstructure on the toughness of a duplex stainless steel UNS S31803," *J Mater Sci*, vol. 40, no. 1, pp. 145–154, Jan. 2005, doi: 10.1007/s10853-005-5700-7.

[22] “Stainless Steel - General Information - Alloying Elements in Stainless Steel.” https://www.aalco.co.uk/datasheets/Stainless-Steel_Alloying-Elements-in-Stainless-Steel_98.ashx (accessed May 07, 2023).
[23] K. Trethewey and J. Chamberlain, *Corrosion for Science and Engineering*, Second edition. Pearson Education, 1998.
[24] “Vickers hardness | mineralogy | Britannica.” https://www.britannica.com/science/Vickers-hardness (accessed Jan. 28, 2023).
[25] V. S. Moura, L. D. Lima, J. M. Pardal, A. Y. Kina, R. R. A. Corte, and S. S. M. Tavares, “Influence of microstructure on the corrosion resistance of the duplex stainless steel UNS S31803,” *Materials Characterization*, vol. 59, no. 8, pp. 1127–1132, Aug. 2008, doi: 10.1016/j.matchar.2007.09.002.
[26] “Vickers Hardness Testing.” https://www.hardnesstesters.com/test-types/vickers-hardness-testing (accessed Jun. 10, 2023).
[27] R. Magnabosco and C. K. Sutto, “MICROHARDNESS OF UNS S31803 (SAF 2205) DUPLEX STAINLESS STEEL AFTER ISOTHERMAL AGING BETWEEN 700°C AND 900°C,” 2003. Accessed: Jun. 10, 2023. [Online]. Available: https://www.semanticscholar.org/paper/MICROHARDNESS-OF-UNS-S31803-(SAF-2205)-DUPLEX-STEEL-Magnabosco-Sutto/d3edae598542ad6b1d5116ae7315454a090a5a5c
[28] “Steel Hardness Conversion Table.” https://www.steelexpress.co.uk/steel-hardness-conversion.html (accessed Jun. 10, 2023).
[29] A. C. on B. C. on M. T. of Welds, “Tension Tests,” in *Standard Methods for Mechanical Testing of Welds - AWS B4.0:2016*, 2016, pp. 1–1.
[30] “Metallographic hot mounting insight | Struers.com.” https://www.struers.com/en/Knowledge/Mounting/Hot-mounting# (accessed Apr. 26, 2023).
[31] “Vickers hardness testing: ISO 6507, ASTM E384,” *Vickers hardness testing: ISO 6507, ASTM E384*. https://www.zwickroell.com/industries/metals/metals-standards/vickers-test-iso-6507/ (accessed Jan. 28, 2023).

8 Appendices

8.1 Documents

8.1.1 WPS

ROSENBERG

WELDING PROCEDURE SPECIFICATION (WPS)

WPS No.: P410-05
Ref.:
Date: 2022-09-19 Rev: 02

Prod. by:	Rosenberg WorleyParsons	Client:	Subsea 7	Ref. stand:	DNVGL-ST-F101 (2017)
Project:	7330 FROSK & 7333 KEG	Ref. spec.:		Exam. body:	
Location:	Stavanger	Ref. WPQR:	RP410H05.06.11 Pro.Test P410-05		

	1	2	3
Welding process	141		
Shielding gas type	ARGON 4.6 I1		
Weaving (yes/no)	YES max: 12 mm	max: mm	max: mm

Purging gas type	ARGON 4.6 I1 45 l/min
Welding positions	All -PG
Joint type	BUTTWELD
Joint preparation	MACHIN./GRIND
Cleaning method	GRIND / BRUSH
Backing	NO
Single/Double	SINGLE
Back gouging	NO
Flux designation	NA
Flux handling	NA
Tungsten electrode	2,4 - 2% Thorium mm
Torch angle	60-90 °
Stand off distance	2-15 mm
Nozzle diameter(s)	15-20mm mm
Tack welding proc.	COL750-R Rev: 4

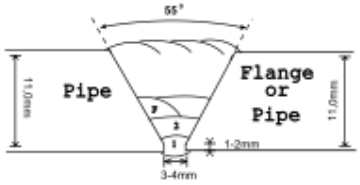

Filler Metal Batch
UTP A 6808 Mo: Batch 106466

Identification of parent metal I: CE max: C max: PCM max: II: CE max: C max: PCM max:

Part	Name/Grade	Standard	Group	Delivery cond.	Thickness range [mm]	Diameter range [mm]
I	DNV SMLS 22Cr	DNV-OS-F101	10.1	Solution Annealed	11,00 - 11,00	146,30 - 146,30
II	F51, 22Cr	ASTM A182	10.1	Solution Annealed	11,00 - 11,00	146,30 - 146,30

Identification of filler metal

Index	Trade name	Classification	Group	Filler handling
1	UTP A 6808 Mo	EN ISO 14343-A W 22 9 3 N L	FM5	COZ767-R
2				
3				

Welding Parameters Equipment: Kemppi

Pass no.	Index	Dia. [mm]	Welding process	Wire feed speed [m/min]	Current [A]	Voltage [V]	Current / Polarity	Welding speed [mm/min]	Run Out Length [mm]	Gas [l/min]	Heat input [kJ/mm]
1	1	2,40	141	-	100 - 113	11,0 - 12,0	DC-	36 - 40		20	1,7 - 2,3
2	1	2,40	141	-	188 - 198	12,0 - 13,0	DC-	102 - 149		20	0,9 - 1,4
Fill	1	2,40	141	-	195 - 220	12,5 - 13,5	DC-	92 - 152		20	1,0 - 1,9
CAP	1	2,40	141	-	160 - 205	12,0 - 14,0	DC-	105 - 120		20	1,0 - 1,6
				-	-	-		-			-
				-	-	-		-			-
				-	-	-		-			-
				-	-	-		-			-
				-	-	-		-			-

Heat treatment Method:

Preheat min: 13 °C Interpass temp. max: 150 °C Heat treatment proc.: Temp. control: Digital
PWHT min: °C max: °C Soaking: min/mm min Heating rate: °C/h Cooling rate: °C/h

Remarks:
- Max O2 in purge, 170ppm

- Diameter refers to ID, internal diameter

Additional info enclosed (Yes/No): NO

Date/Signature: 2022-09-19 AEG
Andreas Gilje

Approved: 2022-09-19 AEG
Andreas Gilje

Index no. 1001423779 Page 1 of 1 Produced by WeldEye®

8.1.2 Base Material Certificate

CERTIFICADO DE INSPECCIÓN
EN 10204:2004 / 3.2

Number: 732559 Page: 1 / 4	Rev: 00
Created on: Date: 27.04.2022	Modified on: 27.04.2022

TTI - TUBACEX TUBOS INOXIDABLES
Registro Mercantil de Alava, Tomo 587, Folio 189, Hoja VI 2885 - N.I.F. A-01140227
Tres cruces, 8
01400 Llodio (Alava)
SPAIN
TL: +34 946719300
FAX: +34 946725062
E-MAIL: qualitytti@tubacex.es

DESCRIPCIÓN DEL CLIENTE

SOLICITANTE	DESTINAT. MCÍA.
TSS NORWAY AS ESPEHAUGEN 45 5258 BERGEN NORWAY	TSS NORWAY AS ESPEHAUGEN 45 5258 BERGEN NORWAY

PEDIDO CLIENTE: 503855
PEDIDO VENTAS: 372492

MATERIAL:SEAML. STAINL. STEEL TUBES/PIPES
HEAT-TREATED, PICKLED, PASSIVATED AS PER ASTM A380
GRADE: 22Cr, S31803, DNV 22Cr,
STANDARD: ASTM A790/A790M-20
NORSOK M650 Ed.4 QTR No.1
NORSOK M630:2020 MDS D41 REV.6
OFFSHORE STANDARD DNVGL-ST-F101 OCT. 2017 Amd DEC 2017
OD: + 1,26 MM- 1,26 MM,WT: + 14,99 %- 12,49 %,OVALITY MAX. 2,52 MM,STRAIGHTNESS (MM/M) MAX. 5,00 MM,
RANDOM LENGTHS 6.000/11.179 MM
PLAIN ENDS,
DIMENSIONS: 168,28 X 10,97 MM - 6" SCH 80S
HOT FINISHED
.
ITP: 21-AL-1201-IA-01

Pos Ped.	Pos Clnt	Nº Entrega	Nº lote	Colada	Piezas	Peso	Long. Tot	Long. Un
20	PROJECT: FROSK		P2201256	58700	6	1.912 KG	43,53 M	6000-11179 MM
20	PROJECT: FROSK		P2200997	58701	2	594 KG	13,50 M	6000-11179 MM
20	PROJECT: FROSK		P2201312	58628	14	4.398 KG	100,52 M	6000-11179 MM
20	PROJECT: FROSK		P2201000	58629	6	2.034 KG	46,35 M	6000-11179 MM
20	PROJECT: FROSK		P2201256	58700	4	1.255 KG	28,65 M	6000-11179 MM
20	PROJECT: FROSK		P2201312	58628	7	2.264 KG	51,88 M	6000-11179 MM
20	PROJECT: FROSK		P2201256	58700	1	309 KG	7,11 M	6000-11179 MM
20	PROJECT: FROSK		P2201004	58628	6	1.871 KG	42,75 M	6000-11179 MM
20	PROJECT: FROSK		P2201004	58628	1	291 KG	6,71 M	6000-11179 MM

DATOS MATERIAL

Heat Nr:	Supplier	Method
58628	ACERALAVA (SPAIN)	Electric furnace+AOD
58629	ACERALAVA (SPAIN)	Electric furnace+AOD
58700	ACERALAVA (SPAIN)	Electric furnace+AOD

AENOR Empresa Registrada UNE-EN ISO 9001
AENOR Gestión Ambiental UNE-EN ISO 14001

Luis A. San Emeterio
FTR Inspector obo Subsea7
27 April 202
REVIEWED

TUBACEX TUBOS INOXIDABLES S.A.U.
INGENIERIA DE CALIDAD
Iñigo Arriola Alcibar

TTI
TUBACEX
GROUP

CERTIFICADO DE INSPECCIÓN EN 10204:2004 / 3.2

Number: 732559 Page: 2 / 4	Rev: 00
Created on: Date: 27.04.2022	Modified on: 27.04.2022

DATOS MATERIAL

Heat Nr:	Supplier	Method
58701	ACERALAVA (SPAIN)	Electric furnace+AOD

COMPOSICIÓN QUÍMICA (%) *L: Ladle C:Products

*	Heat	Seq	C	Mn	Si	P	S	Ni	Cr	Mo	N	Pren
L	58628	1	0,013	1,19	0,290	0,028	0,0007	5,45	22,60	3,19	0,1885	36,1430
L	58629	1	0,012	1,05	0,320	0,029	0,0005	5,42	22,82	3,10	0,1873	36,0468
L	58700	1	0,018	1,04	0,270	0,028	0,0005	5,55	22,55	3,18	0,1669	35,7144
L	58701	1	0,013	1,03	0,290	0,029	0,0004	5,35	22,60	3,12	0,1670	35,5680
C	58628	4	0,013	1,18	0,290	0,028	0,0007	5,40	22,55	3,20	0,1885	36,1260
C	58628	5	0,013	1,19	0,310	0,027	0,0007	5,46	22,60	3,19	0,1885	36,1430
C	58629	8	0,012	1,05	0,320	0,029	0,0005	5,45	22,70	3,19	0,1875	36,2270
C	58629	9	0,012	1,03	0,320	0,029	0,0005	5,38	22,87	3,15	0,1873	36,2618
C	58700	8	0,018	1,02	0,270	0,027	0,0005	5,55	22,45	3,17	0,1669	35,5814
C	58700	9	0,018	1,03	0,270	0,027	0,0005	5,55	22,50	3,15	0,1670	35,5670
C	58701	1	0,013	1,00	0,290	0,030	0,0004	5,39	22,56	3,12	0,1670	35,5280
C	58701	8	0,013	1,02	0,290	0,028	0,0004	5,40	22,55	3,11	0,1670	35,4850

TRATAMIENTO TÉRMICO

SOLUTION ANNEALED AT 1040 °C , Direct water quenched

TEST DE TENSIÓN

Lot No.	Sample	T	Rp0.2	Rp0.5	Rp1.0	Rm	A2"	A5	Type	Spc.Type	Spc.Dim	YS0.5/TS
		°C	MPa	MPa	MPa	MPa	%	%			mm	
P2200997	1	20	649	642	710	777	36	34	L	S	20,07	0,83
P2201312	1	20	541	545	604	750	49	46	L	S	20,05	0,72
P2201000	1	20	510	539	586	728	42	38	L	S	20,09	0,74
P2201256	1	20	477	503	551	702	36	34	L	S	20,05	0,72
P2201004	1	20	473	487	570	722	41	37	L	S	19,97	0,68

TEST DE DUREZA

Lot No.	Sample	HV1	HV2
P2200997	1	228	223
P2201312	1	223	228
P2201000	1	233	228
P2201256	1	223	218
P2201004	1	223	223

TEST DE IMPACTO

Lot No.	Sample	T	Wspec	Ecv 1	Ecv 2	Ecv 3	Ecv AVG	Type	Le1	Le2	Le3	Shear 1	Shear 2	Shear 3
		°C	mm	J	J	J	J		mm	mm	mm	%	%	%
P2200997	1	-46	5,00	90	77	91	86	T	1,70	1,60	1,70	100	100	100
P2201312	1	-46	7,50	165	170	164	166	T	1,80	1,87	1,89	70	70	70
P2201000	1	-46	5,00	95	86	82	88	T	1,80	1,60	1,60	100	100	100
P2201256	1	-46	7,50	184	172	187	181	T	2,20	2,10	2,20	100	100	100
P2201004	1	-46	7,50	148	145	130	141	T	2,00	1,90	1,70	100	100	100

AENOR ER Empresa Registrada UNE-EN ISO 9001

AENOR Gestión Ambiental UNE-EN ISO 14001

Luis A. San Emeterio
FTR Inspector obo Subsea7
27 April 202
REVIEWED

TUBACEX TUBOS INOXIDABLES S.A.U.
INGENIERIA DE CALIDAD

Iñigo Arriola Alcibar

TTI TUBACEX GROUP

CERTIFICADO DE INSPECCIÓN
EN 10204:2004 / 3.2

Number: 732559 Page: 3 / 4	Rev: 00
Created on: Date: 27.04.2022	Modified on: 27.04.2022

Corrosión ASTM G48 práctica A

Lot No.	Sample	T	Pits-20x	W.loss	time
		°C		g/m2	Horas
P2200997	1	25	N	0,0000	24,0
P2201312	1	25	N	0,1211	24,0
P2201000	1	25	N	0,1184	24,0
P2201256	1	25	N	0,0000	24,0
P2201004	1	25	N	0,0000	24,0

Contenido de Ferrita según ASTM E562

Lot No.	Sample	%Fer	Dev.Ferr	ACCURACY
		%	%	%
P2200997	1	48,54	2,25	2,95
P2201312	1	44,14	2,32	3,34
P2201000	1	47,67	2,01	2,67
P2201256	1	47,26	1,50	2,00
P2201004	1	44,80	1,87	2,65

ESPACIADO DE AUSTENITA

Lot No.	Sample	MICRAS
		µm
P2200997	1	7
P2201312	1	6
P2201000	1	6
P2201256	1	5
P2201004	1	6

METALURGICAL TESTS

ETCH STRUCTURE ACC. DNVGL-ST-F101 App.B. MATERIAL FREE FROM INTERMETALLIC PHASES AND PRECIPITATES. UNIFORM STRUCTURE ACROSS FULL WALL THICKNESS

NON-DESTRUCTIVE TESTS

100% ULTRASONIC TEST ACC. TO ISO 10893-10 LONGITUDINAL AND TRANSVERSE LEVEL U2;Laminar Imperfections DNVGL-ST-F101 Table D12,continuous wall thickness verification ISO 10893-12: satisfactory

POSITIVE MATERIAL IDENTIFICATION TEST ON EACH TUBE/PIPE BY "X-RAY-FLUORESCENCE-ANALYZER": SATISFACTORY
HYDROSTATIC PRESSURE TESTED AT 523 bar, 7600 PSI DURING 10 SEC ON EACH TUBE/PIPE: SATISFACTORY

Penetrant testing on pipe body for MPQT pipes acc. to ISO 10893-4 Level P2: SATISFACTORY

VISUAL INSPECTION ON EACH TUBE: SATISFACTORY

AENOR ER Empresa Registrada UNE-EN ISO 9001

AENOR Gestión Ambiental UNE-EN ISO 14001

Luis A. San Emeterio
FTR Inspector obo Subsea7
27 April 202
REVIEWED

TUBACEX TUBOS INOXIDABLES S.A.U.
INGENIERIA DE CALIDAD

Iñigo Arriola Alcibar

8.1.3 Filler Material Certificate

voestalpine Böhler Welding Germany GmbH

voestalpine Böhler Welding Germany GmbH
Hafenstr. 21 | D-59067 Hamm
Postfach 2551 | D-59015 Hamm
www.voestalpine.com/welding

ROSENBERG WORLEY AS
Att.: Fakturamottak
PO. BOX 54
4086 HUNDVÅG
Norway

Inspection certificate 3.1

as per : EN 10204
No. : 2022-2084305795-10-106387-014
Rev. 0 Page 1 of 1

PO no.	5634-9288	of	16.06.2022
Order no.	1084003529		
Delivery note/pos./split	2084305795/000000/000010	of	11.08.2022
Product	GTAW rod/wire		
Trade name	**UTP A 6808 MO**		
Standard designation	EN ISO 14343-A: W 22 9 3 N L AWS A5.9: ER2209		
Dimension	2,4 x 500 mm		264483
Heat no.	106387		80462
Quantity	200,0 KG		1SC1A10W 0015

Chemical composition in % of the product

C	Si	Mn	P	S	Cr	Mo	Ni	Cu	N					
0,02	0,4	1,4	0,020	0,002	23,2	3,2	8,6	< 0,1	0,15					

Mechanical properties

Tensile test

T	ReL / Rp 0,2 MPa	Rp 1,0 MPa	Rm MPa	A (Lo = 5d) %	Z %	WBH PWHT	Remarks
20°C	≥ 600	≥ 650	≥ 720	≥ 25			

Impact test

T	Impact energy KV / J	Average KV / J	Lateral expansion mm	Shear fracture %	WBH PWHT	Remarks
20°C	≥ 100					

Town: Avesta
Date: 11.08.2022
This certificate was issued by DP-equipment and does not require signature.
Authorized representative: Lars-Åke Bylund

voestalpine
ONE STEP AHEAD.

8.2 Optical Microscope Images

8.2.1 Side-View Sample

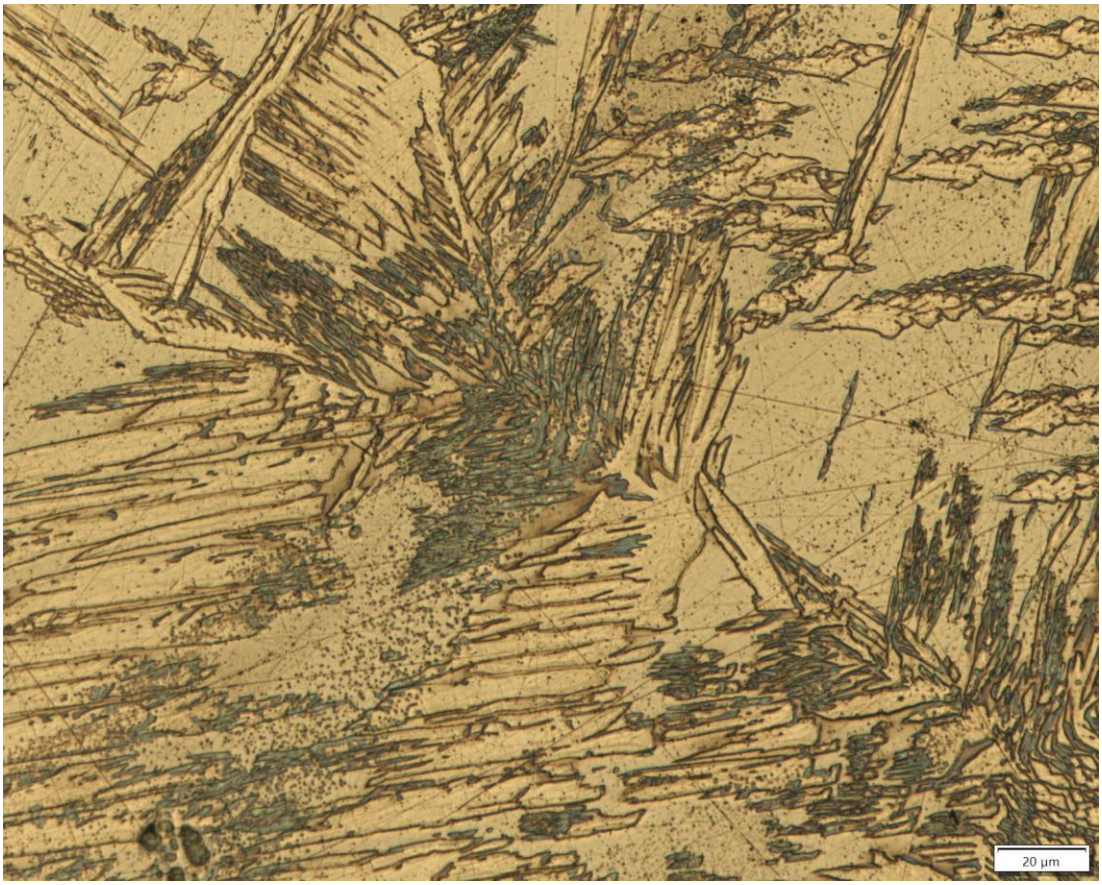

Figure 43 Image of some structure inside the weld in Side-view sample.

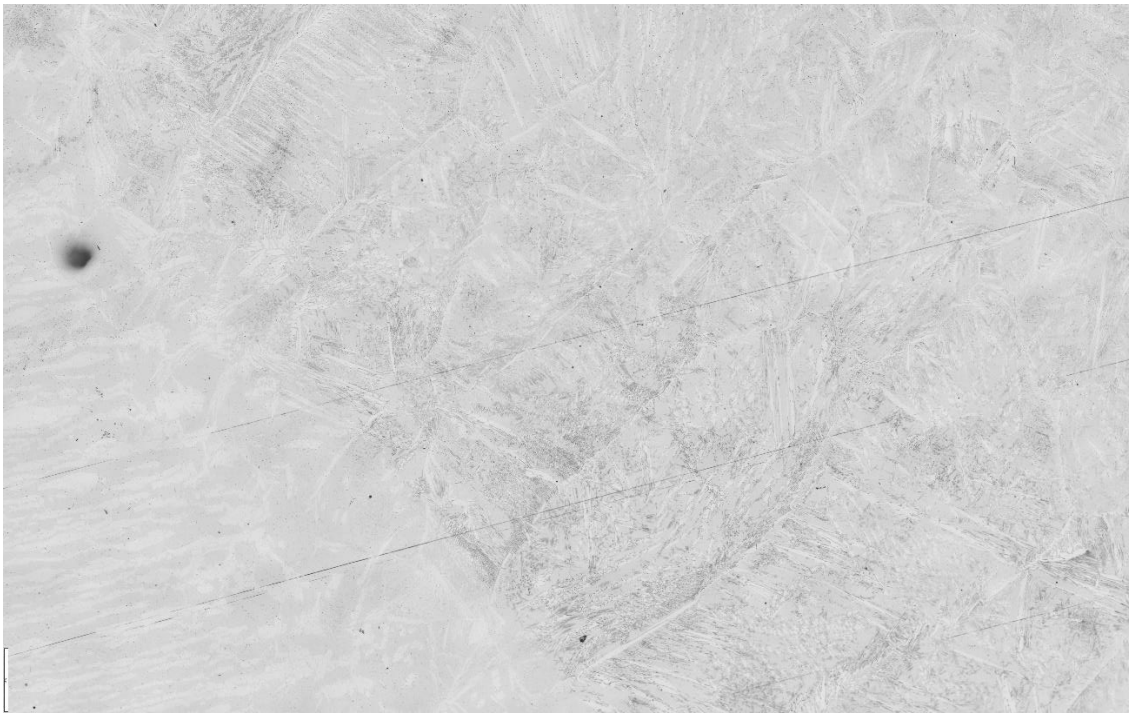

Figure 44 Overview of Side-view sample showing transition from weld to base material.

8.2.2 Bottom-View Sample

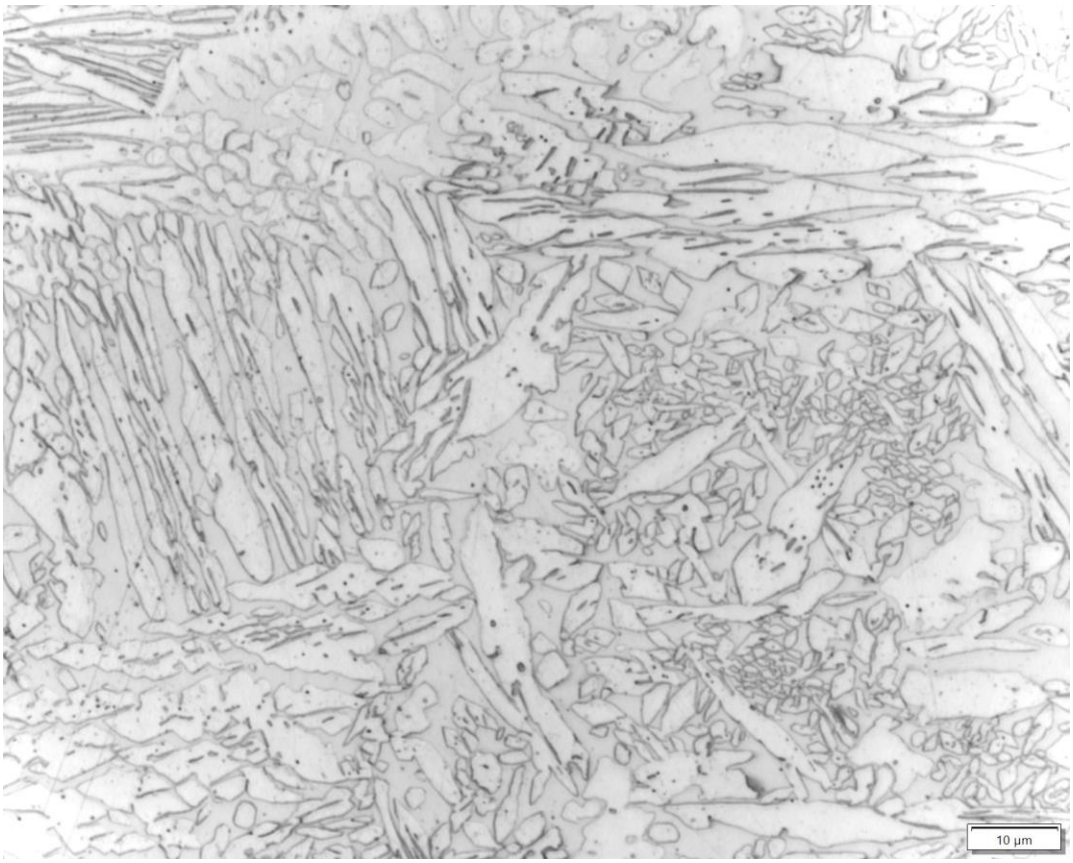

Figure 45 Different austenitic structures inside the weld.

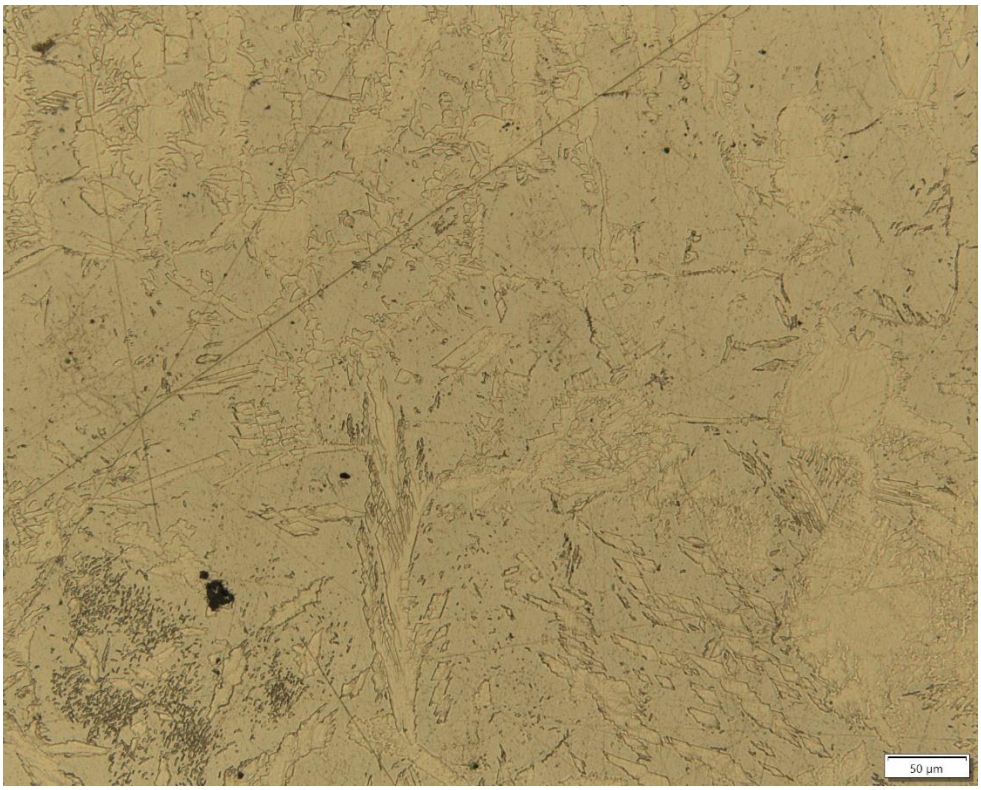

Figure 46 Image from inside the weld of Bottom-view sample.

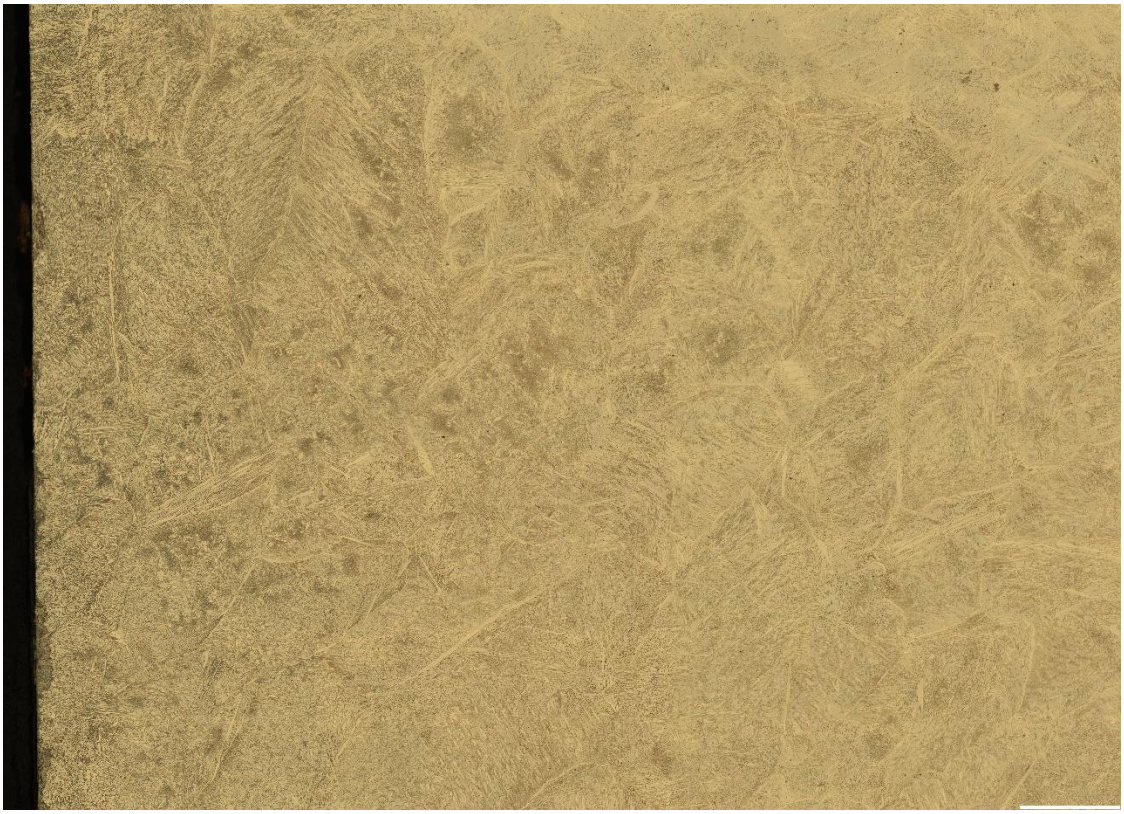

Figure 47 Overview image of the end of weld. Shows allotriomorphic and Widmanstätten austenite. The darker areas are filled with clusters of intragranular austenite.

8.3 Tensile Test Graphs

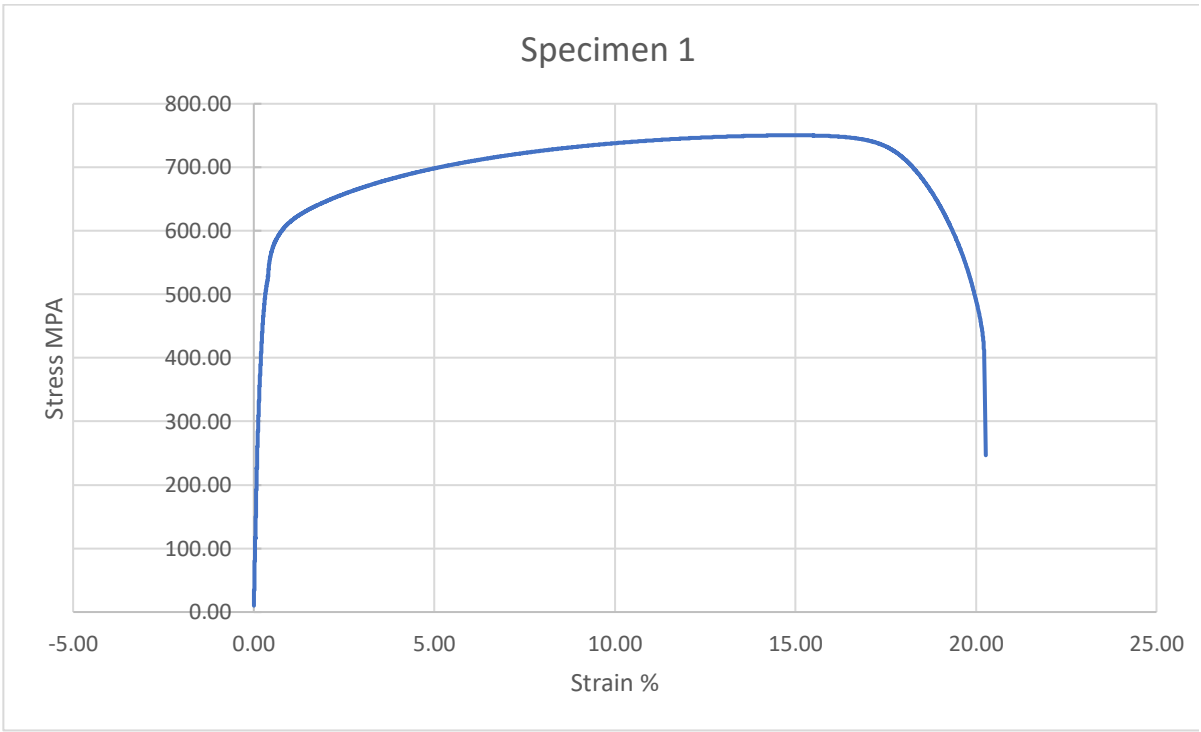

Figure 48 Graph of the results for the tension test for specimen 1.

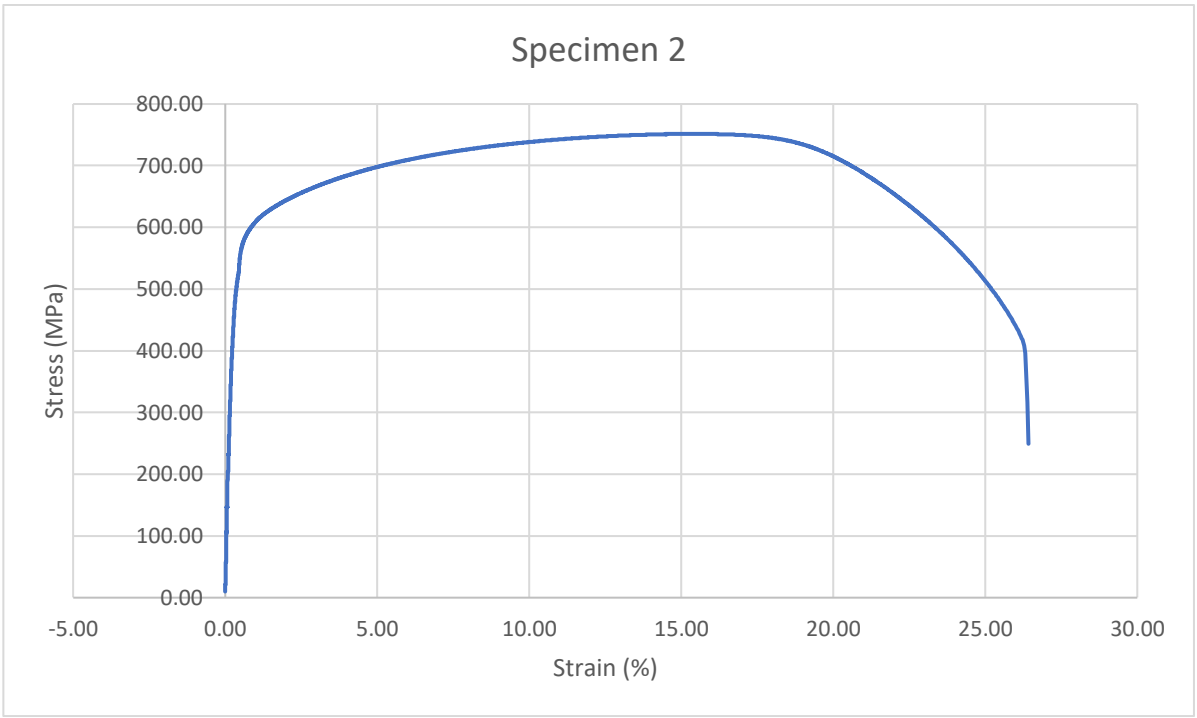

Figure 49 Graph of the results for the tension test for specimen 2.

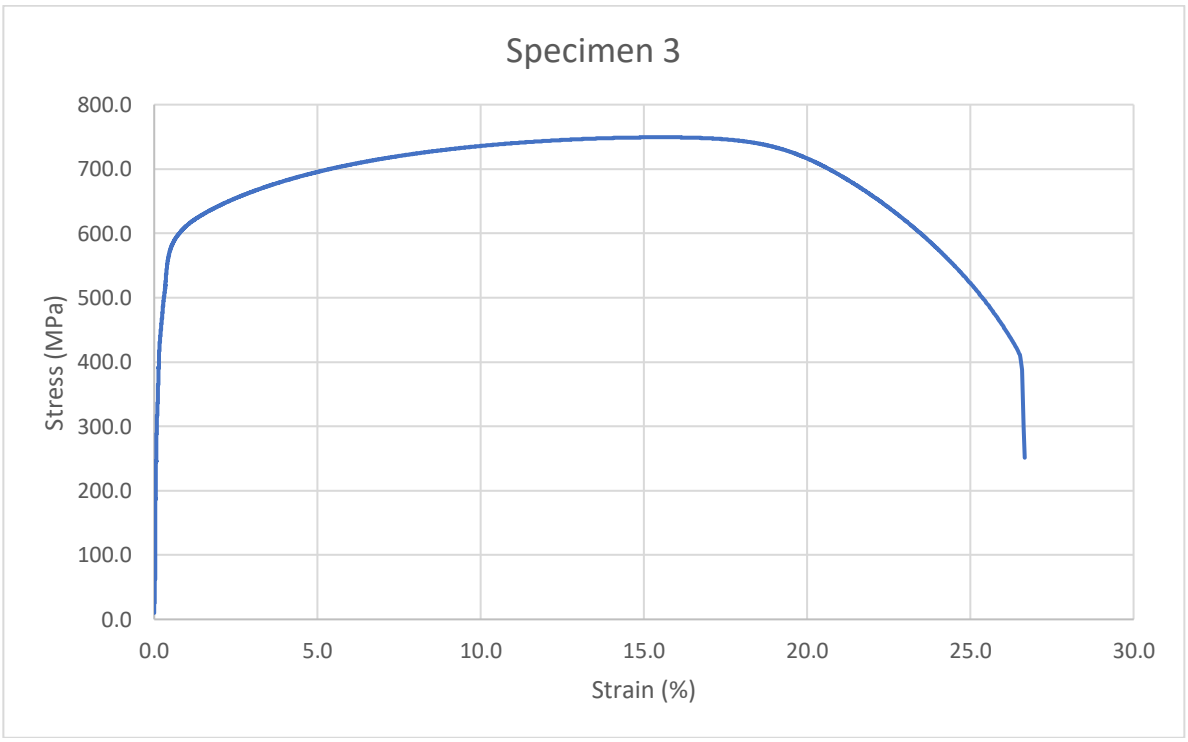

Figure 50 Graph of the results for the tension test for specimen 3.

8.4 IPF Results

8.4.1 Weld Cap – Higher

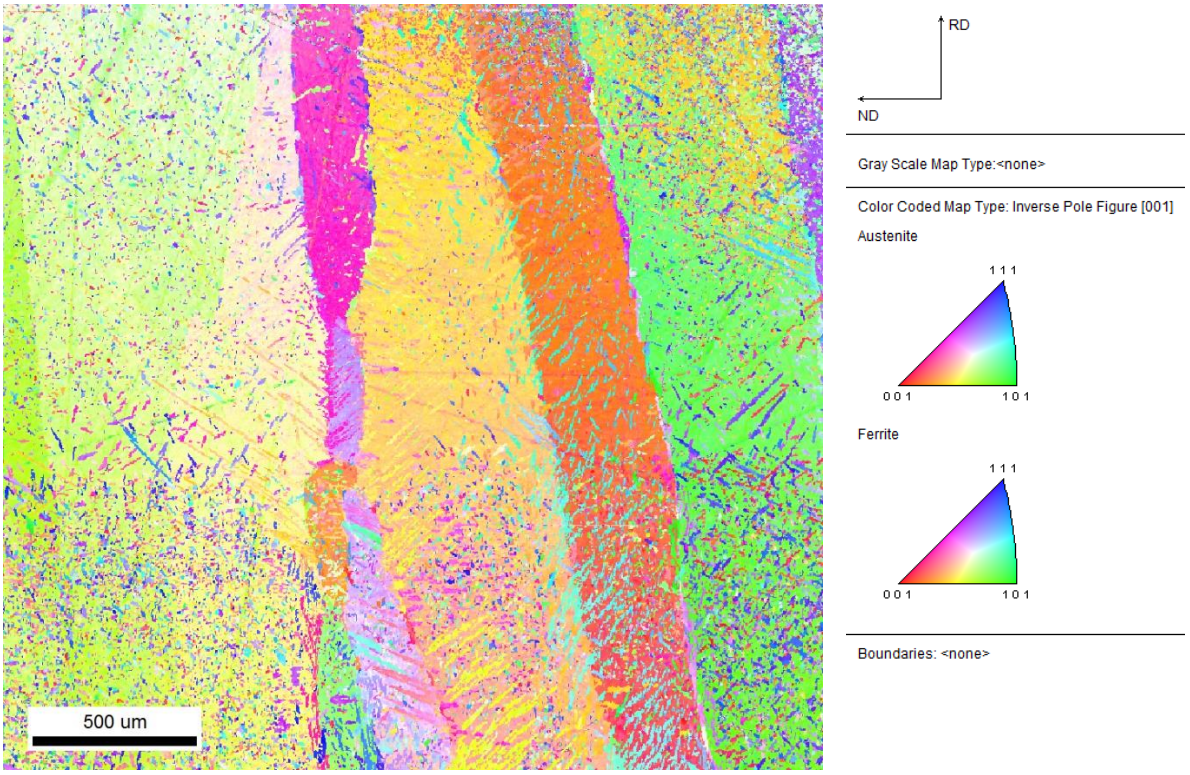

Figure 51 IPF for upper part of weld cap.

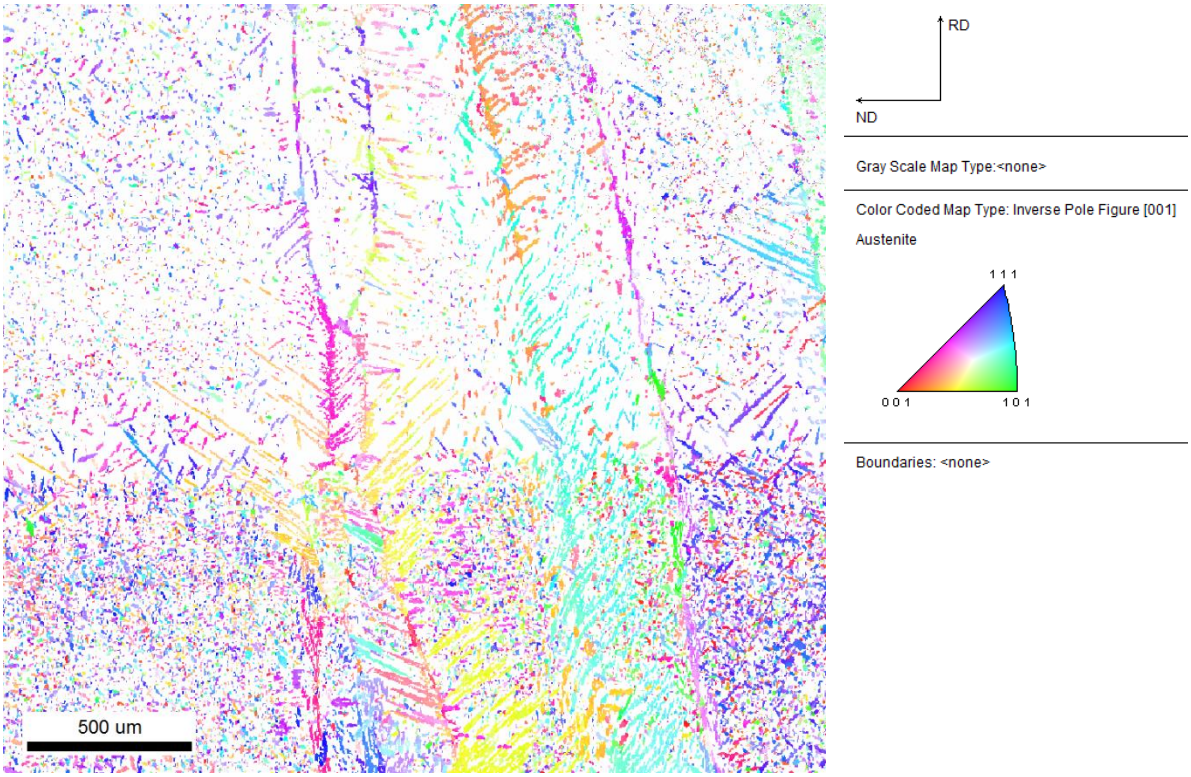

Figure 52 IPF showing austenitic structures in upper weld cap.

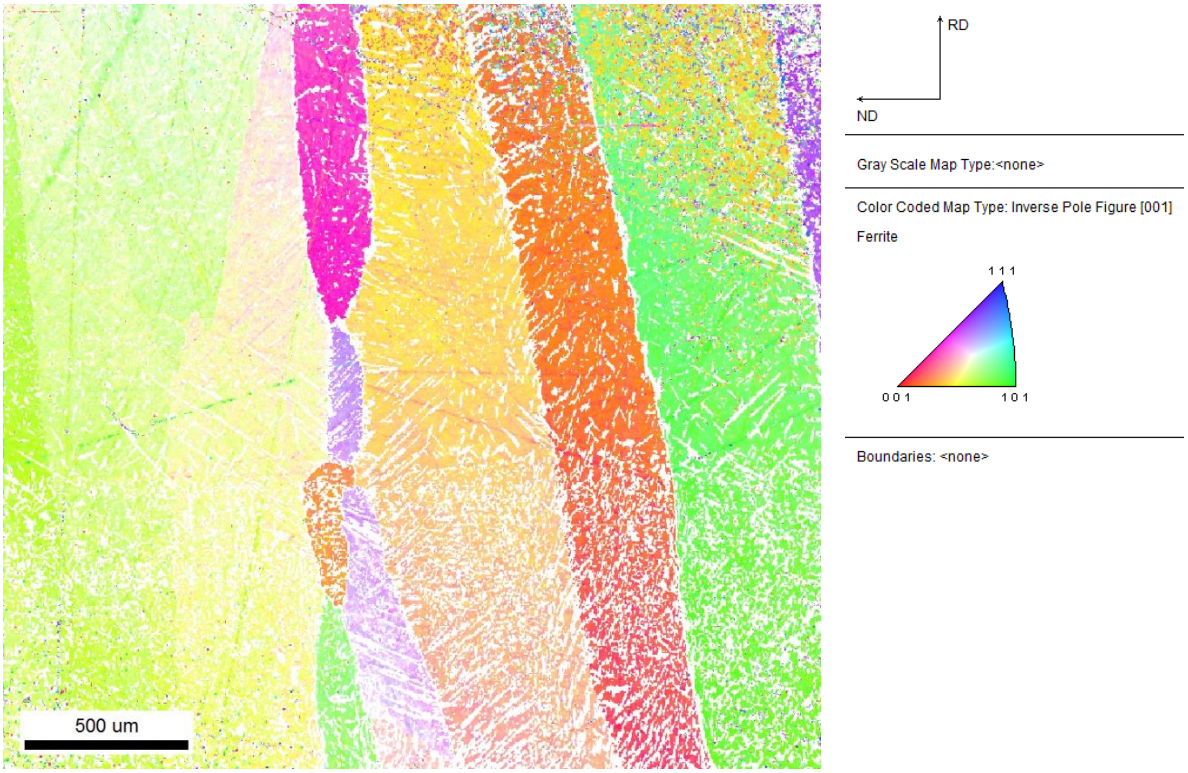

Figure 53 IPF showing ferritic structures in the upper weld cap.

8.4.2 Weld Cap – Lower

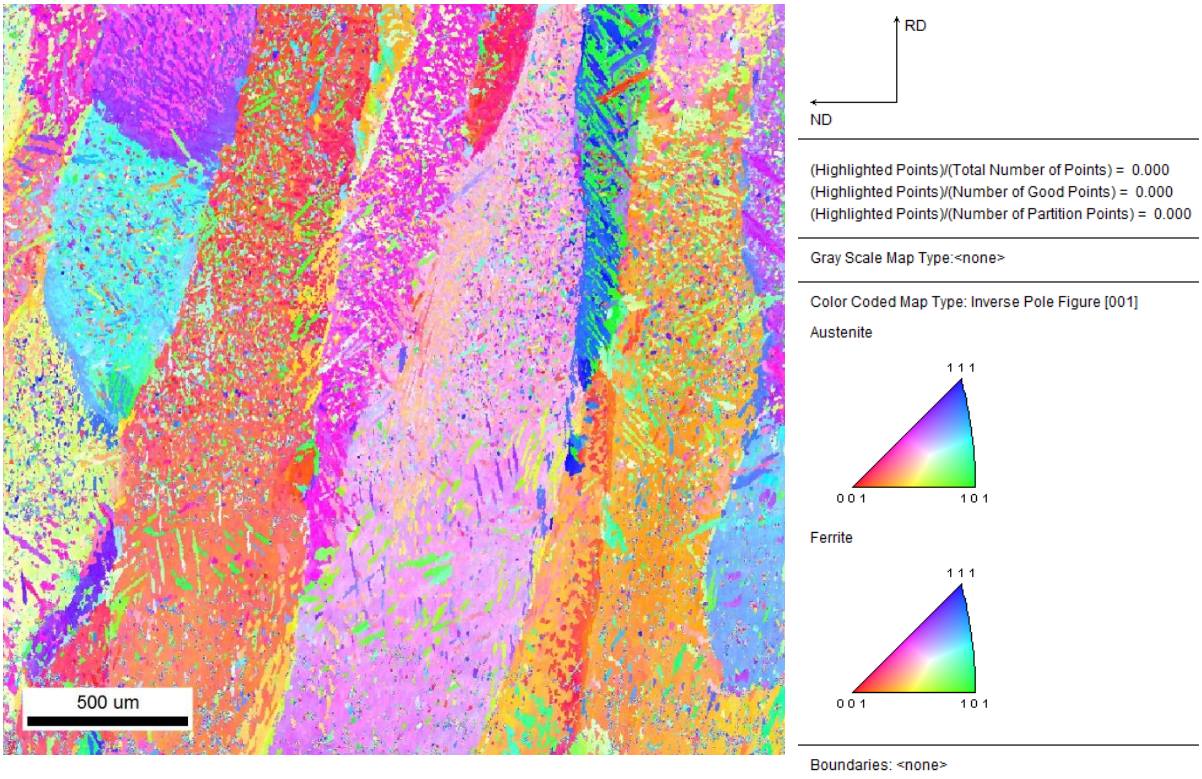

Figure 54 IPF for weld cap.

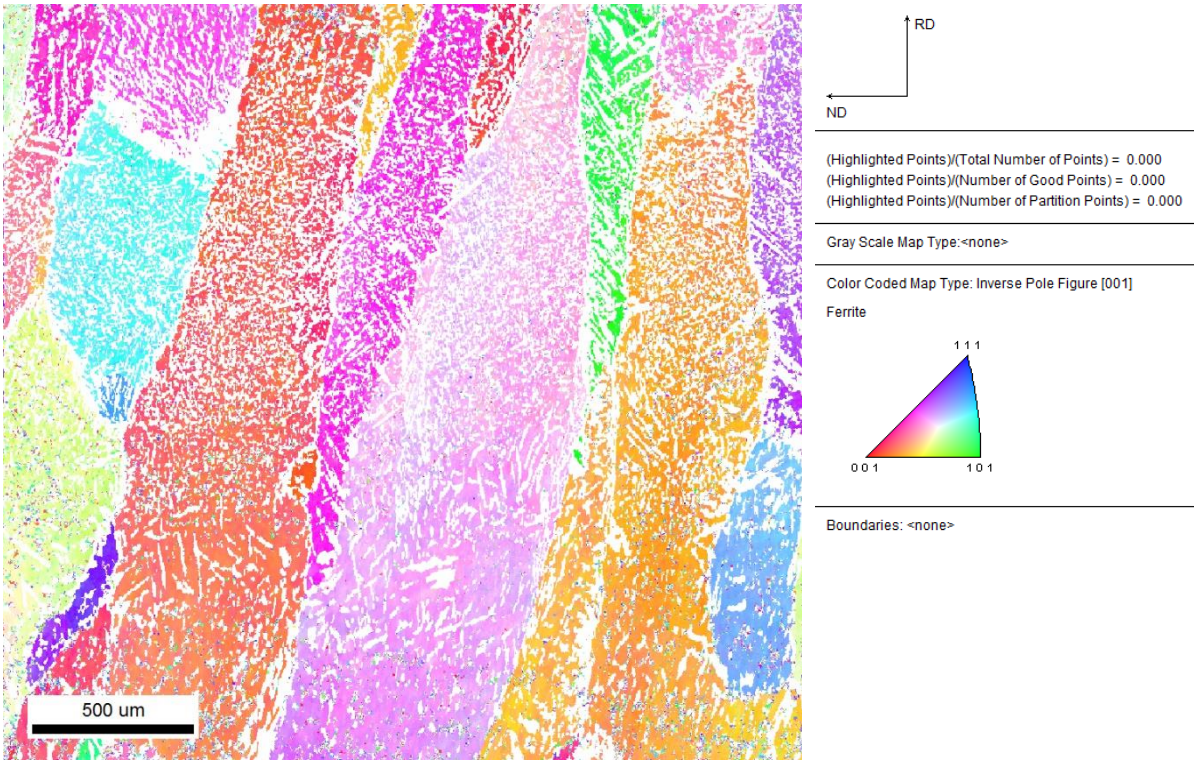

Figure 55 Ferrite IPF for weld cap.

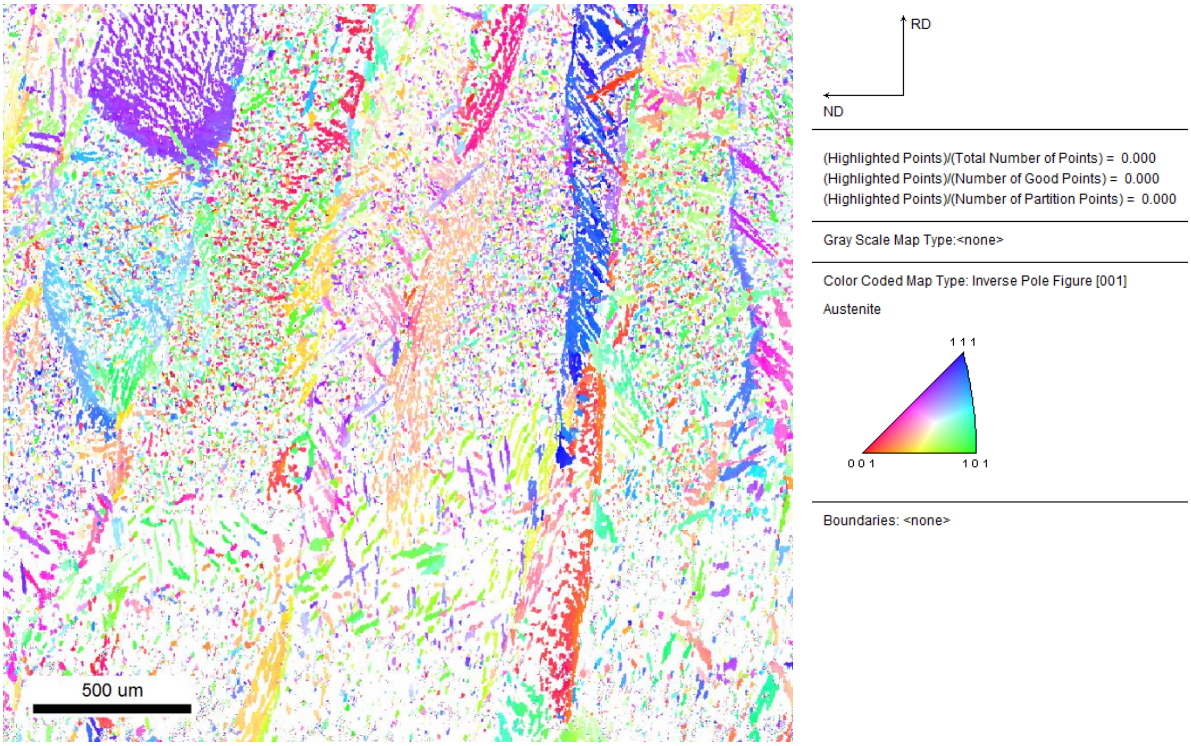

Figure 56 Austenite IPF for weld cap.

8.4.3 Center of Weld

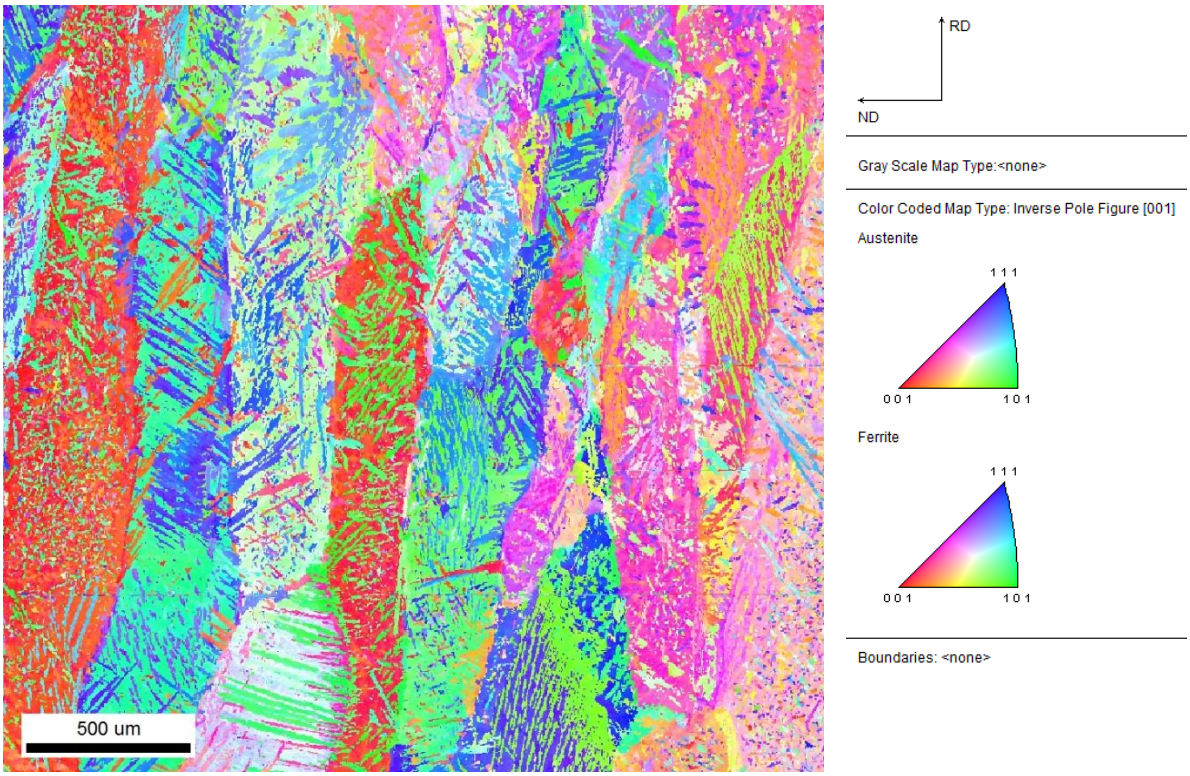

Figure 57 IPF for the center of the weld.

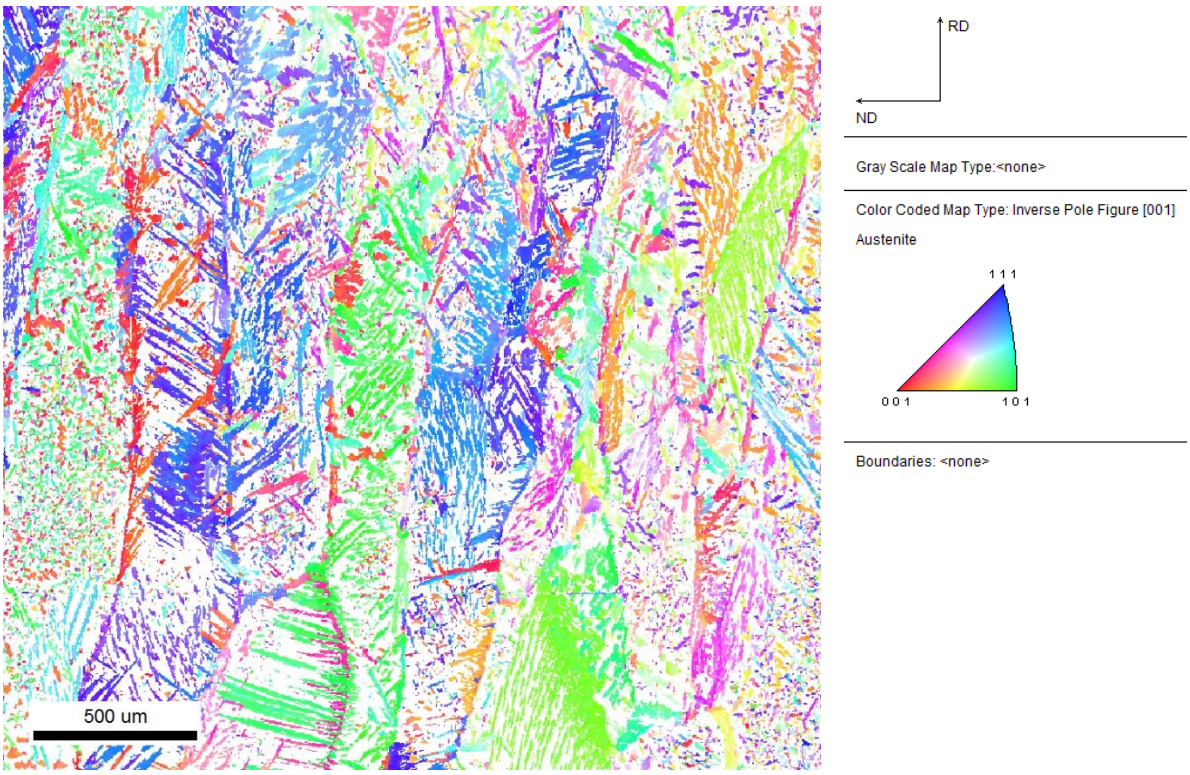

Figure 58 IPF showing austenitic structures in the center of the weld.

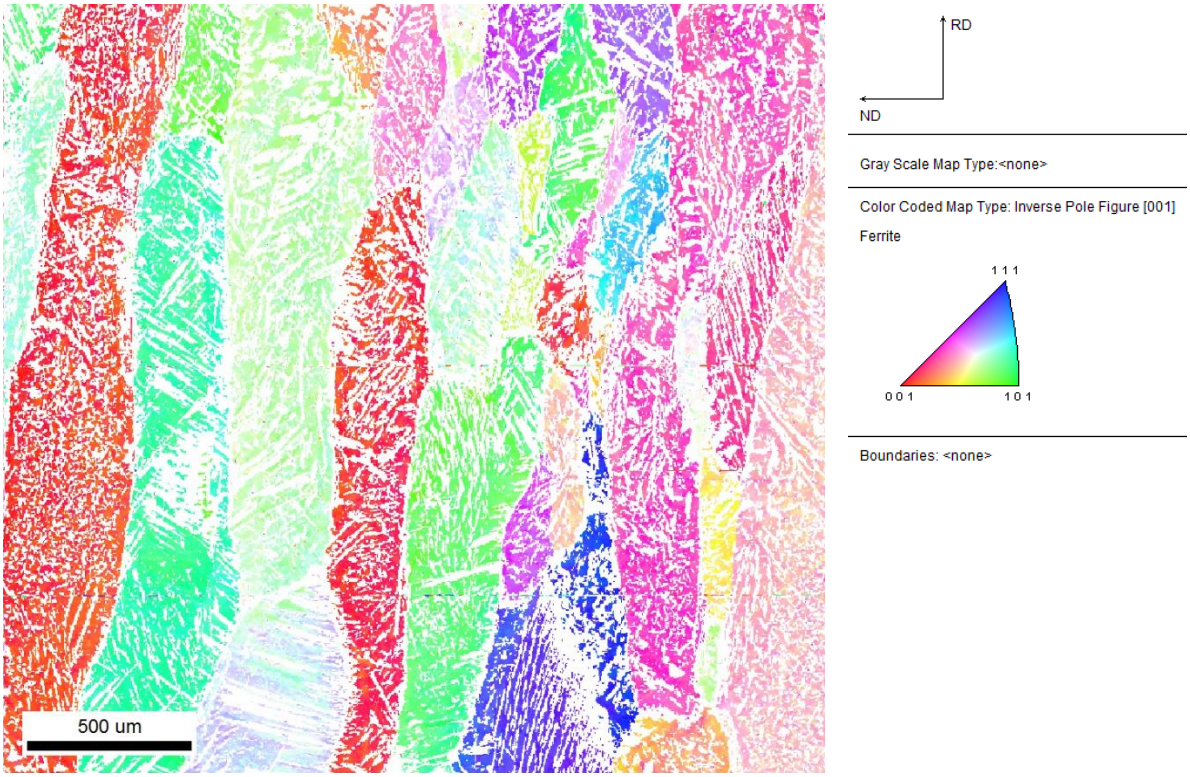

Figure 59 IPF for ferrite in the center of the weld.

8.4.4 HAZ and Surrounding Areas

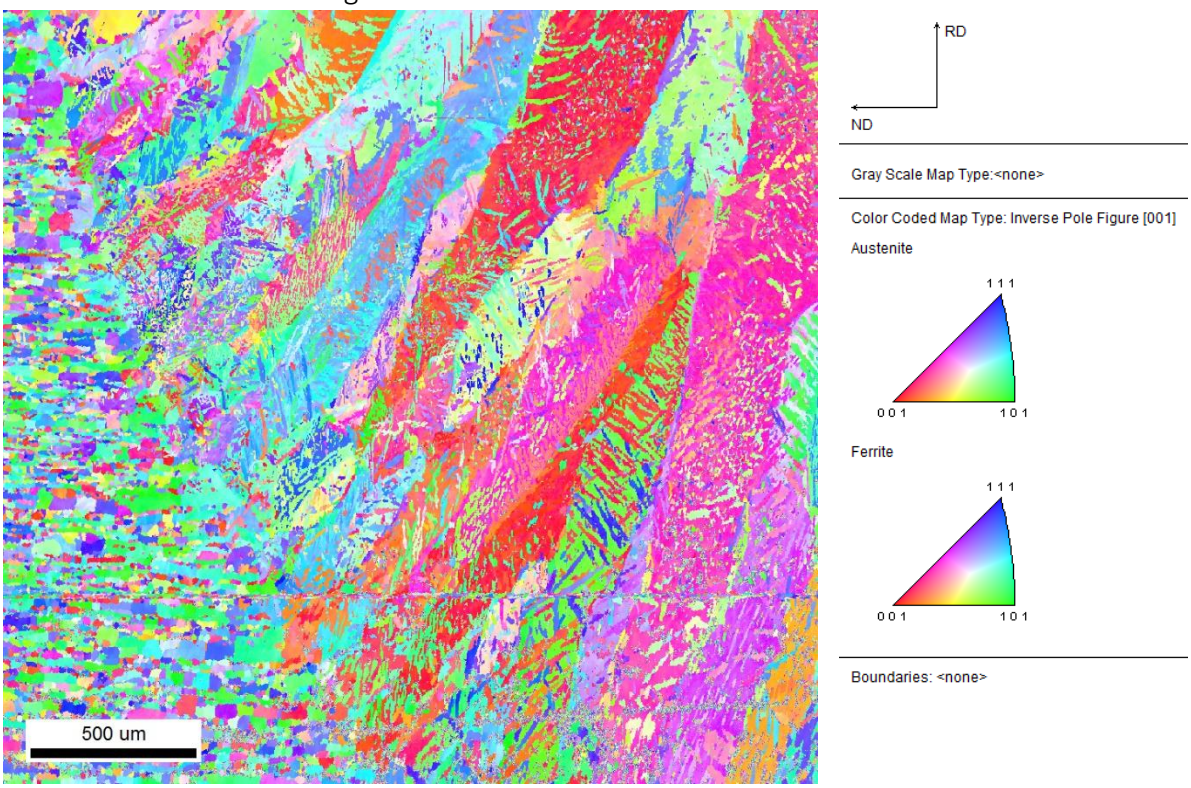

Figure 60 IPF for the left HAZ.

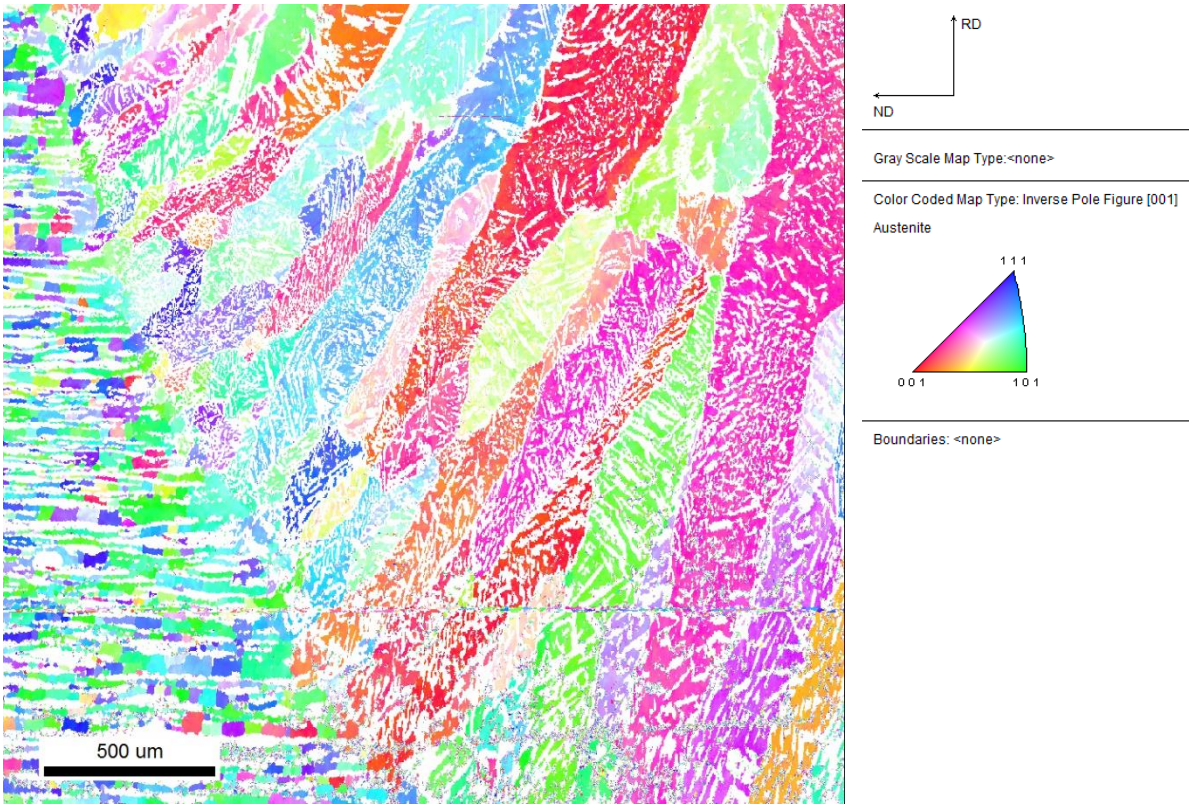

Figure 61 Ferrite IPF for the left HAZ.

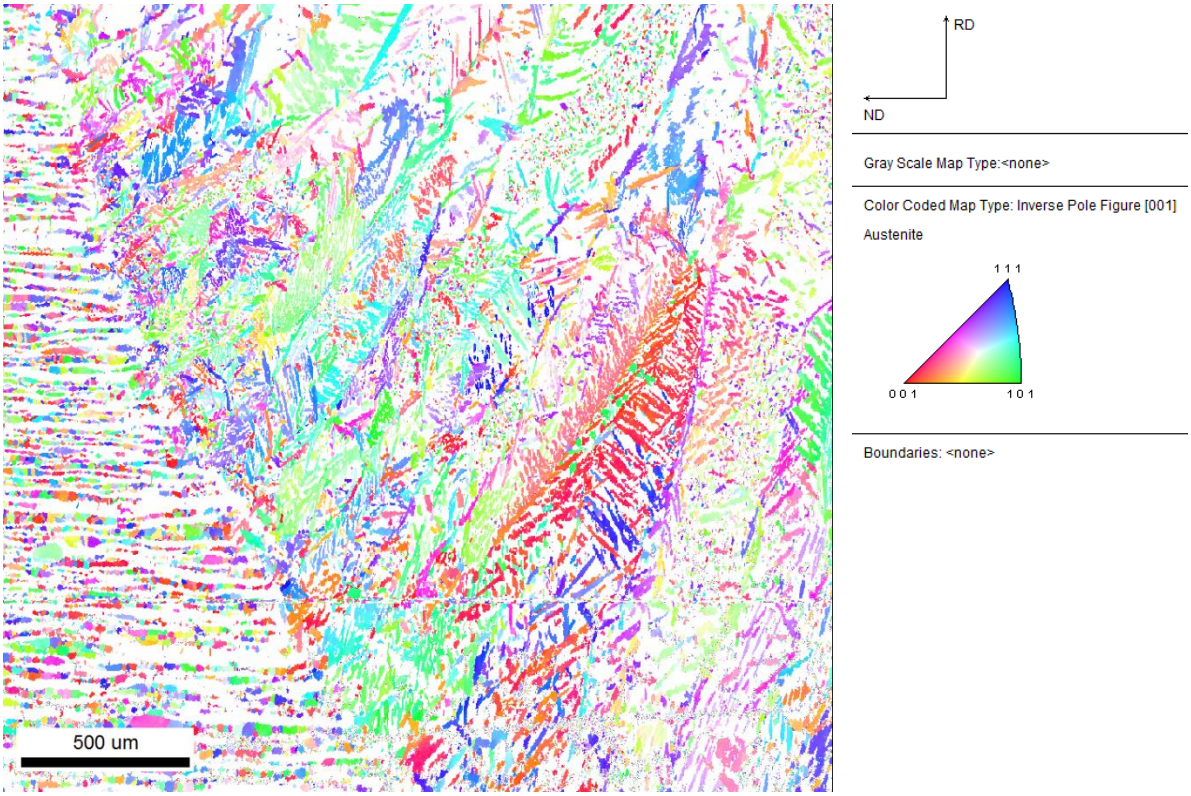

Figure 62 Austenite IPF for the left HAZ.

8.4.5 Root Bead

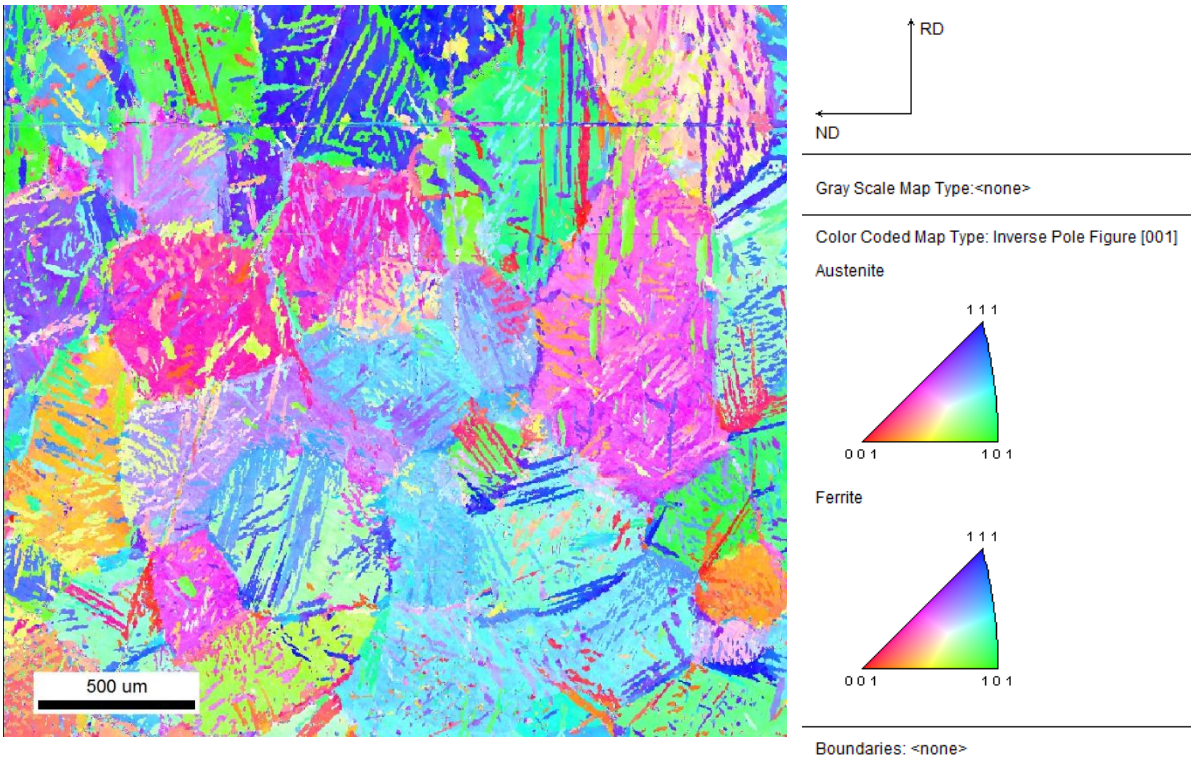

Figure 63 IPF for Root Weld.

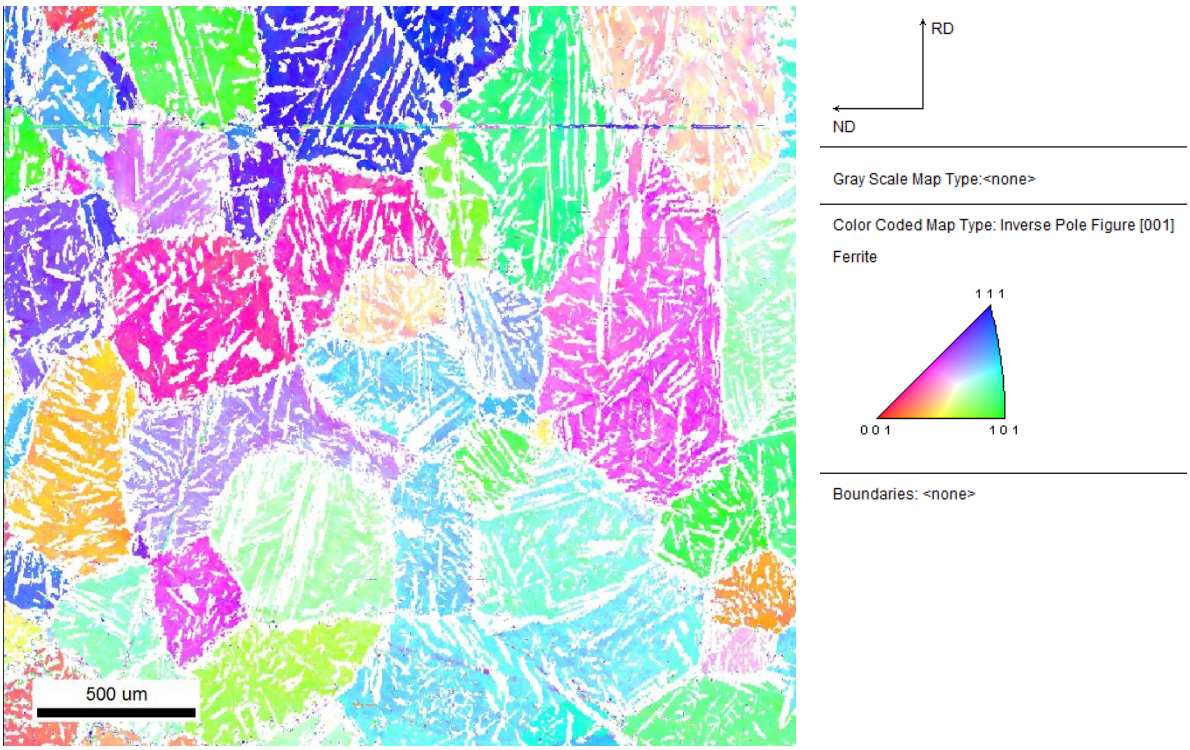

Figure 64 IPF for root weld, coloring only the ferrite.

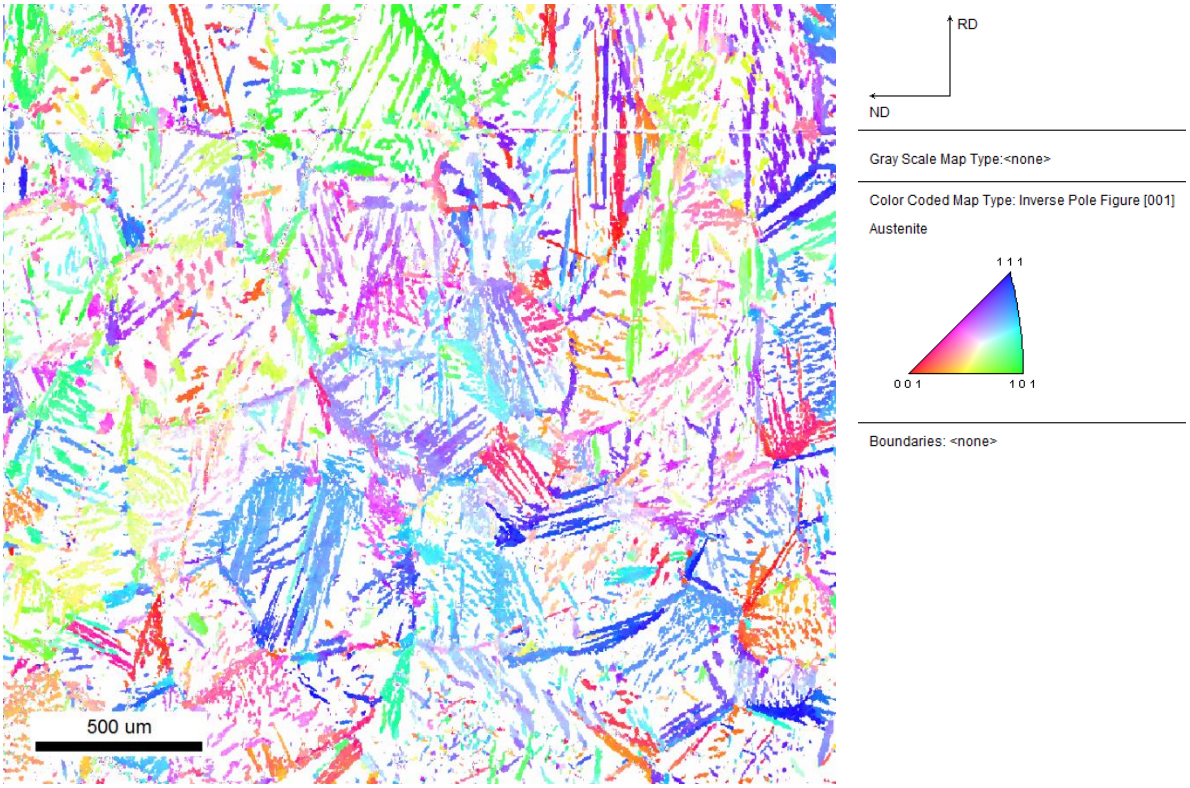

Figure 65 IPF for root weld, coloring only austenite.

8.5 EDS Graph Data

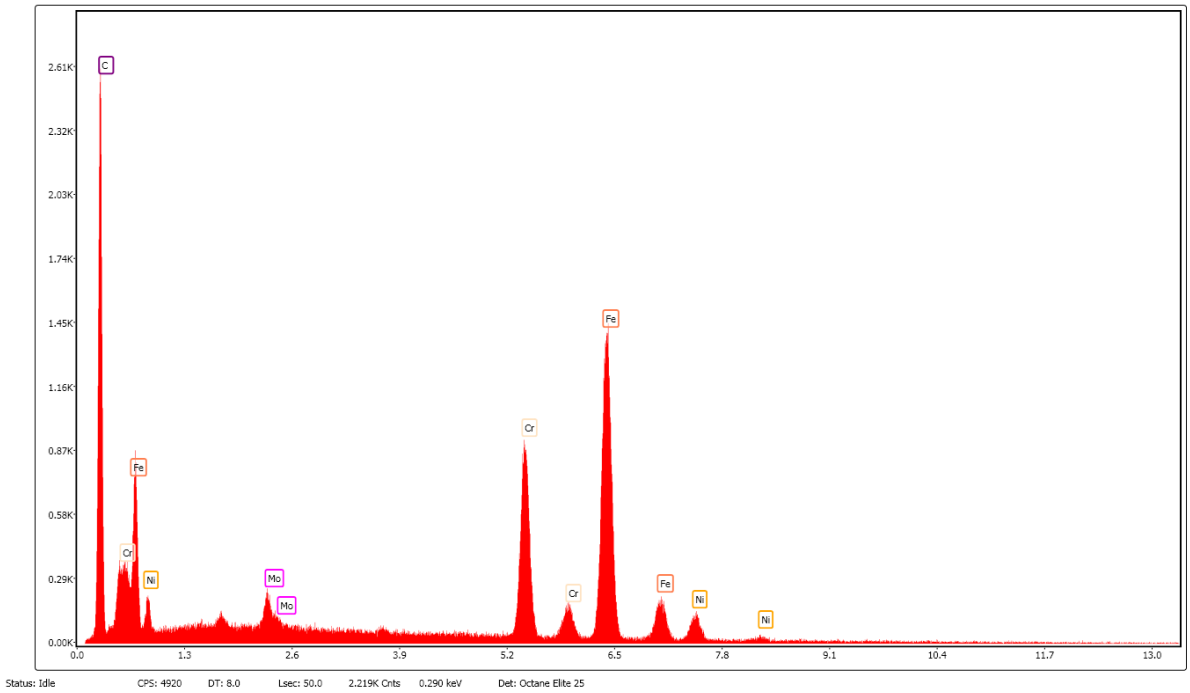

Figure 66 EDS results for spot 1, area 1.

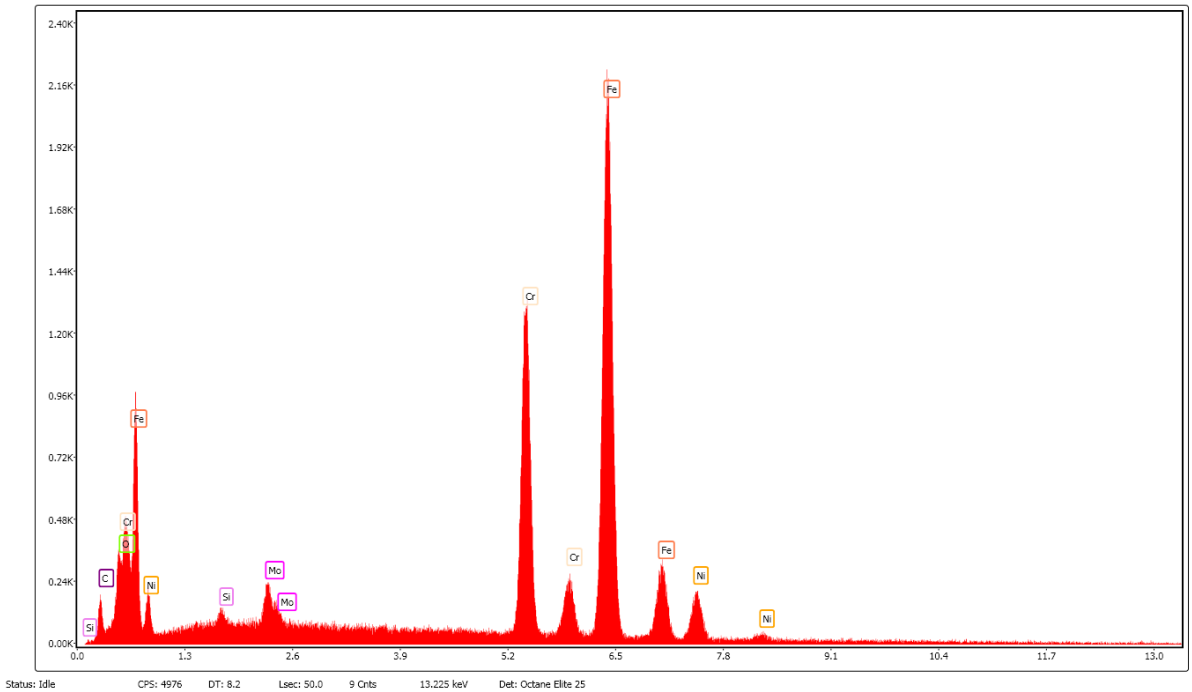

Figure 67 Results for EDS for spot 2, area 1.

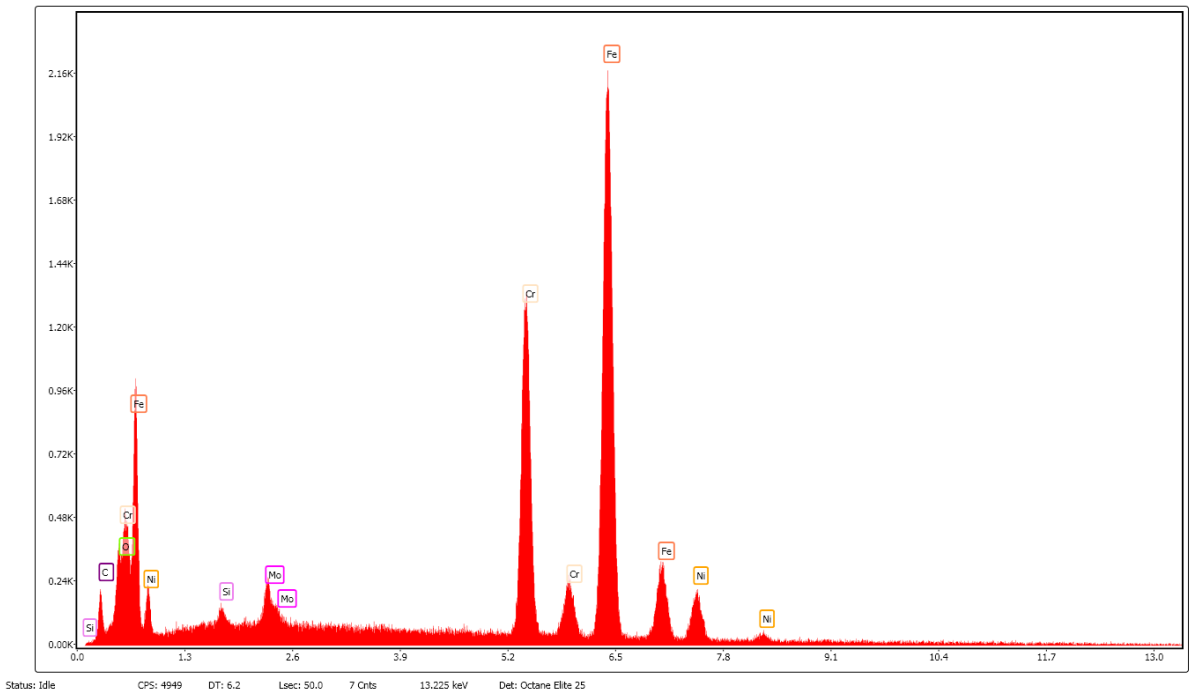

Figure 68 EDS for spot 3, area 1.

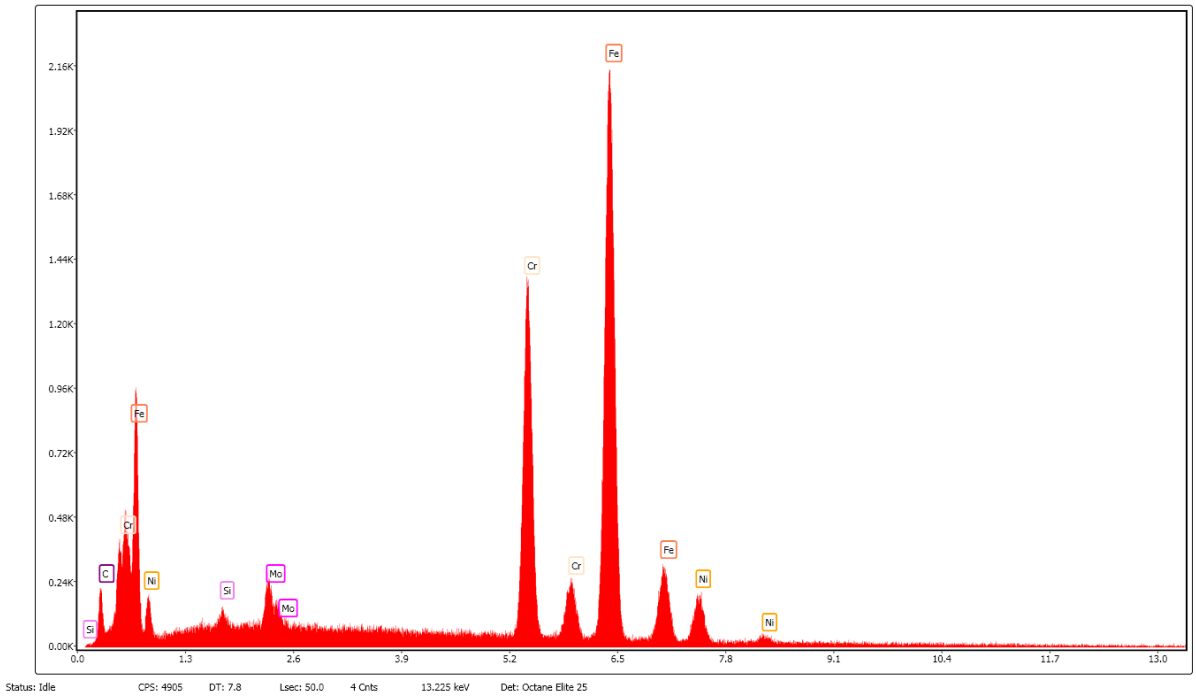

Figure 69 EDS for spot 4, area 1.

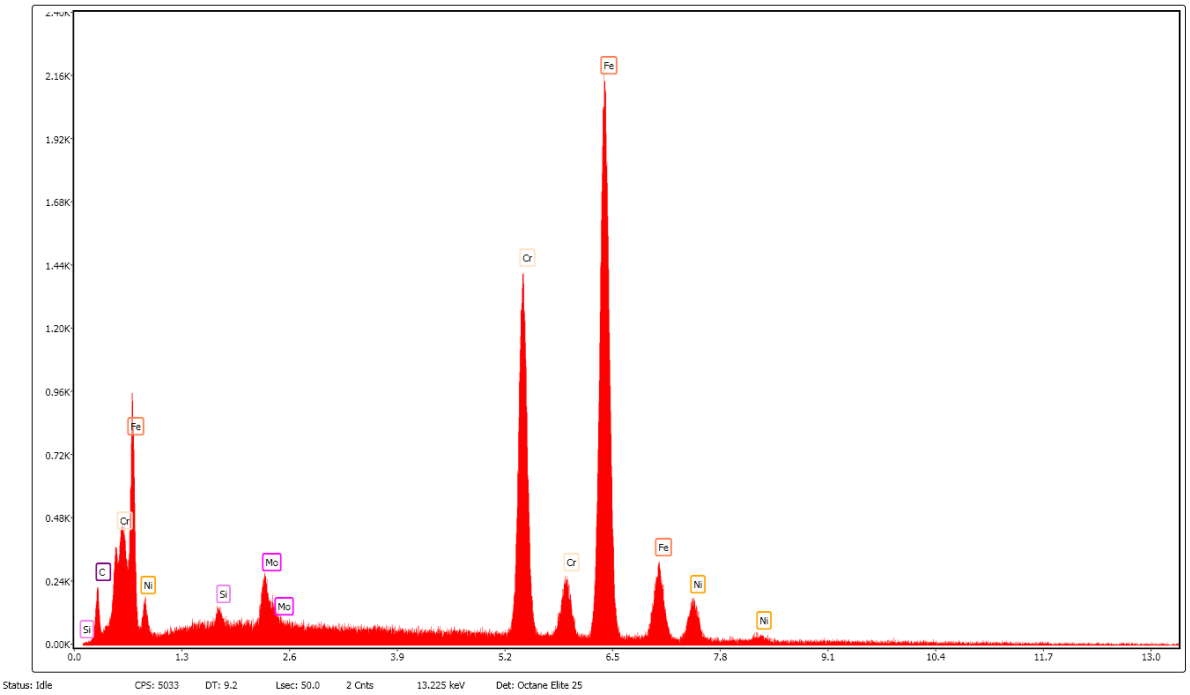

Figure 70 EDS for spot 5, area 1.